Metallurgy and Mechanics of Low-Enriched Uranium (LEU) and its Alloys for Isotope and Energy Production

A Thesis

Presented to

the faculty of the School of Engineering and Applied Science

University of Virginia

in partial fulfillment

of the requirements for the degree

Master of Science

by

Daniel Malta

August

2018

APPROVAL SHEET

The thesis
is submitted in partial fulfillment of the requirements
for the degree of
Master of Science

AUTHOR

The thesis has been read and approved by the examining committee:

Sean Agnew
Advisor

James Howe

Matthew Panzer

Saumyadeep Jana

Accepted for the School of Engineering and Applied Science:

Craig H. Benson, Dean, School of Engineering and Applied Science

August
2018

Abstract

Use of highly-enriched uranium (HEU) at research reactors or the exporting of HEU for humanitarian purposes, such as for the production of medical isotopes, leads to a risk of nuclear proliferation. This thesis will discuss efforts to improve the understanding of low-enriched uranium (LEU) to enable more accurate predictions of the material behavior during manufacturing and use as an irradiation target for the production of medical isotope Tc-99m and as a reactor fuel.

The α-phase (orthorhombic crystal structure) LEU foils proposed for use in the production of medical isotope Tc-99m have anisotropic properties due to the crystallographic texture which is introduced during the foil rolling process. This was previously demonstrated using physics-based viscoplastic self-consistent (VPSC) modeling, which used the deformation-induced texture as an input [1]. A phenomenological, analytical model for the anisotropic yield stress behavior of orthotropic, hexagonal metals was developed by Cazacu, Plunkett, and Barlat [2], denoted CPB06. A MATLAB optimization routine was used to determine values for the anisotropy coefficients used in the model, by fitting to the VPSC predictions. CPB06 was implemented as a user-subroutine (VUMAT) in ABAQUS/Explicit, a commercial finite element analysis (FEA) software, which allowed for finite element simulation of the irradiation target manufacturing process. FEA simulations ultimately revealed that while the plastic anisotropy of the foil could potentially change the strength of the material relative to the isotropic case under certain loading conditions, anisotropy did not noticeably affect the foil strength when under internal pressure, and the performance of the Tc-99m target was not affected.

The γ-phase stabilized LEU-10Mo (wt%) alloy has been identified as a candidate fuel for high performance research reactors, though there are concerns regarding phase and mechanical

stability under reactor conditions, especially during transient conditions. *In-situ* neutron diffraction performed at the Los Alamos Neutron Science Center (LANSCE) was used to investigate phase decomposition behavior in U-10Mo and U-9.8Mo with 0.2 wt% ternary additions of Cr, Ni, or Co, thus maintaining the total alloy content in all four alloys at 10 wt%. Since the metastable BCC phase γ-U is optimal, it is critical to understand whether or not such alloying additions delay or promote phase decomposition. These alloying additions were chosen for research since they are readily available, and come in different unit-cell structures (BCC, FCC, and HCP).

During the *in-situ* experiments performed on the Spectrometer for Materials Research at Temperature and Stress (SMARTS), the samples were first heated at a rate of 50 ºC/min to ~650 ºC, which is above the γ-phase solvus line, and held for 1 hour to dissolve any fine, second phase particles which may have precipitated during prior heating and homogenization steps. Then, the samples were cooled at a rate of 50 ºC/min to the isothermal hold temperatures of interest, 490 or 500 ºC, and held for 20 hours to observe the kinetics of decomposition of the metastable γ-U-Mo phase toward the equilibrium α-U and γ’ (U_2Mo) phases. Finally, the samples were cooled to room temperature at a rate of 50 ºC and remeasured *ex-situ*, both in SMARTS and in the High Intensity Pressure and Preferred Orientation (HIPPO) instrument. Rietveld analysis using the GSAS-II and MAUD software packages was employed to determine the phase fractions, lattice parameters, and crystallographic texture of all the observed phases.

Experiments conducted on U-10Mo and U-9.8Mo-0.2Cr did not exhibit measurable phase decomposition. However, some phase evolution was observed in the U-9.8Mo-0.2Ni and U-9.8Mo-0.2Co alloys, which included development of the orthorhombic α-U phase along with a corresponding molybdenum-rich, and perhaps ordered, version of the BCC γ-phase, here denoted

γ_b. Hence, it is concluded that Ni and Co ternary additions degrade the thermal stability of U-10Mo, while Cr additions do not have an observable effect. It is hypothesized that the more rapid phase evolution in the Ni and Co containing alloys is due to heterogeneous nucleation associated with the presence of small grain boundary precipitate phases, including U_6Co and U_6Ni, which were previously observed by SEM [3], and whose presence is corroborated by the presence of a small, solitary neutron diffraction peak in the experiments performed on U-9.8Mo-0.2Co.

Table of Contents

List of Figures

List of Tables

1. Introduction

1.1 Motivation

The National Nuclear Security Administration's Material Minimization and Management (M3) Program is currently researching LEU as an alternative to HEU for applications such as the operation of research reactors and production of diagnostic medical radioisotopes. Reducing the need for HEU fuels by developing reliable LEU fuels which maintain performance will decrease the chance of nuclear proliferation. HEU is defined as uranium which contains greater than 20 wt% of ^{235}U, the isotope of uranium which can sustain fission reactions. Many HEU fuels are greater than 90 wt% ^{235}U, posing serious proliferation risks [4]. Nuclear fuel above an enrichment level of 20% poses a national security risk since it can be used to make simple improvised nuclear weapons by terrorists [5]. Many civilian facilities which use and store HEU lack adequate security to prevent criminals and terrorists from taking fresh or spent fuel, and the United States has only sufficiently accounted for 10% of the HEU material exported [6]. While many research reactors initially used LEU fuels, the LEU fuels in the 1950's simply were not as powerful as HEU fuels, and the pursuit of higher performance drove the switch to HEU fuel sources [7]. However, with increasing global awareness of international security, it is now imperative to develop LEU fuel sources that are capable of powering our research reactors and meeting production demands for medical diagnostic imaging.

Tc-99m is a metastable nuclear isomer used in about 85% of nuclear medical diagnostic imaging procedures worldwide, making it the most commonly used medical radioisotope [8]. Tc-99m is a decay product of Mo-99, which is produced commercially by the fission of HEU in research and material testing reactors around the world. Mo-99 can be also be produced by the irradiation of LEU, although with lower production efficiency due to the lower fission yield. The primary benefit to using LEU, in addition to international security, is that export controls of LEU are less stringent than for HEU, so it can be used in a larger portion of nuclear reactors worldwide [9]. Mo-99 has a short half-life of 2.75 days, and Tc-99m has a half-life of a mere 6 hours, so production of the radioisotope on a global scale is preferred so that it can be transported to where it is needed quickly.

Figure 1. HEU and LEU reactors used worldwide for Mo-99 Production [10]

One proposed method of generating Mo-99 and thus Tc-99m from LEU involves the manufacture and subsequent irradiation of an annular target. This target is comprised of a thin LEU foil pressed between aluminum tubes by a method known as hydroforming, where hydraulic pressure is applied to deform the tubes to hold the foil tightly in place [11]. This process creates a target for irradiation which will contain the uranium during fission and also conduct heat from the irradiated material to surrounding coolant. A thin layer of electro-deposited nickel (~15-25 microns), is used to prevent bonding between the uranium and aluminum [12]. The annular target is bombarded with neutrons to initiate fission reactions which result in the formation of Mo-99. Finally, the assembly is cut open and the fission products are retrieved for post-processing so that the Mo-99 product can be isolated and transformed to Tc-99m with the appropriate timing for a medical imaging procedure.

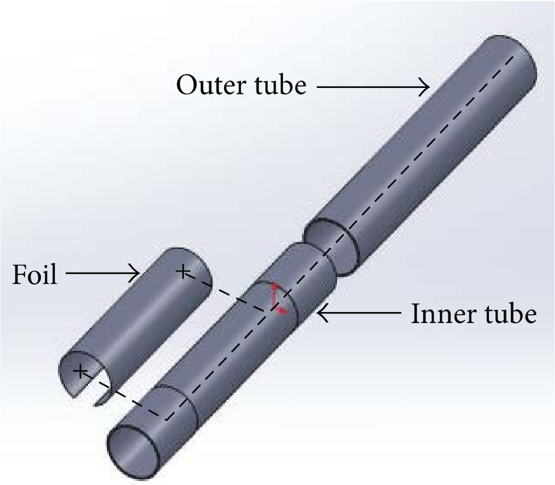

Figure 2. Diagram of LEU irradiation target components [13]

During manufacturing and use of the LEU irradiation target, the assembly undergoes processes such as internal pressurization, pressure relaxation, and then irradiation, which generate residual stresses in the foil and aluminum tubes. The post-irradiation residual stress-state of the LEU target foil and surrounding assembly is critical to the proper retrieval of the fission products. If the residual hoop stress is tensile in nature, the outer tube will spring open once cut, allowing for easy retrieval of the fission products. However, if the outer tube is in a compressive state, it will collapse when cut, making retrieval of the fission products more difficult.

Finite element analysis allows for the physical response to be modeled at each location in a simulation assembly and readily visualized, even with complex shapes. As a result, it can be used to perform parametric studies examining a variety of loading conditions and material parameters without the need for expensive physical testing, especially in the case of radioactive materials. Previously, finite element simulations of the Tc-99m target assembly hydroforming and irradiation scenario were conducted in which the uranium foil was considered to have the properties of isotropic, bulk α-uranium [13]. However, since the foil is manufactured by cold-rolling to a large reduction in thickness, roughly 3 mm to 100-150 microns [1, 14], there is significant development of texture and therefore anisotropy in the foil. Considering how delicately the success of the target assembly depends on the residual stress-state of the target assembly, modelers ought to consider the severe anisotropy of the foil as a component of the entire system. Once the anisotropy of the foil is modeled and accounted for in the finite element simulations, if it is determined that the residual stress-state of the assembly is significantly affected, then some aspect of the assembly process for the foil and tubes may have to be adjusted so that the retrieval of fission products can take place efficiently.

In addition to medical isotope production, LEU fuels are necessary to the operation of research reactors. The conversion to LEU fuel sources in research reactors requires developing a new class of nuclear fuel which has a higher density of uranium in order to obtain higher energy output. However, using pure uranium poses problems since the highly anisotropic properties of orthorhombic α-phase of uranium will cause the nuclear fuel to swell and degrade during use. The high-temperature BCC phase of uranium, γ-U, has desirable properties for use as a nuclear fuel [15]. However, this phase is metastable at room temperature, and secondary phases, α-U and γ' (U_2Mo), will develop below the eutectic temperature which will ruin the stability and performance of the fuel during irradiation as a result of their anisotropic properties. The favorable metastable BCC γ-U phase can be preserved at temperatures below the eutectic by alloying. U-Mo alloys provide a good balance between a high density of uranium and a high level of γ-phase stability [16]. An increase in the molybdenum content of the alloy improves the fission gas behavior, particle swelling, and phase stability of the fuel [17]. In this thesis, U-10 wt% Mo will be studied since U-Mo alloys around this level of alloy content are considered to have an optimal balance of uranium density and stability during irradiation.

In particular, the effect of small additions (0.2 wt%) of ternary alloys will be studied for any effect on the phase decomposition kinetics of the U-10Mo system. Previously, it has been seen that certain transition metals can be useful for preserving the metastable γ-phase of U-Mo below the eutectoid temperature [18]. Some of the elements frequently studied for the purpose of γ-phase stability include Mo, Nb, Ru, V, and Zr. Experimentally, Mo, Nb, and Ru were found to stabilize the γ-phase, while V was seen to have little effect, and Zr was shown to decrease the stability [19]. Using a modeling approach, the effectiveness of various transition metals in stabilizing the γ-phase when they are added to U-Mo alloys has been calculated [20]. Here, addition of Zr was shown to decrease decomposition time relative to U-Mo, but Re, Ru, and Pt increase the nucleation time substantially in comparison to U-Mo. It is clear that adding these metals to the nuclear fuel often has an effect on the stability of the fuel. Some of the more common metals for impurities in nuclear fuel which have not been studied significantly include Cr (BCC), Ni (FCC), and Co (HCP). This thesis study will aim to observe the effect of the presence of these transition metals of varying crystal structures on the phase stability of the fuel.

1.2 Research Objectives

The research conducted for this thesis will help advance LEU technology so it can be used on a global scale for isotope production and powering small-scale reactors. The objectives of the FEA research for the assembly and irradiation of the LEU target are as follows:

1. Fit the CPB06 model parameters to yield surface results generated by prior VPSC modeling.
2. Conduct benchmarking with FEA which validates that the CPB06 parameters represent the material behavior that is expected, and that the user subroutine can produce reasonable finite element solutions to problems with known solutions.
3. Understand the effects of various types of anisotropy on the stress-states of internally-pressurized tubes.
4. Develop FEA simulations of the hydroforming and irradiation process to determine whether LEU foil anisotropy is significant to the residual stresses seen in the target assembly during the manufacturing and irradiation process.

The completion of these objectives will ultimately answer the question of whether LEU foil anisotropy matters in the context of irradiation target manufacturing and use. The results will allow for scientists and engineers to design the irradiation target components and manufacturing process according to the true material properties demonstrated by LEU foil. Knowing the true strength properties of the foil could be significant to deciding upon the foil manufacturing process, assembly geometry, hydroforming pressures, or design of the surrounding components in order to achieve the final goal of producing an irradiation target which makes the process of target irradiation more efficient. Along the way, a method for fitting the CPB06 model parameters to plastically-anisotropic materials with known yield surfaces will be developed, allowing for others to easily implement the plastic anisotropy of materials into their own FEA simulations of materials which may be textured as in the case of LEU foils.

The goals of the *in situ* neutron diffraction conducted on various U-Mo alloys are slightly different, though they all relate back to the main theme of advancing LEU technology to replace HEU for nonproliferation purposes. The ultimate goal is to develop LEU fuel that is efficient (uranium-dense), yet stable during use in research reactors. The research in this thesis aims to complete the following goals, which will provide a small contribution to the larger research effort.

1. Use sequential Rietveld analysis to track the phase decomposition kinetics of U-10Mo and U-9.8Mo-0.2(Cr, Ni, Co) using *in situ* neutron diffraction data.
2. Use Rietveld analysis to collect phase fraction and texture data from *ex situ* neutron diffraction scans.
3. Determine the effectiveness of small additions of Cr, Ni, and Co as γ-U-Mo stabilizers.
4. Compare neutron diffraction results to SEM, EBSD, and x-ray diffraction data gathered at Pacific Northwest National Laboratory (PNNL) to tell a complete story of how Cr, Ni, and Co additions affected the phase stability of U-10Mo alloys based on the microstructural characteristics.

Successful completion of these goals is a small, but important step in developing a LEU nuclear fuel composition which is ideal for service in research reactors.

2. Part 1: Modeling of Anisotropic Uranium Foil and Medical Isotope Target Assembly

2.1 Development and Characteristics of LEU Foil Anisotropy

The texture of α-uranium foils was previously measured using a combination of x-ray and neutron diffraction [21]. X-ray diffraction was used to measure the texture near the surface of the material, and neutron diffraction was useful for determining the texture throughout the entire thickness of the foil. In addition, the strain history of cold, straight-rolled isotropic uranium was gathered from finite element modeling [1]. Subsequently, this strain history was used as an input to viscoplastic self-consistent (VPSC) polycrystal plasticity code to predict the anisotropic yield strength of the α-uranium foils [1]. The texture, or preferred crystallographic orientation of grains in the material, is typically the origin of such anisotropic material properties. Crystalline materials generally possess anisotropic properties in the single crystal form, especially those which are not cubic, such as orthorhombic α-uranium. When the bulk, polycrystalline material is comprised of many randomly-oriented grains, the effects of anisotropy are nullified and the polycrystal exhibits a net-isotropic behavior. However, once texture is introduced by a manufacturing process such as rolling, which causes a non-random grain-orientation distribution, the mechanical properties of the material change in each direction.

Prior work using EPSC and VPSC modeling found that most of the elastic properties did not deviate far from isotropy, but the plastic properties did exhibit anisotropy and a tension-compression strength differential [1, 22, 23]. Advantages of using a modeling approach such as VPSC are that it can predict the yield strength along any arbitrary straining direction, not just uniaxial loading along the material axes. In particular, it can predict the yield strength along axes which would normally be difficult to measure experimentally, such as tensile strength along the very small thickness of the foil. The results of the VPSC stress simulations were plotted in the π-plane. These results will be shown following a brief description of what the π-plane is and why it is useful for visualizing plastic anisotropy in the uranium foil.

Figure 3 demonstrates how the von Mises and Tresca yield criteria look plotted in principal stress space (σ_1, σ_2, and σ_3 are eigenvalues of the stress tensor). A yield criterion, sometimes referred to as a yield surface or yield locus, represents all of the multiaxial stress-states which will result in plasticity. Any stress-state inside the yield criterion will result only in elastic deformation, while stress-state at the boundary of the yield surface will result in plastic strain.

$$F - \sigma_y \leq 0 \qquad \text{(Eq. 1)}$$

Where σ_y is the yield strength along a predefined direction, such as the rolling direction. In principal stress space, the von Mises yield criterion presents itself as a cylinder whose axis is parallel to the hydrostatic axis (the line where $\sigma_1 = \sigma_2 = \sigma_3$). Along the hydrostatic axis, the shape of the yield criterion does not change. This is a result of the fact that hydrostatic pressure, $p = -\frac{1}{3}(\sigma_1 + \sigma_2 + \sigma_3)$ does not influence the plasticity of metals.

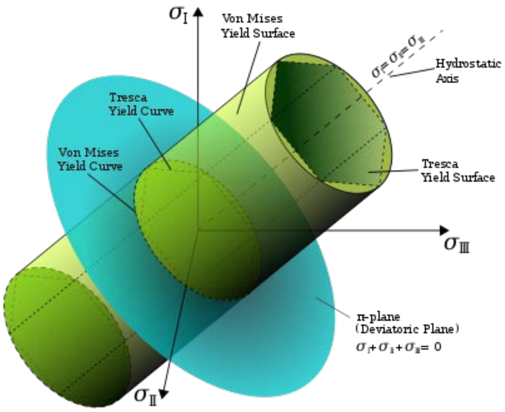

Figure 3. Von Mises and Tresca yield surfaces plotted in principal stress space [24]

In the figure above, the blue plane represents the π-plane. There is no pressure in this plane, meaning this plane contains all of the stress conditions for which $\sigma_1 + \sigma_2 + \sigma_3 = 0$. The von Mises yield criterion, the yield criterion of perfectly isotropic material, is circular in shape when projected onto this plane. The π-plane is a useful perspective for viewing anisotropic yield criteria since deviation from isotropic behavior along any direction will be immediately obvious. Therefore, this is the preferred perspective for a visual assessment of plastic anisotropy and tension-compression asymmetry.

The VPSC results for the anisotropic yield surface of the uranium foil are now shown plotted in the π-plane (Figure 4), where the principal stress axes are aligned with the RD, ND, and TD. The von Mises isotropic yield surface (black) is shown for comparison purposes. The yield surface for randomly-textured α-uranium (blue) is isotropic in that the strength in tension along each direction is the same, as is the strength in compression along each direction. However, the material displays slightly higher strength in compression than in tension along each direction. This is due to differences in the relative activity of slip and mechanical twinning in tension versus compression.

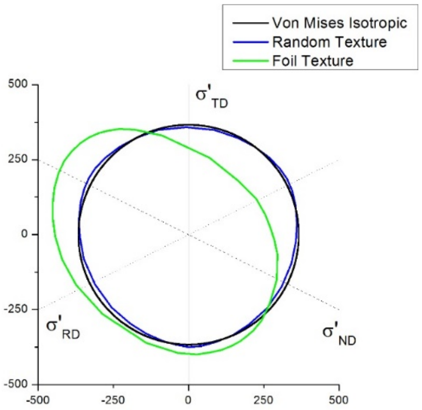

Figure 4. π-plane representation of the foil yield surface [1]

Based on the VPSC predicted yield surface of the foil, there is a clear difference in strength along each of the material directions when compared to the isotropic case. The most prominent properties are the increase in the compressive strength of the normal direction and a weakening of the compressive strength in the rolling direction. There is also a noticeable amount of asymmetry in the strength of the material in tension versus in compression. Along the ND and TD, the material is stronger in compression, and along the RD, it is much stronger in tension. Again, the asymmetric response is due to softer twinning modes being activated predominantly in either tension or compression, but not both. In order to account for the unique yield strength characteristics of the foil in a finite element simulation, a model must be chosen that can capture both the anisotropic (RD vs ND vs TD) and asymmetric (tension vs compression) differences in strength, and can be readily incorporated into finite element simulations using a user subroutine. The model that was chosen to capture this behavior is the analytical model of Cazacu, Plunkett and Barlat, hereafter referred to as the CPB06 model [2].

2.2 Introduction to the CPB06 Model for Plastic Anisotropy and Asymmetry

In order to properly incorporate the unique yield behavior of the uranium foil in finite element simulations, the CPB06 model was employed. CPB06 is a yield-criterion that contains parameters which can be altered to generate an asymmetric, anisotropic yield surface in 6D stress space. The master function for the yield criterion is as follows:

$$F = (|\Sigma_1| - k \cdot \Sigma_1)^a + (|\Sigma_2| - k \cdot \Sigma_2)^a + (|\Sigma_3| - k \cdot \Sigma_3)^a \qquad \text{(Eq. 2)}$$

In this function, which ultimately describes the size and shape of the yield surface, F is the parameter which controls the size of the yield surface. The exponent a controls the sharpness of the “corners” in the yield function and k dictates the ratio of tensile to compressive strength.

$\Sigma_{1,2,3}$ are eigenvalues of the Σ matrix, which will later be shown to depend on the deviatoric stress tensor and a matrix of anisotropy coefficients. First, in order to understand how tension-compression asymmetry is accounted for in this model, the following equations will demonstrate how the ratio of tensile to compressive strength is incorporated into a single variable, *k*. σ_T and σ_C are the uniaxial yield strengths along a particular direction in tension and compression, respectively.

$$k = \frac{1-h\left(\frac{\sigma_T}{\sigma_C}\right)}{1+h\left(\frac{\sigma_T}{\sigma_C}\right)} \qquad \text{(Eq. 3)}$$

$$h\left(\frac{\sigma_T}{\sigma_C}\right) = \left[\frac{2^a-2\left(\frac{\sigma_T}{\sigma_C}\right)^a}{\left(2\frac{\sigma_T}{\sigma_C}\right)^a-2}\right]^{\frac{1}{a}} \qquad \text{(Eq. 4)}$$

When the value of *k* is positive, the material will have higher strength in tension than in compression, and when *k* is negative, it will have higher compressive strength, similar to the randomly textured uranium. A value of zero means that the material is equally strong in tension and compression. While the *k* term accounts for the asymmetric portion of the yield stress response, the anisotropy is controlled by a matrix of coefficients. These coefficients, contained in a matrix [C], are used to perform a linear transformation on the deviatoric stress tensor [S] to yield [Σ] (see Eq. 5). Deviatoric stresses are the stresses which remain after the hydrostatic pressure is removed, since again the hydrostatic pressure does not affect the plasticity of metals.

$$\Sigma = C[S] \qquad \text{(Eq. 5)}$$

$$C = \begin{bmatrix} C_{11} & C_{12} & C_{13} & & & \\ C_{12} & C_{22} & C_{23} & & & \\ C_{13} & C_{23} & C_{33} & & & \\ & & & C_{44} & & \\ & & & & C_{55} & \\ & & & & & C_{66} \end{bmatrix} \qquad \text{(Eq. 6)}$$

Provided *a* = 2 and there is no anisotropy $\left(C_{11} = C_{22} = C_{33} = C_{44} = C_{55} = C_{66} = 1; C_{12} = C_{13} = C_{23} = 0.5; all\ other\ C_{ij} = 0\right)$, the criterion will simplify to the von Mises case. In order to represent the anisotropic and asymmetric properties of the yield strength of cold-rolled uranium foil, the values of *k* and all C_{ij} components of the anisotropy matrix must be determined. This was accomplished with a MATLAB code which was used fit the CPB06 yield function to the VPSC predicted yield surface.

In this MATLAB program, an initial guess is made for the values of the CPB06 parameters. Based on these parameters, the effective stress is calculated for each of the 36 stress-states for which the VPSC calculation predicted yield values. These stress-states correspond to 36 equally-spaced straining directions in the π-plane. Since the straining direction is always perpendicular to the surface of a yield criterion (this is known as the normality rule), the 36 points which are equally-spaced in strain-space will not be equally-spaced in stress-space unless the material is isotropic. For each of these 36 data points, an optimization routine in MATLAB was used to then minimize the amount of error between the values of effective stress for each straining direction.

$$\boldsymbol{\chi^2 = \sum_{i=1}^{36} \left(\frac{F_i}{\sigma_0} - 1\right)^2} \qquad \text{(Eq. 7)}$$

In this error function, F_i is the value of the yield function at the i^{th} stress-state and σ_0 is the yield stress predicted by VPSC along the RD, here used as a normalization factor. The parameters were subjected to constraints ($0 < C_{ij} < 10$ and $-1 < k < 1$). The values for the parameters which resulted in the best fit are shown in Table 1. The C_{ij} values are normalized with respect to C_{11}. The shear-related terms C_{44}, C_{55}, and C_{66} are all equal to 1 in this case, since the simulation goals did not involve shear loading conditions.

Table 1. Values of CPB06 parameters used to describe the LEU foil.

C_{11}	C_{12}	C_{13}	C_{22}	C_{23}	C_{33}	k
1	2.65	2.82	2.86	3.97	2.69	-0.222

In order to plot the CPB06 yield function, an initial value for the size of the yield criterion, F, is determined using Equation 2 with the previously determined values for a, k, and C_{ij}. This initial value is calculated for the first stress-state, which lies directly on the RD axis. This axis was designated in the MATLAB script as corresponding to $\theta = 0^{o}$. Each of the next points in the plot were then calculated in increments of 5^{o} until $\theta = 355^{o}$. Since F is constant for a given yield surface, for each of the next points, a value of the radius of the yield surface at that point was calculated by redefining the deviatoric stresses in terms of r and θ and solving for a value of r that matched the initially determined value of F. The points were then converted from values of r and θ into 2D Cartesian coordinates to be plotted in the π-plane.

For the present scenario, the 11 stressing or straining direction was chosen to correspond to RD, 22 with ND, and 33 with TD. The negative value of the k parameter indicates that this material tends to have a higher strength in compression than in tension. This agrees with the yield surface that was shown previously, which has higher compressive strength in the ND and TD directions. Figure 5 shows a comparison between the yield surface generated by the CPB06 model using the parameters revealed with the MATLAB script, and the yield surface gathered from VPSC simulations.

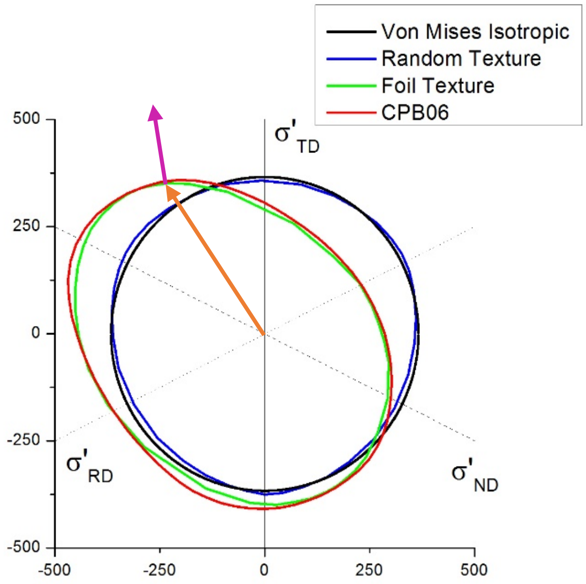

Figure 5. Yield surface comparison between the VPSC and CPB06 models

During the simulations of the medical isotope target assembly process, the LEU foil material will be subjected to internal pressure which will cause the development of compressive stresses in the ND (parallel to the radial direction) and tensile stresses in the TD (parallel to the tube hoop direction). For example, the orange arrow in Figure 5 indicates a stress direction in which equal stress is exerted along ND-compression and TD-tension. The purple arrow indicates the straining direction which the foil material will undergo in response to this type of loading (a manifestation of the aforementioned normality rule). The difference in direction of these two arrows is a manifestation of the anisotropy of the material. Note that the stressing and straining directions would be parallel for the isotropic yield surface. Upon plastic straining, the yield surface expand according to the hardening rule employed, as discussed below.

The current model assumes that the material hardens in an isotropic manner. This means that with larger strain levels, the yield-surface will grow larger, but does not change its shape.

Some more complex models incorporate evolving yield surfaces which account for the further development of anisotropy during straining [25]. Modeling evolving yield surfaces requires yield surface data to be generated for many strain levels. Since it is predicted that the LEU foil will not see large amounts of strain during the target-forming simulation, isotropic hardening is a fair simplifying assumption, which will be examined below. Isotropic strain-hardening was modeled using Equation 8. Y_0 is the initial yield strength along the RD in tension. The values of the hardening parameters were determined by fitting this equation to the VPSC data gathered for tension up to 20% strain along the RD direction.

$$Y(\bar{\epsilon}_p) = Y_0(1 + K\bar{\epsilon}_p)^n \tag{Eq. 8}$$

2.3 Validation of the CPB06 Model and VUMAT Subroutine

In order to implement the anisotropy and asymmetry parameters found during the CPB06 modeling into finite element simulations, a user subroutine known as a VUMAT was used. The VUMAT was developed by Williams and Sinha [26] and uses the CPB06 model as the basis for the material behavior of 3D brick elements in ABAQUS/Explicit. During a particular time step in a FEA simulation, the VUMAT determines whether each element is within the bounds of the yield surface, and is therefore elastic, or at the boundary of the yield surface, and will therefore strain in the direction normal to the yield surface and harden accordingly. If the element achieved plasticity during a particular time step, during the next iteration the VUMAT will recalculate the yield surface for the particular degree of hardening achieved.

Before using the VUMAT to approach the ultimate LEU target assembly problem, simpler finite element simulations were performed for benchmarking purposes. A benchmarking strategy was used in the early stages of research for two very important reasons:

1. Ensure that the anisotropy and asymmetry parameters used in the VUMAT provide a material response which is consistent with the behavior predicted by VPSC modeling.
2. Ensure that the VUMAT can be used to accurately produce finite element solutions which match known results to a theoretical problem for the isotropic case.

Acting on the first benchmarking goal, a series of simple finite element simulations were done using single elements to test the strength of the finite element material in tension and compression. The stress-response of the finite element material point should match the behavior predicted by the CPB06 yield surface. Figure 6 shows an example of the single element used before any simulations are done. The material axes were assigned such that the 1/X direction corresponds to the RD, 2/Y corresponds to the ND, and 3/Z corresponds to the TD. The stacking direction (S) simply shows the direction in which further meshing elements would be generated but is irrelevant to the calculations or results of the simulation.

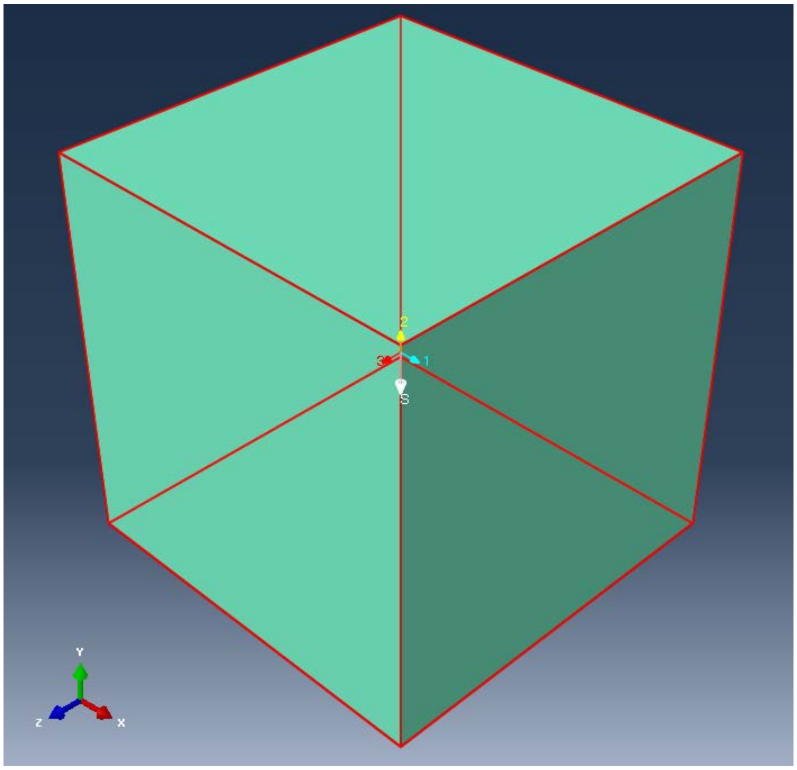

Figure 6. Visual of a single element with a user-defined material orientation.

For this work, a single 3D stress, linear shape function, and reduced-integration element was used. This is the same element type that is eventually used in the LEU target assembly. This element was assigned the material properties of the foil, listed in Table 2.

Table 2. Material parameters used in CPB06 VUMAT

MATERIAL CONSTANTS	
YOUNG'S MODULUS (E)	208 GPa
POISSON'S RATIO (ν)	0.23
STRENGTH COEFFICIENT (K)	155 MPa
STRAIN-HARDENING EXPONENT (n)	0.14
DENSITY (ρ)	18.9 g/cm^3
CPB06 PARAMETERS	
F (yield strength in RD)	403 MPa
k	-0.22212
a	2
C_{11}	1
C_{12}	2.6461
C_{13}	2.8173
C_{22}	2.8563
C_{23}	3.9708
C_{33}	2.6907
C_{44}	1
C_{55}	1
C_{66}	1

These simulations were designed to provide a uniaxial stress-strain response for tension and compression along the rolling, normal, and transverse directions. A boundary condition was applied to one face of the element which moves that face at a velocity which corresponds to 20% engineering strain per second. The particular velocity is insignificant since the material model is strain-rate-independent. A value of 20% strain was used because the material achieved a strain-level of 20% in the VPSC simulations used for comparison.

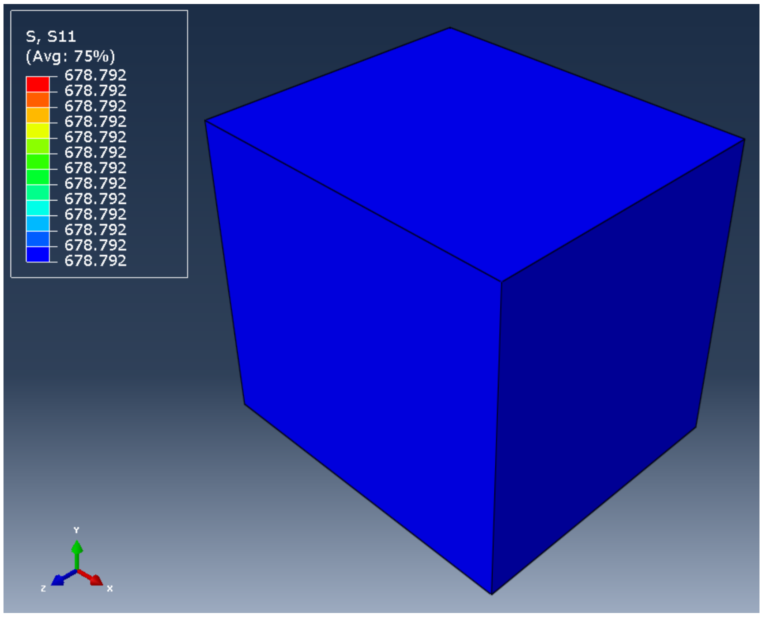

Figure 7. Element showing stress accumulated after 20% tension in the RD

The stress-strain relationship for tension and compression along each of the directions was captured by reporting the stress value at various increments in the experiment. Figure 8 shows a summary of the results. The strength of each of the direction and loading condition combinations is ranked in order of strongest to weakest from left to right in the legend of the plot. The results of these simulations were also compared to similar results from VPSC simulations (Figure 9).

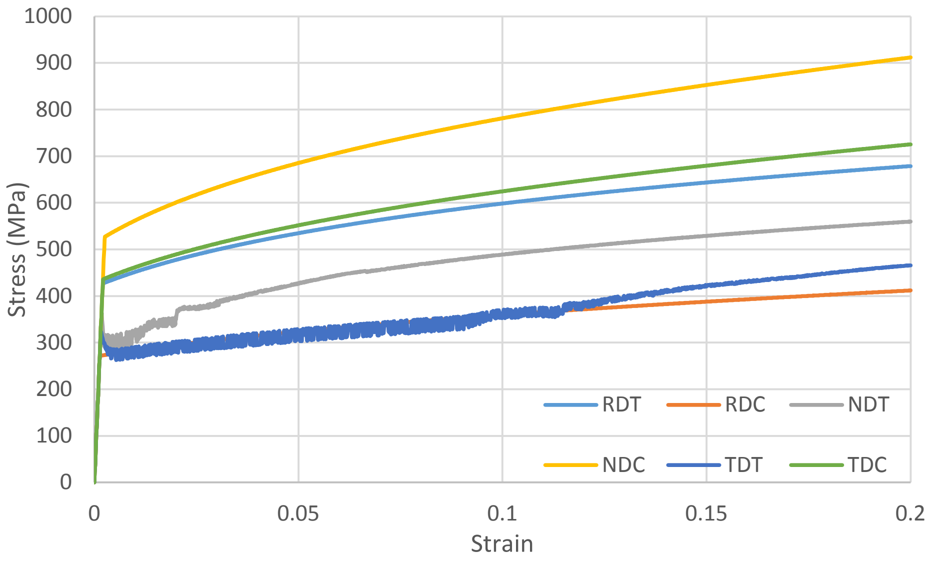

Figure 8. Stress-strain curves for single-element simulations (RD, ND, and TD in tension, T, or compression, C)

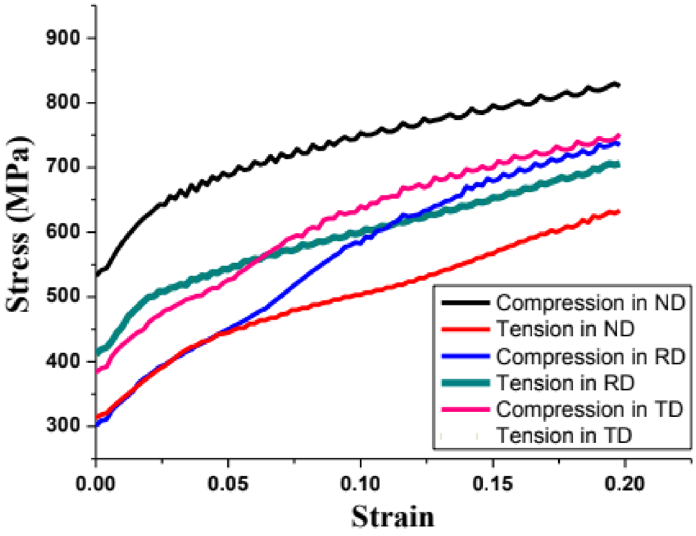

Figure 9. VPSC results for stress-strain relations in each direction [27]

The FEA results show that the ordering of the strength of these combinations of tension and compression along the RD, ND, and TD is consistent with the order that is observed from the CPB06 and VPSC yield surfaces. In other words, the anisotropy of the CPB06-based finite element material is consistent with the intended material behavior predicted by the VPSC code. The optimization of the CPB06 parameters and implementation of these parameters in a finite element subroutine were successful.

As stated before, for proper benchmarking, the VUMAT was benchmarked against a simple problem with a known solution, signifying that it can be used to produce reliable answers to more complex finite element problems. For this project, the VUMAT was used to predict the elasto-plastic behavior of internally-pressurized, isotropic thick-walled tubes [28]. Thick-walled tubes were chosen as the subject of study because they are similar to the geometry of the final medical isotope target problem, and in addition to benchmarking, this study could also help develop a basic understanding of how various kinds of anisotropy can affect the hoop, radial, and axial stresses in such a cylindrical system.

Theoretical solutions to thick-walled tube stress calculations using both Tresca and von Mises yield theories (the latter elasto-plastic constitutive rule is often attributed to Prandtl and Reuss) were held as the standard for comparison when obtaining solutions to finite element problems regarding yielding in non-hardening, thick-walled tubes. The following diagram (Figure 10) depicts a simple thick-walled tube under internal pressure. The stress due to pressure has caused the tube to partially yield, with an elasto-plastic boundary (dotted line) between the yielded and unyielded material.

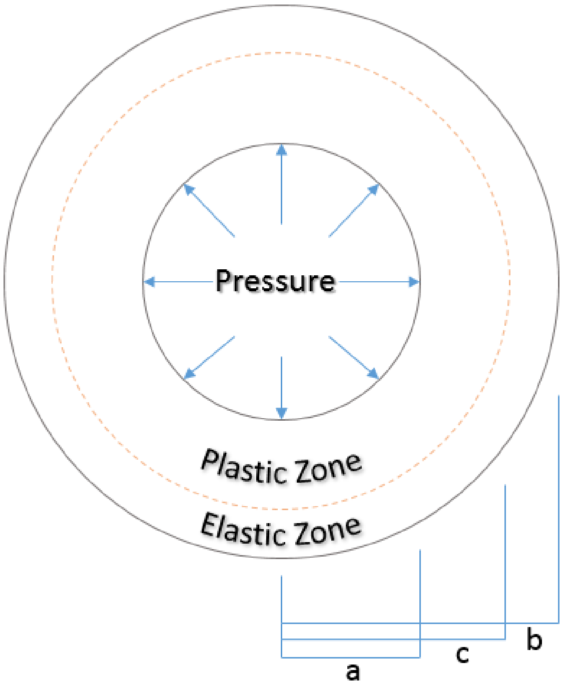

Figure 10. Geometry of an internally-pressurized thick-walled tube

The thick-walled tube has three important dimensions: the internal radius, *a*, the outer radius, *b*, and the radius at which the elasto-plastic boundary is located, *c*. As the internal pressure increases, the amount of material that has yielded increases. For the case of a tube in plane strain, the radial and tangential stresses in both the elastic and plastic regions of the tube can be determined as a function of the location of the plastic boundary and the location of interest for the stress calculation. Thick-walled tubes can be modeled as open-end, closed-end, or plane strain. Plane strain was chosen for the purposes of this modeling since it the LEU target assembly will later also be modeled under the plane strain assumption. By making the plane strain assumption, it is assumed that the tubes will be long enough that any effects due to the end-geometry of the tube will have no bearing on the stress-state in the middle of the tube. For a thick-walled tube under plane strain, there are several equations which are used to determine the state of stress. The equations governing the Tresca yield criterion will be outlined first, since they can be solved analytically.

In the elastic region:

$$\sigma_r = \frac{-kc^2}{b^2}\left(\frac{b^2}{r^2} - 1\right) \qquad \text{(Eq. 9)}$$

$$\sigma_\theta = \frac{kc^2}{b^2}\left(\frac{b^2}{r^2} + 1\right) \qquad \text{(Eq. 10)}$$

$$\sigma_z = 2\nu k\frac{c^2}{b^2} \qquad \text{(Eq. 11)}$$

In the plastic region:

$$\sigma_r = -k\left(1 - \frac{c^2}{b^2} + ln\frac{c^2}{r^2}\right) \qquad \text{(Eq. 12)}$$

$$\sigma_\theta = k\left(1 + \frac{c^2}{b^2} - ln\frac{c^2}{r^2}\right) \qquad \text{(Eq. 13)}$$

$$\sigma_z = 2\nu k\left(\frac{c^2}{b^2} - ln\frac{c^2}{r^2}\right) \qquad \text{(Eq. 14)}$$

The pressure which causes a particular degree of yielding:

$$p = k\left(1 - \frac{c^2}{b^2} + ln\frac{c^2}{a^2}\right) \qquad \text{(Eq. 15)}$$

In these equations, *r* is the radius at which the stress-state is being calculated. *k* is the yield stress of the material in pure shear, or the uniaxial yield stress of the material in tension divided by $\sqrt{3}$. Using these equations, the predicted stress-state throughout the thickness of a thick-walled tube was plotted. When materials yield according to the von Mises criterion rather than Tresca, then the Prandtl-Reuss theory can be used to solve for the stresses seen in the plastic region. For plane strain ($\varepsilon_z = 0$), the equations governing the behavior of a thick-walled tube are the following:

$$\sigma_r = -kN\left(\frac{b^2}{r^2} - 1\right) \tag{Eq. 16}$$

$$\boldsymbol{\sigma_\theta = kN\left(\frac{b^2}{r^2} - 1\right)} \tag{Eq. 17}$$

$$\boldsymbol{\sigma_z = 2k\nu N} \tag{Eq. 18}$$

$$\varepsilon_r = \frac{kN}{2G}\left(1 - 2\nu - \frac{b^2}{r^2}\right) \tag{Eq. 19}$$

$$\varepsilon_\theta = \frac{kN}{2G}\left(1 - 2\nu + \frac{b^2}{r^2}\right) \tag{Eq. 20}$$

$$N = \left[\frac{1}{3}(1 - 2\nu)^2 + \frac{b^4}{c^4}\right]^{-1/2} \tag{Eq. 21}$$

$$d\varepsilon_\theta = \frac{\varepsilon_r - \varepsilon_\theta}{r}dr \tag{Eq. 22}$$

$$d\varepsilon_r = \frac{\left\{G\left(\frac{2}{3} + \frac{s_r s_\theta}{k^2}\right) - K\right\}d\varepsilon_\theta + \frac{1}{2r}\left(-3s_r + \sqrt{4k^2 - 3s_r^2}\right)dr}{G\left(\frac{4}{3} - \frac{s_r^2}{k^2}\right) + K} \tag{Eq. 23}$$

$$ds_r = G\left(\frac{4}{3} - \frac{s_r^2}{k^2}\right)d\varepsilon_r - G\left(\frac{2}{3} + \frac{s_r s_\theta}{k^2}\right)d\varepsilon_\theta \tag{Eq. 24}$$

$$s_\theta = \frac{1}{2}(-s_r + \sqrt{4k^2 - 3s^2} \tag{Eq. 25}$$

$$\sigma_r = s_r + K(\varepsilon_r + \varepsilon_\theta) \tag{Eq. 26}$$

$$\sigma_\theta = s_\theta + K(\varepsilon_r + \varepsilon_\theta) \tag{Eq. 27}$$

$$\sigma_z = -(s_r + s_\theta) + K(\varepsilon_r + \varepsilon_\theta) \tag{Eq. 28}$$

Unlike the case of Tresca yielding, this system of equations cannot be solved analytically. As such, the finite difference method was employed using a FORTRAN code to solve for the stresses in the thick-walled tube using Prandtl-Reuss equations [29]. The process for solving for the stresses using the finite difference method is as follows:

1. Set a value for c, the elasto-plastic boundary. In this case c will be set to the outer radius to start.
2. Calculate N.
3. Calculate the stresses and strains in terms of r, then solve for the stresses and strains at $r = c$.
4. Calculate $d\varepsilon_\theta, d\varepsilon_r, ds_r$ at $r = c - dr$.
5. Update the values of $\varepsilon_\theta, \varepsilon_r, s_\theta, ds_r$ at $r = c - dr$.
6. Solve for the stresses $\sigma_r, \sigma_\theta, \sigma_z$ using Equations 25-27.
7. Repeat steps 5 and 6 until $r = a$.

Finite element simulations using the CPB06 VUMAT were performed for the same boundary conditions. Though the plane strain thick-walled tube is a problem which could be easily modeled in 2D with lower computation time, it was modeled with 3D stress elements using the CPB06 VUMAT. The element type used was a 3D stress, 8-node linear brick with reduced integration and hourglass control. The tube was created with the inner radius one-half that of the outer radius. 51 elements were used through the thickness and around the circumference of the quarter tube for a total of 2,551 elements. This number of elements allowed for a solution approaching the solution which would be reached with a very large number of elements, but with less computation time. It also allowed for enough integration points to obtain a comprehensive amount of precise data from measurements taken at each element or node along the geometry of the tube. Quarter symmetry was employed to reduce computation time, and the thickness of the model only needed to be one element thick in the axial direction due to the plane strain conditions leading to uniform axial stress through the length of the tube.

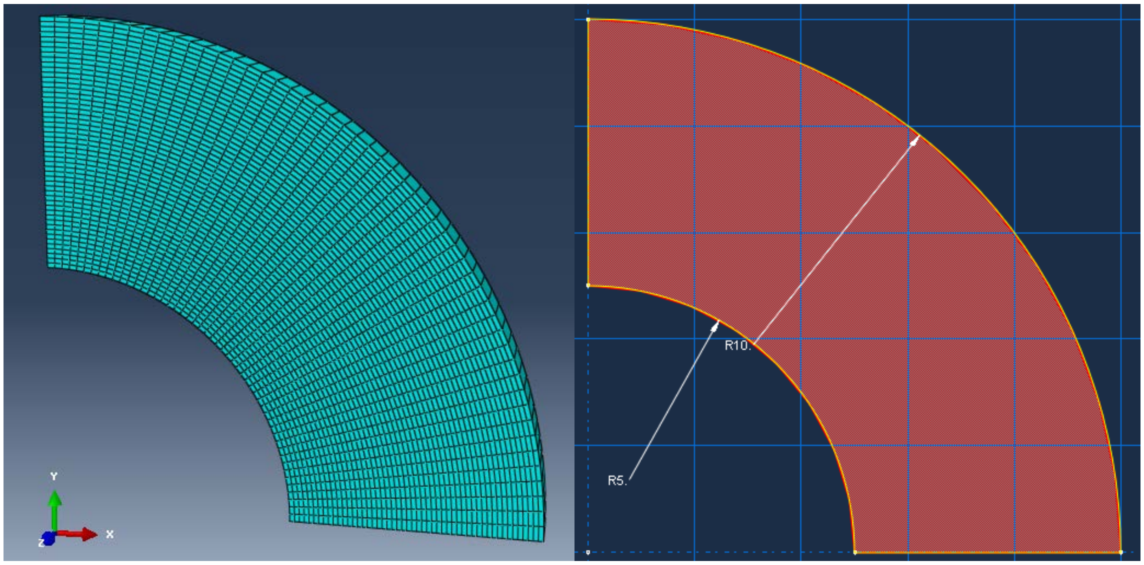

Figure 11. Meshing and geometry schematics for the thick-walled tube

In order to employ the VUMAT, the material directions had to be assigned to the part. Figure 12 below shows how the material axes were assigned to the part so that the rolling direction (1) is in line with the length of the tube, the normal direction (2) is aligned with the thickness, and the transverse direction (3) is aligned with the circumference. This was accomplished using the “orientation” feature under the part description in ABAQUS. The 1 direction was designated to be normal to the front face, and the 3 direction was designated to point along the outer circumference, which resulted in the coordinate system shown. Assigning the directions in this manner allowed for the anisotropic properties of the material to be assigned such that the part behaves like a metal sheet rolled into a tube, with the material axes aligning with the axial, radial, and tangential directions. The element stacking direction (S) is also illustrated but is not significant to the numerical results of the simulation.

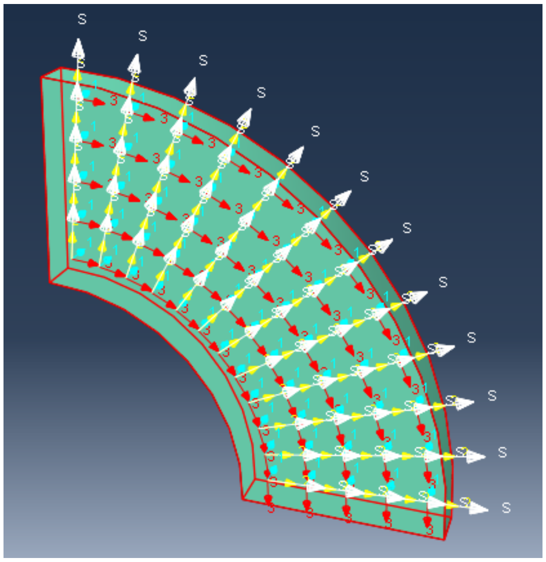

Figure 12. Quarter-section of thick-walled tube with material orientation

Other than symmetry in the X and Y directions, a plane strain boundary condition was applied. This boundary condition specified that there is zero displacement along the axial direction for the whole tube. A dynamic, explicit step type was chosen, since this is required for the VUMAT. During this step, pressure was ramped linearly to a final value of 88.03 MPa, the minimum pressure calculated to cause yielding through the entire thickness of a thick-walled tube with an isotropic yield strength of 110 MPa, the same yield strength that will be used in many of the LEU foil simulations. For this simulation, the VUMAT was first used with isotropic and symmetric parameters $\left(C_{11} = C_{22} = C_{33} = C_{44} = C_{55} = C_{66} = 1; C_{12} = C_{13} = C_{23} = 0.5; all\ other\ C_{ij} = 0; k = 0; a = 2\right),$ for which the model is identical to the von Mises yield criterion. The hardening coefficient was also set equal to zero, consistent with the above Tresca yield solutions for a non-hardening material. In short, the FEA software will solve the problem consistent with the Prandtl-Reuss equations.

In Figure 13, the Mises stress-states of the tube at 20% and 60% yielding are shown. Red denotes that section of the tube which has reached the yield stress value of 110 MPa. The gradient to blue denotes a regions over which the material remains elastic. The stresses seen through the thickness of the tube in FEA were plotted against the Tresca solutions for yielding at 0%, 20%, 40%, 60%, and 100% of the tube radius with good agreement. In these plots (Figure 14), the Tresca solutions are seen as solid lines, and the finite element (FE) results are dashed. Notice slight deviation in the solutions which is most obvious near the inner radius.

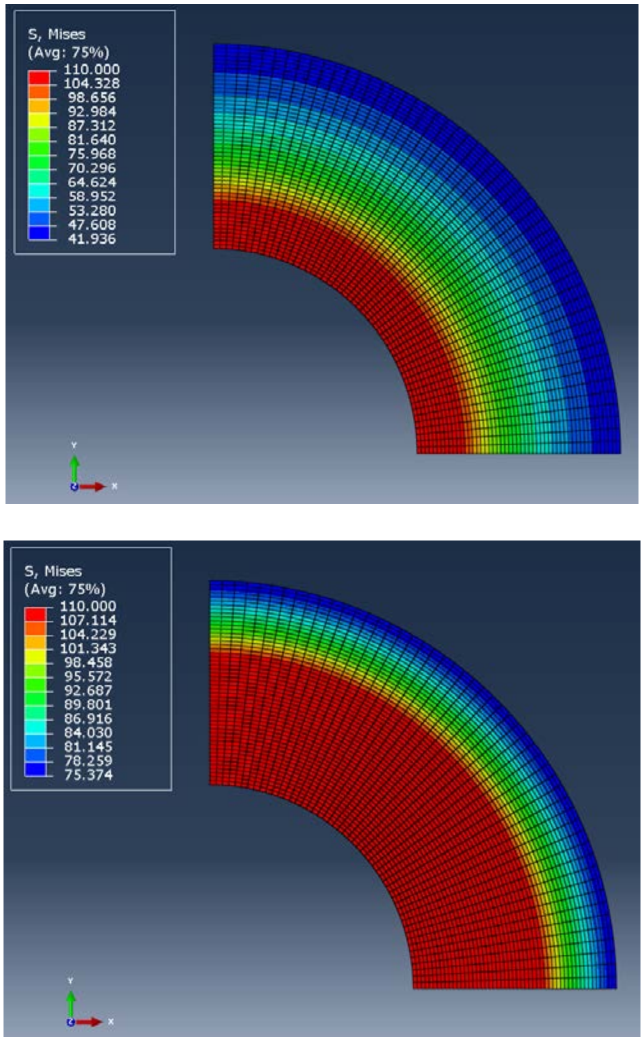

Figure 13. Mises stress-state for the thick-walled tube at 20% yielding (top) and 80% yielding (bottom) with yield strength = 110 MPa

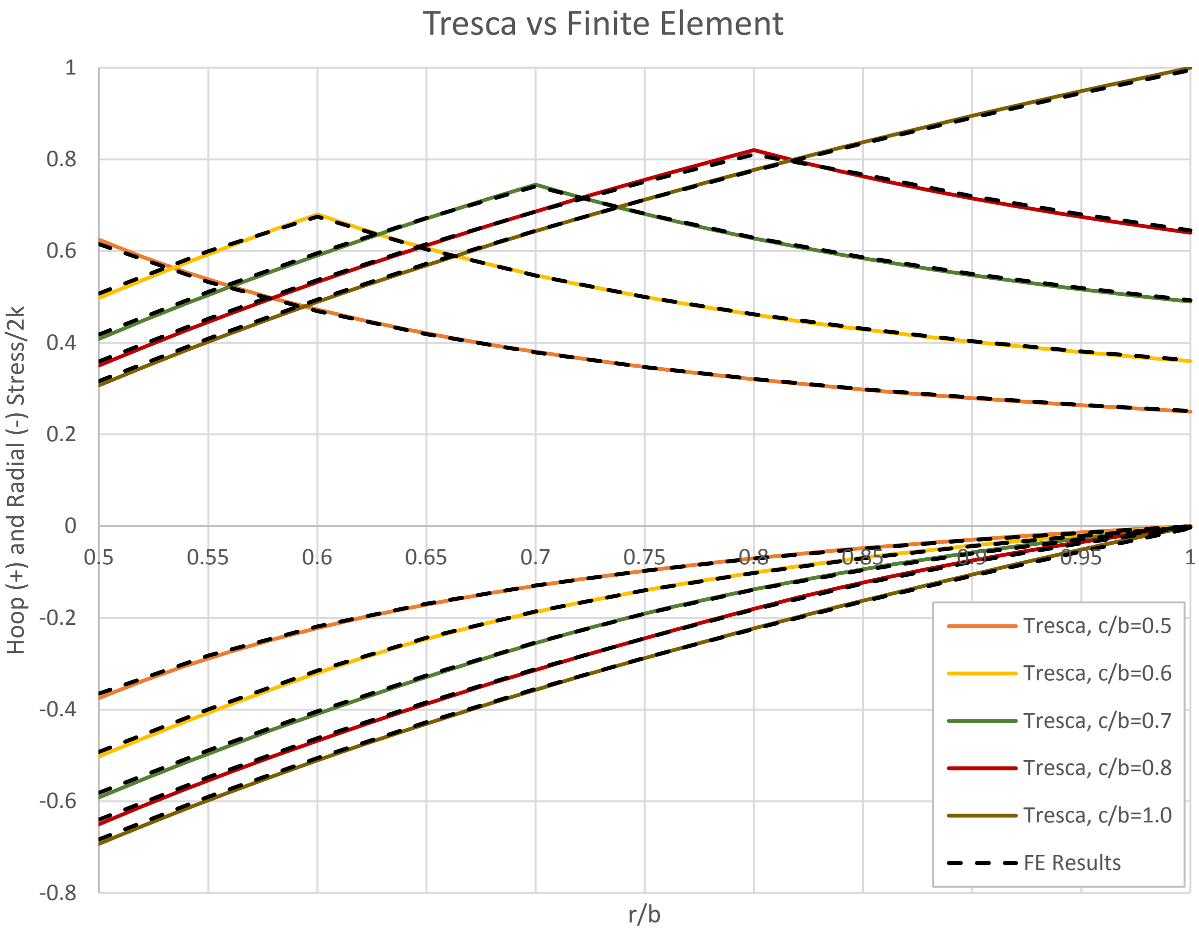

Figure 14. Comparison of Tresca and finite element (FE) solutions for radial and hoop stresses in a thick-walled tube at various levels of plasticity

A comparison of the finite difference and finite element solutions employing the Prandtl-Reuss equations is shown in Figure 15. Here, the agreement is precise. Any disagreement is due to numerical error, given the fact that the same constitutive rule is employed to solve the same set of boundary conditions.

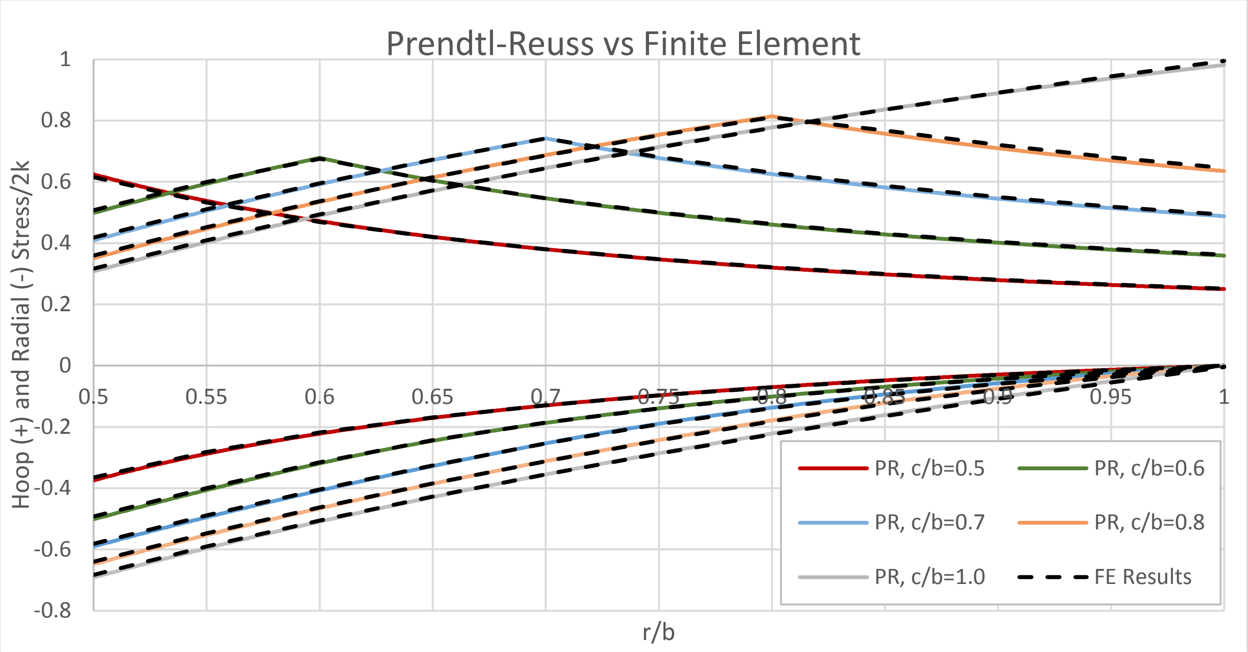

Figure 15. Finite difference solutions to hoop and radial stresses within the internally pressurized thick-walled tube employing Prandtl-Ruess (PR) equations compared with finite element solutions employing the CPB06 VUMAT with isotropic parameters.

The agreement between the two solution methods provides confidence that the VUMAT was successfully implemented in the finite element simulation. Combined with the previous results for single elements under imposed uniaxial stressing conditions, the VUMAT has been proven to reliably produce results that are consistent with theoretical models and reproduce the strength levels anticipated from the LEU foil material.

2.4 Effects of Anisotropy in Thick-Walled Tubes

Once the VUMAT had been proven to reliably incorporate the anisotropy model in the commercial finite element software, a series of simple simulations were used to experiment with how various types of anisotropy would affect the stress-state in thick-walled tubes. Using the perfectly isotropic case as a base-line, simulations were performed which would test how in-plane and out-of-plane asymmetry would affect an internally pressurized tube. Finally, a tube with the anisotropic and asymmetric properties of the LEU foil was considered.

Table 3. Outline of thick-walled tube experiments

	Out-of-plane isotropic	**Mild out-of-plane anisotropy**
In-plane isotropic	Perfectly Isotropic	Stronger along ND
Mild in-plane anisotropy	Stronger along TD or Stronger along RD	Actual Foil Properties

For these simulations, the pressure was ramped linearly to a final pressure of 88.03 MPa, just as in the isotropic, non-hardening case. This way, the stress behavior can be compared across various types of plastic strength for equivalent loading conditions, though the anisotropic and hardening materials may not see the same level of plasticity. For the hardening materials, the following hardening scheme for isotropic uranium was used (K=1,140 MPa, n=0.23, σ_0=110 MPa, see (Eq. 8)).

From the von Mises stress-states of the various tube types (Figure 16), it is apparent that an increase in strength along the transverse direction (aligned with the hoop direction) increased the overall strength of the tube the most, and an increase in the strength along the normal direction increased the strength nearly as much. This is to be expected, since, as demonstrated earlier, the largest stresses seen in internally-pressurized tubes are tension of the hoop direction and compression of the radial direction. Beyond this, the tube with the foil properties behaved very similarly to the isotropic material. Otherwise, the elasto-plastic boundary is at the lowest percent of the overall radius for the case of the strong TD tube. Due to strain hardening, the stresses in the plastic zone are higher than the stresses in the elastic zone. Increasing the strength along the normal direction had a very similar, but slightly smaller effect on the overall resistance to plasticity during internal pressurizing of the tubes. When the strength in the rolling direction was increased, the strength of the material decreased slightly from the isotropic case as can be seen by less of the stress being bared in the plastic section, and more stress being bared in the elastic region. These same results are reflected in the hoop, radial, and axial stresses (Figure 17 - Figure 19).

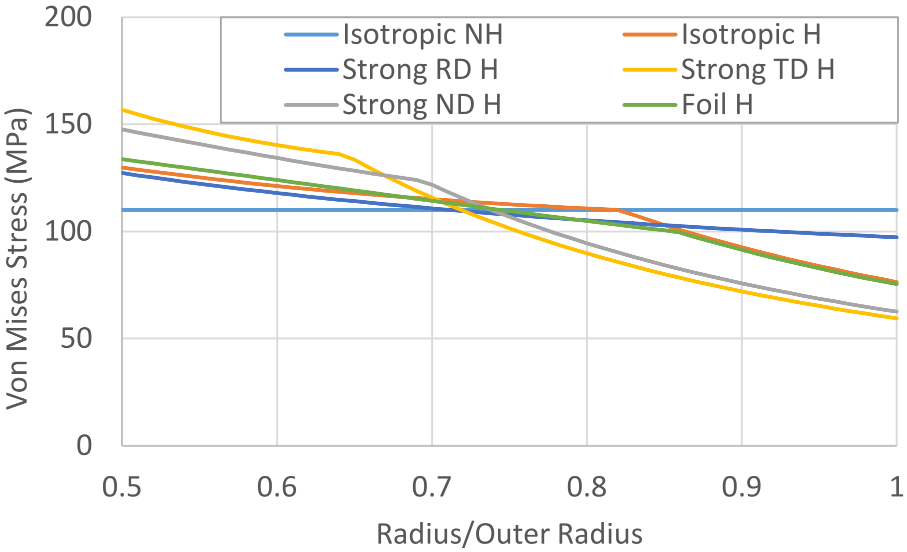

Figure 16. Comparison of von Mises stress in six tubes with varying anisotropy (NH denotes non-hardening and H denotes isotropic hardening)

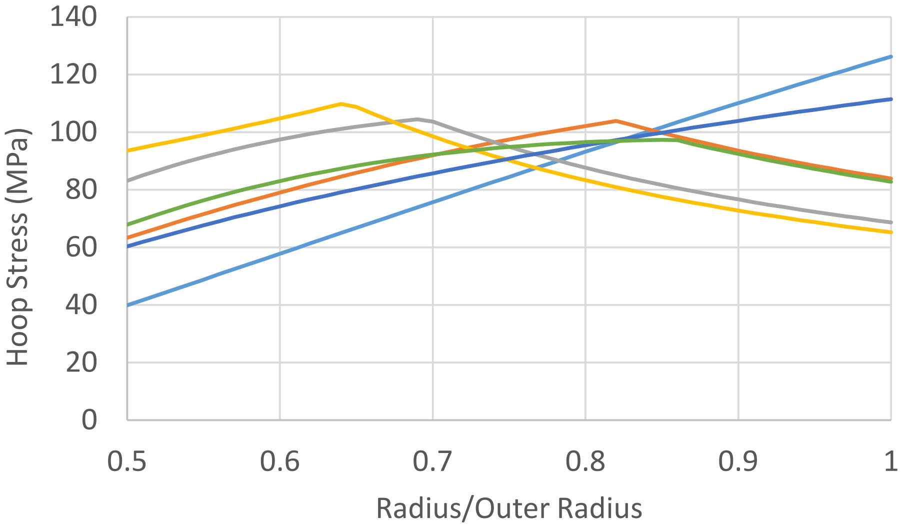

Figure 17. Hoop stresses in thick-walled tubes

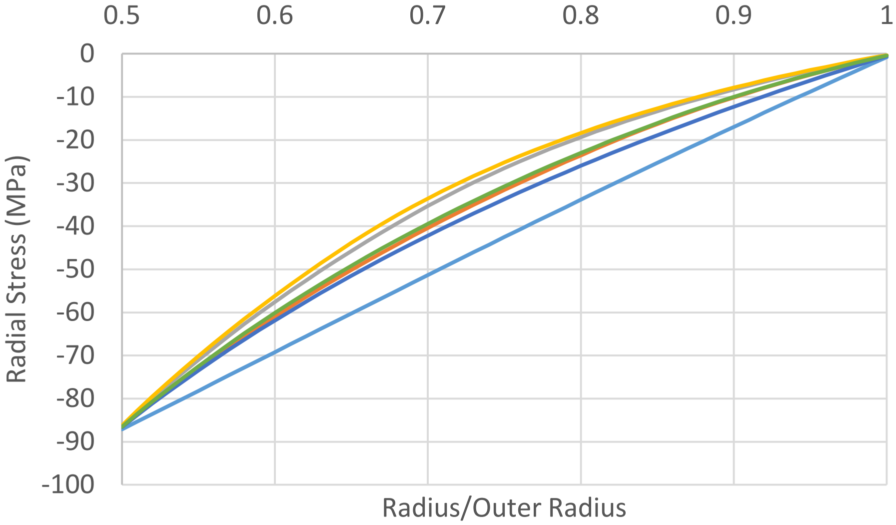

Figure 18. Radial stresses in thick-walled tubes

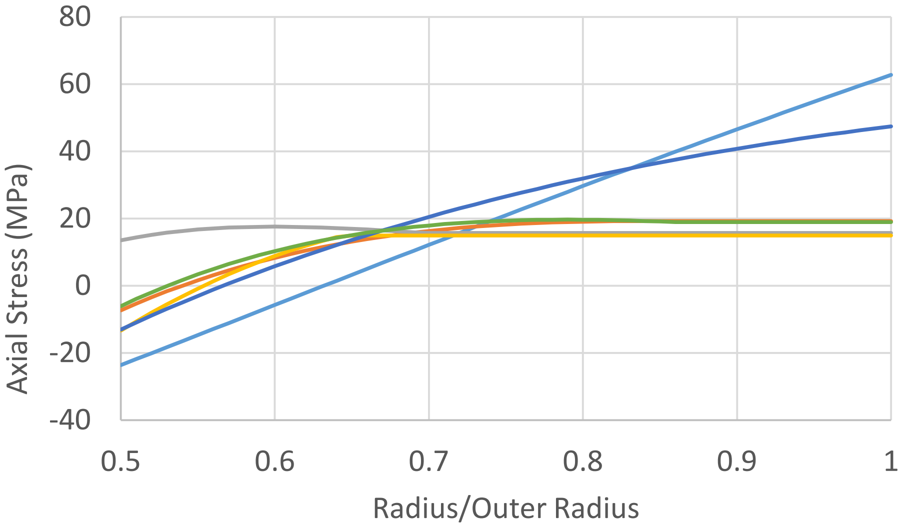

Figure 19. Axial stresses in thick-walled tubes

From these results, it is clear that the anisotropic foil is predicted to respond to internal pressures similar to the isotropic foil used in previous finite element models of the Tc-99m target assembly. Internally-pressurized tubes will experience compressive stresses along the radial direction, and tensile stresses along the hoop (transverse) direction. *Since the foil material has higher strength in the compressive normal direction, but a decrease in strength along the tensile transverse direction, it seems that the effects of anisotropy were neutralized for this particular loading condition.* Though the foil-type anisotropy did not have a tremendous effect on the stress-state for internally-pressurized thick-walled tubes, it did have a clear effect on the single elements subjected to various uniaxial loads. At this stage, it is difficult to tell if anisotropy will have a significant result on the outcome of the target assembly simulations. The complexity of the simulation will increase due to the use of multiple parts with differing material properties.

2.5 Simulation of Hydroforming of LEU Foils during Target Assembly

Previous efforts to use finite element analysis to study the assembly irradiation of LEU foil for production of Tc-99m were a large step in starting the research conversation in this area [13]. However, as seen earlier, the texture of α-U LEU foils makes certain mechanical properties anisotropic, namely the plastic stress-behavior. It must be determined whether the anisotropy of the foil will have a significant effect on the resulting stress-state of the target assembly. The geometry of the problem, as well as the details of the simulation steps (pressure application, pressure relaxation, and irradiation) will now be discussed.

As described in reference [13], the Tc-99m target assembly, pictured earlier in Figure 2, and below in Figure 20, is composed of concentric aluminum 6061-T6 tubes containing a thin LEU foil. The foil is wrapped around the smaller tube, and a gap of 128 microns exists between the foil and the outer tube. A gap between the ends of the foil, known as the foil relief, exists near the bottom of the assembly and the gap between the foil ends resides in a 45° arc from the center of the tubes. Due to the geometry of the problem, a boundary condition for symmetry in the x-direction was able to be used, which reduces the number of necessary elements by half.

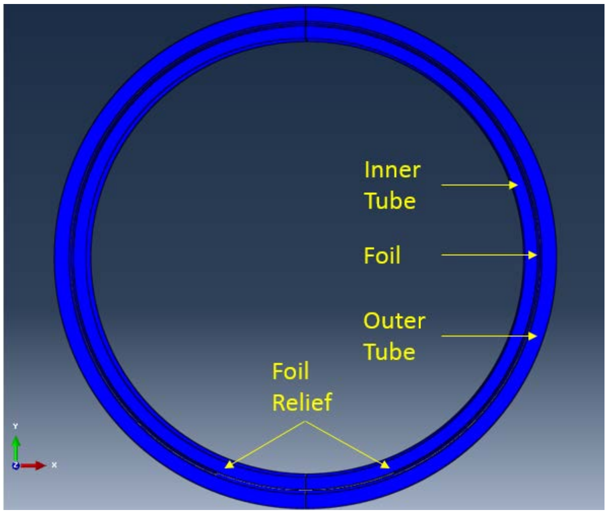

Figure 20. Schematic of target assembly

Table 4. Measurements of target assembly components

Part	Inner Radius (mm)	Outer Radius (mm)	Total Thickness (μm)	Foil Gap
Inner Tube	13.105	13.857	752	-
LEU Foil	13.8571	13.9821	125	45º
Outer Tube	14.110	15.000	890	-

Use of the VUMAT requires the selection of a 3D brick element. While this plane strain finite element problem could be modeled with much less computational expense using 2D elements, this simply was not an available option in this case. In addition, since the selection of element types is limited to linear brick elements, this eliminated the possibility of using quadratic elements, such as were used by Govindarajan et al. [13]. Quadratic element types use a quadratic shape function to approximate the displacement field whereas linear elements use a linear function. The element type chosen for this work was C3D8RT. These are 8-node, thermally-coupled brick elements with reduced-integration and hourglass control. Thermally-coupled elements were chosen to allow for modeling of the final irradiation step of the process, which is both a mechanical and thermal problem. 10 elements were used through the thickness of each part, and 16,450 elements were used in total.

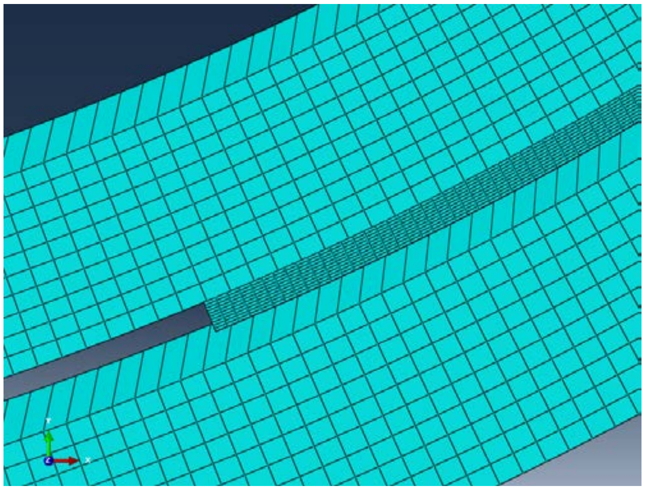

Figure 21. Meshing scheme near the foil relief

Just as with the thick-walled tubes, the coordinate system of the foil was established such that the RD is along the 1-direction, the ND is along the 2-direction, and the TD is along the 3-direction. In terms of tube geometry, the RD, ND, and TD correspond to the axial, radial, and hoop directions. This is critical for the proper application of the VUMAT, so that the material properties are aligned correctly with the right coordinate system. This coordinate system was also applied to the isotropic aluminum tubes for the sake of consistency and also because it is beneficial to visualize stresses in terms of axial, radial, and hoop stresses when dealing with tubes.

Several boundary conditions were applied to ensure a proper solution to the problem. Firstly, a boundary condition for symmetry was applied for symmetry across the vertical axis. This reduced the number of elements which were required to solve the problem, saving computational time. The next boundary conditions applied were zero rotation around the z-axis (θ-rotation), and zero translation at the symmetry boundary. These boundary conditions ensure that after the symmetry condition is applied, the tube components do not drift from the vertical axis as pressure is applied. Lastly, the plane strain condition was enforced by specifying zero displacement in the axial direction. Surface contact interaction properties were set for frictionless, hard contact between each of the components. Thermal interactions between the parts were accounted for by assuming perfect conductance when the parts are in contact and a linear decrease in conductivity down to zero conductivity at a distance of 10 mm.

An initialization step and 3 solver steps were used in this simulation to recreate the hydroforming and irradiation processes. The initialization step serves to establish the boundary conditions and interactions described above, before any loads are applied or calculations are made. In addition, a predefined temperature field of 323 K was set, which will become useful during the irradiation step. The following three steps are all of the dynamic-explicit type, since this is a requirement of the VUMAT. In dynamic analysis, forces and displacements vary with time, and inertial effects are relevant to the solution. Explicit steps determine solutions to problems by explicitly advancing the kinematic state from the previous increment, which requires solving at many small time increments to ensure accuracy. This is in contrast to implicit integrations, which can require multiple iterations within a time step to establish equilibrium and compatibility to within a certain tolerance (at the end of the time step), but can generally solve the problem in fewer steps.

The pressure application step replicates the internal stresses the tube will be subjected to while the irradiation target is assembled during the hydroforming process. An internal pressure of 36.4 MPa was applied to the surface of the inner tube. This pressure was determined experimentally by others to be the maximum pressure which could be bared by the aluminum tubes before rupture occurred along the tube axis in the foil relief region [13]. In the finite element simulation, the load was applied linearly from a pressure of 0 to 36.4 MPa from the beginning to the end of the step. In the pressure removal step, the pressure is linearly unloaded from 36.4 to 0 MPa. At the end of this step, the tubes and foil should still be held together due to the plastic strain accrued in the inner tube, causing it to still be expanded enough to the foil tightly in place. It is important that the foil is in full contact with the tubes in order for the tubes to properly conduct heat to the coolant during the irradiation of the foil.

The irradiation step simulates the temperatures and stresses seen during the irradiation of the LEU foil. The temperatures seen during this process cause thermal expansion of the components which can affect the final stress-state of the assembly. For this step, a body heat flux of 16,000 $\frac{mW}{mm^2}$ was applied linearly to the foil to simulate the heat produced by the irradiation process. Since the assembly is surrounded by coolant during this step, a film coefficient of 19 $\frac{mW}{mm^2K}$ was applied to the inner and outer surfaces of the assembly with a sink temperature of 323 K. This coefficient corresponds to a coolant flow rate of 0.83 $\frac{m}{s}$ through the inner tube and 1.86 $\frac{m}{s}$ along the outside of the outer tube [13]. The main interest in each of these cases is to determine if thermal contact between the LEU foil and Al tubes is maintained, once it is established during the internal pressurization step.

In prior FEA work [13], a contact condition was applied in the first two steps of the problem (pressure application and relaxation) specifying that there should be no separation after contact of two surfaces. This assumption was enforced so that during pressure relaxation, the foil is forced to stay in contact with the surfaces of the inner and outer tubes leading up to the following irradiation step. Physically, the foil should be in full contact with the tubes in this manner so that during irradiation, the aluminum tubes can conduct heat to the surrounding coolant. However, the full closure around the foil should be a result of the proper application of enough internal pressure to cause sufficient plasticity of the aluminum tubes to hold the foil tightly in place. The option to disallow separation after contact therefore should be used with caution, because if the foil would not stay in contact with the tubes without this condition, then the enforcement of this condition may generate inaccurate residual stresses which would not otherwise arise if the foil were allowed to separate normally. In the case of the simulations performed for this thesis, a surface interaction property allowing for separation after contact was employed, since it was deemed logical to check that this pressure level would indeed hold all of the components tightly together following pressure removal.

2.6 Results

Two initial simulations were conducted, one using an isotropic foil with equivalent properties to those employed in the work by Solbrekken et al. [13], and another using an anisotropic/asymmetric foil properties which mimic the VPSC predictions for LEU foil published by Steiner et al. [1]. In addition to the difference in anisotropy, the latter material also exhibits higher strength, in keeping with a literature survey of the mechanical properties of polycrystalline uranium. In the end, this difference in strength will be shown to have very little impact upon the simulation results of the medical isotope target assembly.

For example, it was found that the internal pressure level of 36.4 MPa was not sufficient to fully close the gaps in the assembly after pressure relaxation of both isotropic and anisotropic cases. Though this pressure was understandably chosen because it was determined to be the pressure at which rupture of the aluminum tubes occurs along the foil relief, the present work shows using finite element models using the given properties for the aluminum (Appendix), larger pressures are required to cause enough plastic deformation to close the gaps between the tubes and foil, after unload. Since the foil gap was not uniform across the entire circumference of the assembly, Figure 22 and Figure 23 show examples of where the foil gaps were largest, with the foil gap highlighted by the yellow bars.

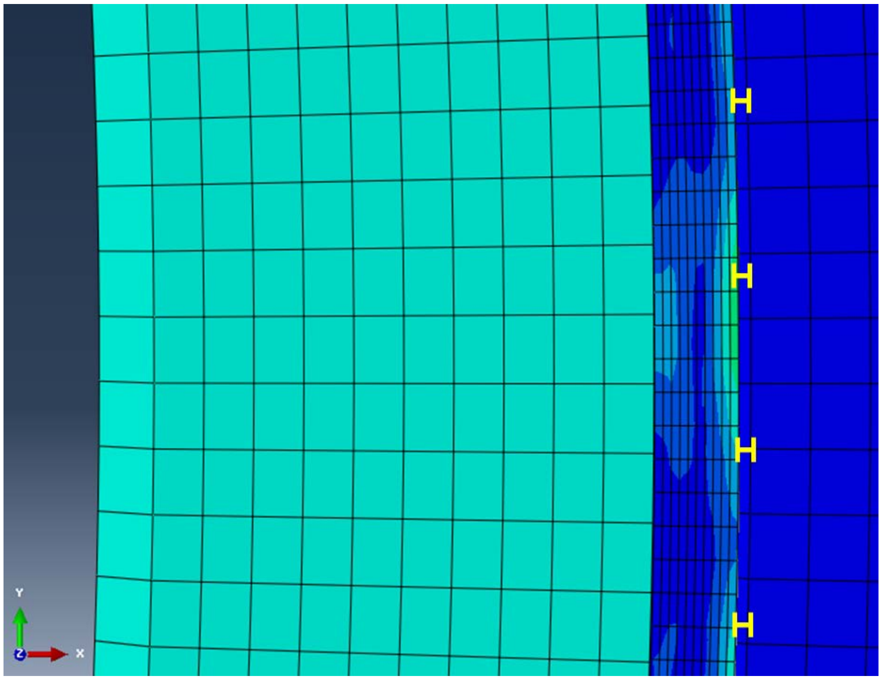

Figure 22. Gap between the foil and outer tube for the isotropic foil

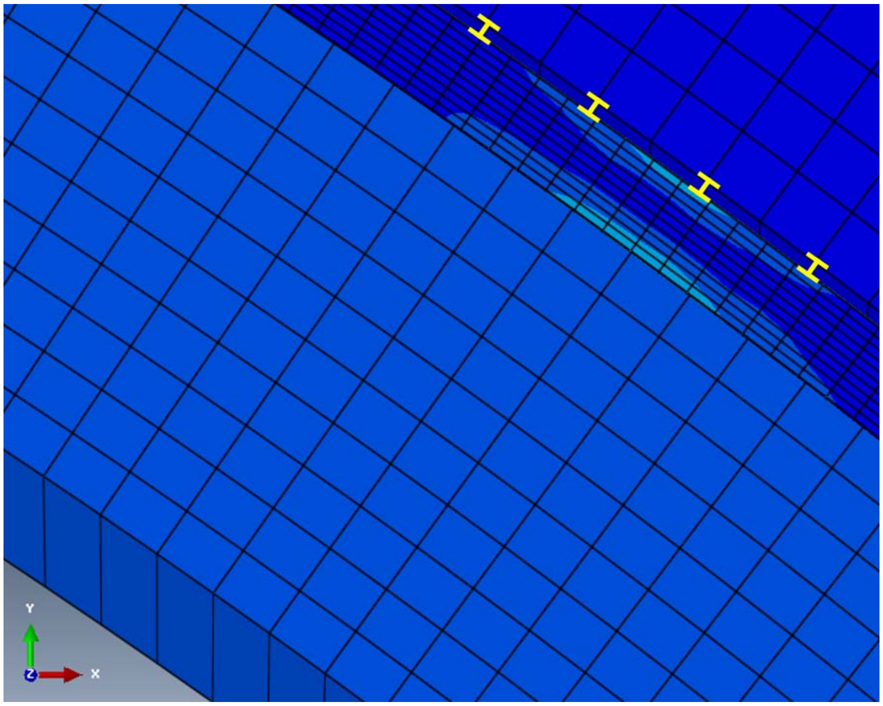

Figure 23. Gap between the foil and outer tube for the anisotropic foil

In order for worthy conclusions to be drawn about the significance of anisotropy in the LEU foil, the pressure must be adjusted to a level which will cause complete closure of the foil within the tubes, even after pressure is relieved. This will ensure that the subsequent irradiation step takes place as it should, with the tubes in full contact with the foil to promote good thermal conductance during irradiation. A series of simulations were performed using a range of internal pressures which caused the assembly to maintain varying levels of contact after pressure relaxation. In the case of 36.4 MPa, the gap was small, so the pressure was increased by 1 MPa per simulated experiment until both foils ended the simulation in full-contact with the tubes. The most important results are summarized in Table 5. Again, since the gaps around the assembly can be uneven, the criterion for the simulation to pass the gap inspection is defined as the foil being in full contact with both tubes for the entire circumference of the foil following pressure relaxation.

Table 5. Summary of closure results for various internal pressures

PRESSURE (MPA)	LEU FOIL TYPE	GAP CLOSED?	LARGEST GAP DISTANCE (μm)
36.4	Isotropic	No	22
	Anisotropic	No	19
39	Isotropic	No	16
	Anisotropic	No	13
40	Isotropic	No	4
	Anisotropic	No	10
41	Isotropic	Yes	0
	Anisotropic	Yes	0

The pressure required to fully close the gap following pressure relaxation when using both the isotropic and the anisotropic foil is roughly 41 MPa. The pressure required to close the gap is the same for both foils (within 1 MPa), so further analysis into the details of the simulation results will have to be done to observe any differences anisotropy may have caused in the stresses seen in the hydroforming and irradiation processes. Figure 24 shows a visual comparison of the Mises stresses seen in the whole assembly at full pressure, which are at first glance very similar.

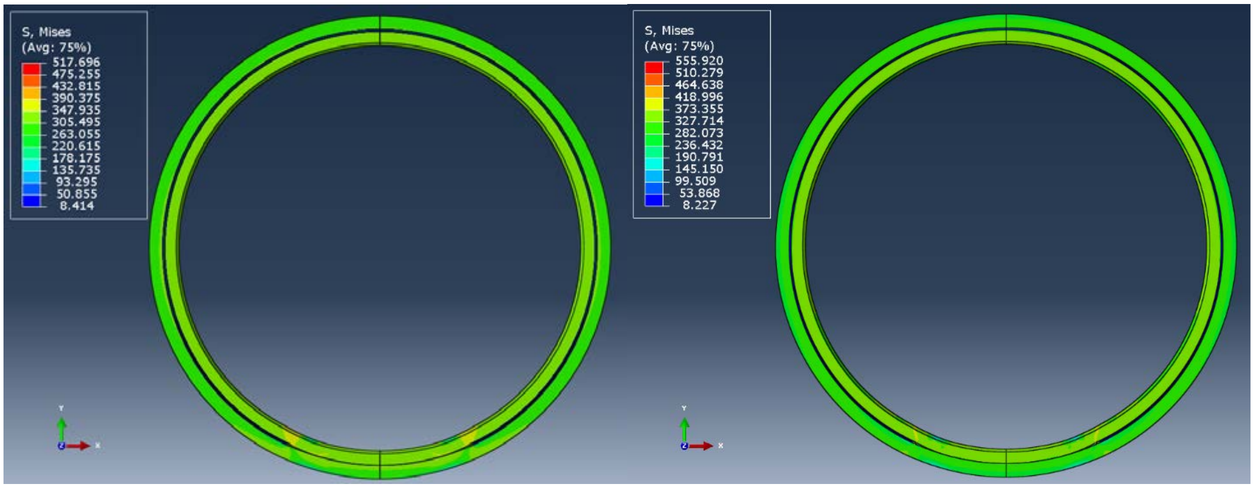

Figure 24. Mises stresses in irradiation target at full pressure (41 MPa), for isotropic (left) and anisotropic (right) LEU foil.

The 41 MPa of applied pressure is accompanied by plasticity in the inner aluminum tube, especially near the ends of the foil. This plasticity is what causes the inner tube to stay expanded following hydroforming, thus creating closure through the assembly for good contact during irradiation. During the internal pressurization step, a maximum equivalent plastic strain value of 0.093 is reached in the anisotropic foil case, which develops to 0.105 at the beginning of the pressure removal step (Figure 25). For the case of the isotropic foil, the maximum plasticity values for the pressure and relaxation steps are 0.100 and 0.104 respectively. The range of plasticity in the tubes then remains constant through the remainder of the simulation. Isolation of the outer tube in the visual analysis (Figure 26) revealed that a small amount of localized plasticity occurred in the outer tube near the foil end, but essentially zero plasticity is found at every other position on the outer tube. This is true for both foil types.

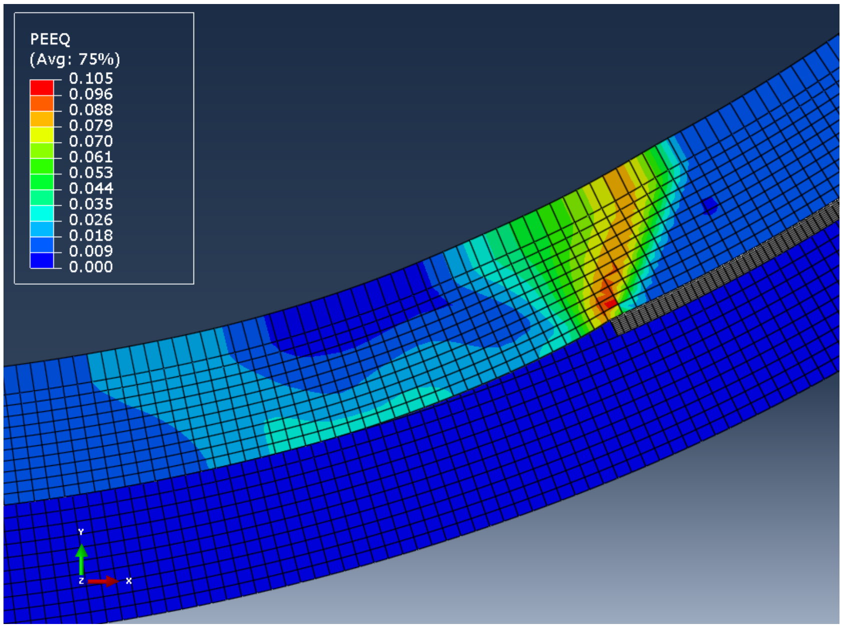

Figure 25. Plastic strain observed following assembly and irradiation of the anisotropic foil

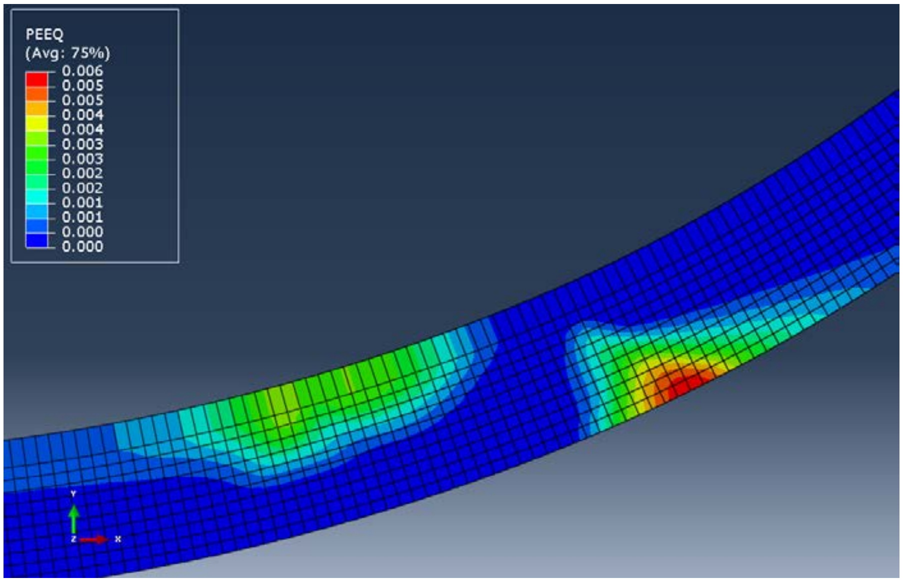

Figure 26. Localized strain in the outer tube

No gaps were found to form during any of the steps for both foils, which is significant because it proves that at this pressure level, the uranium foil will be held in place during the entire procedure so that the aluminum tubes can conduct heat away during the irradiation process, regardless of whether the foil anisotropy is taken into account or not. At full pressure, a very high, localized stresses can be seen at the end of the foil, but the rest of the foil has relatively low stress compared to the aluminum tubes (Figure 27). After the pressure is relieved, mild residual stresses are left in the inner tube and at the end of the foil, but the stresses through the majority of the foil and outer tube are relatively low (Figure 28). During irradiation, the uranium foil expands due to heating, and, being further compressed by the aluminum tubes, sees higher stresses than in the previous steps (Figure 29). In reality, these stresses are expected to relax over time as the assembly is held at this temperature, so the key result here is that contact is maintained even under thermoelastic loading indicative of the irradiation step. These results are at least capable of demonstrating that the higher temperatures seen in the uranium will cause the foil to expand more than the aluminum, and the foil will remain in place between the tubes during irradiation.

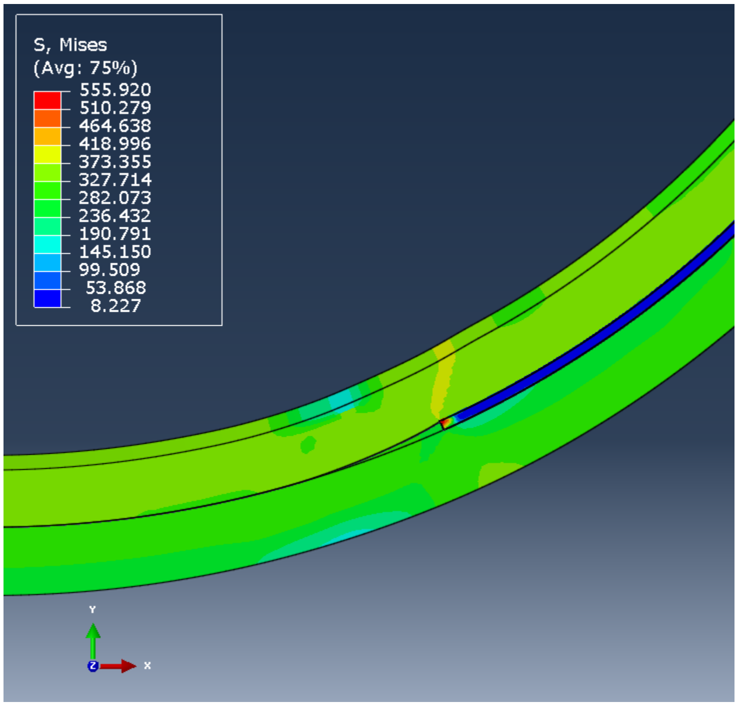

Figure 27. Mises stress in anisotropic assembly at full pressure (41 MPa)

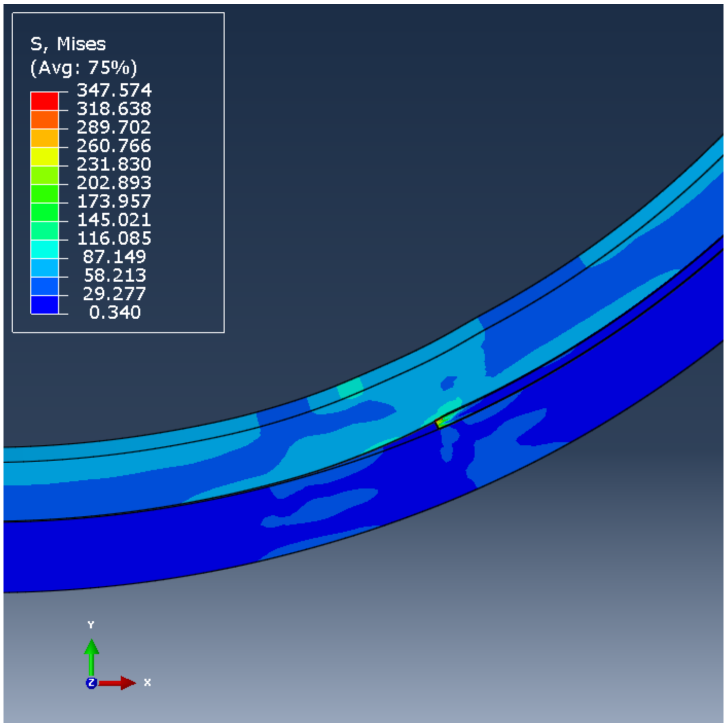

Figure 28. Mises stress in anisotropic assembly at zero pressure

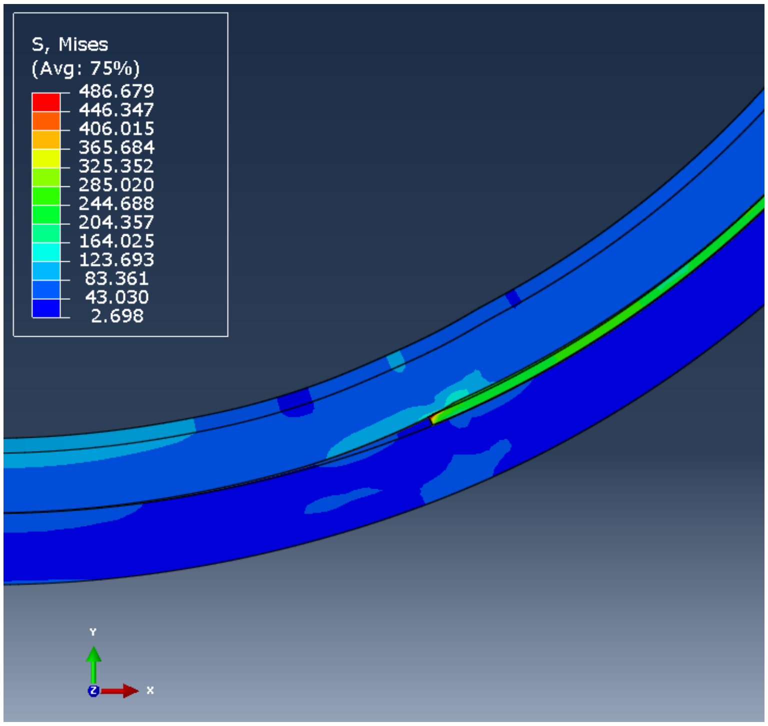

Figure 29. Mises stress in anisotropic assembly during irradiation

Now that the general stresses and strains seen in the assembly are understood, a closer look will be taken to determine if the anisotropy of the foil can significantly affect any of the stress-states in the assembly. The most significant simulation steps to consider are the hydroforming steps, since these steps will test if anisotropy affects the mechanical performance of the foil. In Figure 30 and Figure 31, the hoop and radial stresses seen at the top of the target assembly, as pictured in Figure 24, chosen since it is furthest from the localized effects of the foil end, were plotted through the thickness for the hydroforming steps.

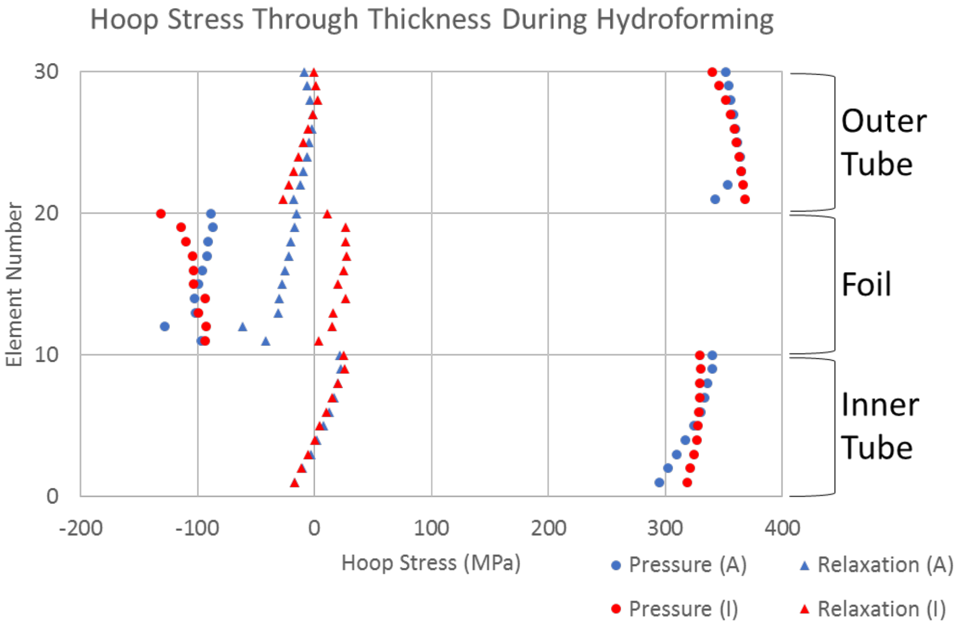

Figure 30. Hoop stresses throughout the tube assembly during hydroforming

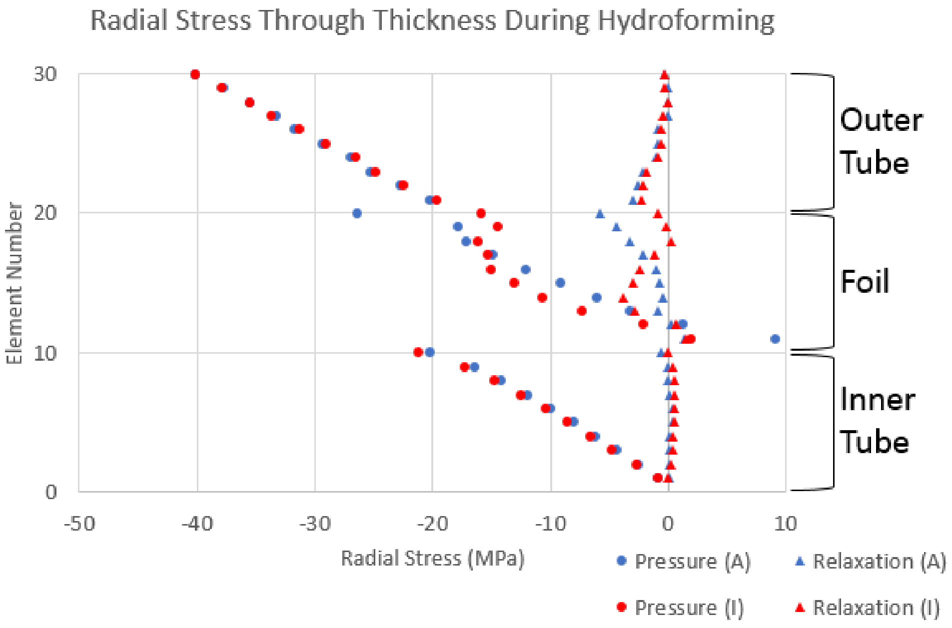

Figure 31. Radial stresses throughout the tube assembly during hydroforming

The results for the stresses observed through multiple components of the assembly are similar for both foil types. At full pressure, the hoop stresses seen in the tubes are tensile, whereas the radial stresses in both foils are compressive. A slight difference exists in the nature of the stresses seen in the foil after pressure is removed. The anisotropic foil remains in a mildly (10s of MPa) compressive state, while the isotropic foil has mildly positive hoop stresses. Overall, there are no other dramatic differences in the stress-sates of the assembly.

Another metric for comparison is the amount of plastic strain (PEEQ) accumulated in the inner tube, since very little plasticity was observed in the outer tube. If there is a difference in the strength of the foils, then there may be different levels of deformation in this component. However, it was found that very similar amounts of PEEQ were measured in both the isotropic and anisotropic cases, as can be seen by the overlapping plots in Figure 32. A comparison of the PEEQ seen at the inner and outer radius of the anisotropic case is shown in Figure 33 to demonstrate that slightly higher plasticity is seen near the inner radius. Only the anisotropic case is shown in Figure 33 because the isotropic results nearly overlap these lines as well.

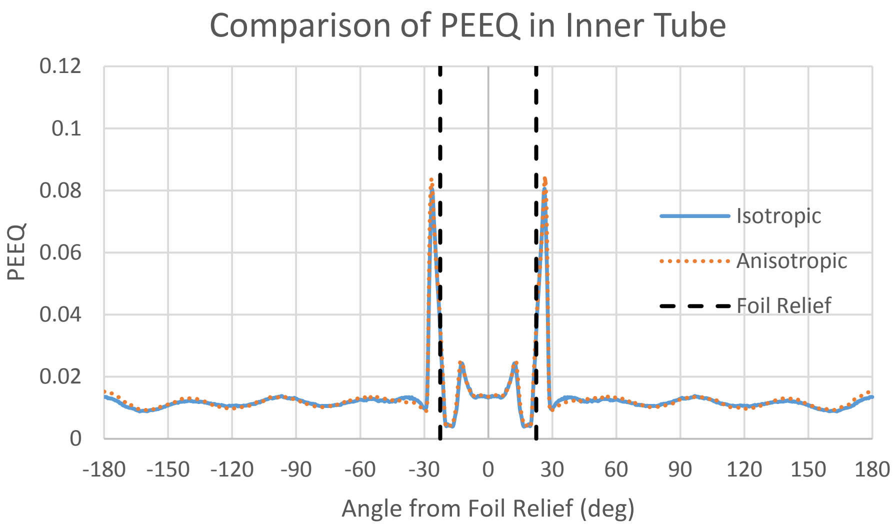

Figure 32. Comparison of PEEQ in inner tube between isotropic and anisotropic foil cases

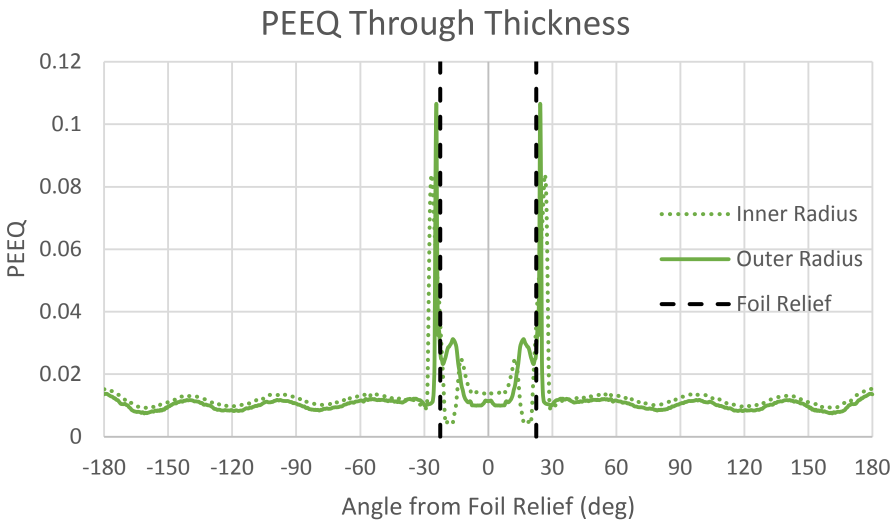

Figure 33. Comparison of PEEQ between inner and outer radius of inner tube

Finally, a critical aspect of this analysis is the determination of the final stress-state in the outer tube. The tensile or compressive nature of the hoop stress in the outer tube will determine how difficult it is to retrieve the fission products at the end of irradiation. As stated previously, if the hoop stress is tensile in nature, the outer tube will spring open when cut, aiding in retrieval of the foil. If the outer tube is in compression in the hoop direction, the tube will collapse when cut, making retrieval of the fission products a more difficult and lengthy process. The average hoop stress through the thickness of the outer tube was plotted for each radial position around the target assembly (Figure 34). The results show that the hoop stress for the outer tube is higher in most of the foil relief section for the isotropic foil, but lower for the rest of the assembly. On average, the hoop stresses for the isotropic case are lower than for the anisotropic case, but the hoop stress in both assemblies is within 3 MPa of the other. Thus, there is ultimately no significant difference in the resulting stress-state. For both cases, the residual hoop stress after hydroforming is positive around the entire assembly, indicating that it would spring open if cut. However, during irradiation, it is expected that these stresses will relax and may ultimately be of little aid in the retrieval of the foil. The important point here is that failure to account for the anisotropy in the uranium foil does not appear to have compromised the conclusion of the prior study [13], in which it was stated that residual stresses of manufacturing will not impede retrieval of fission products after irradiation of this new irradiation target design.

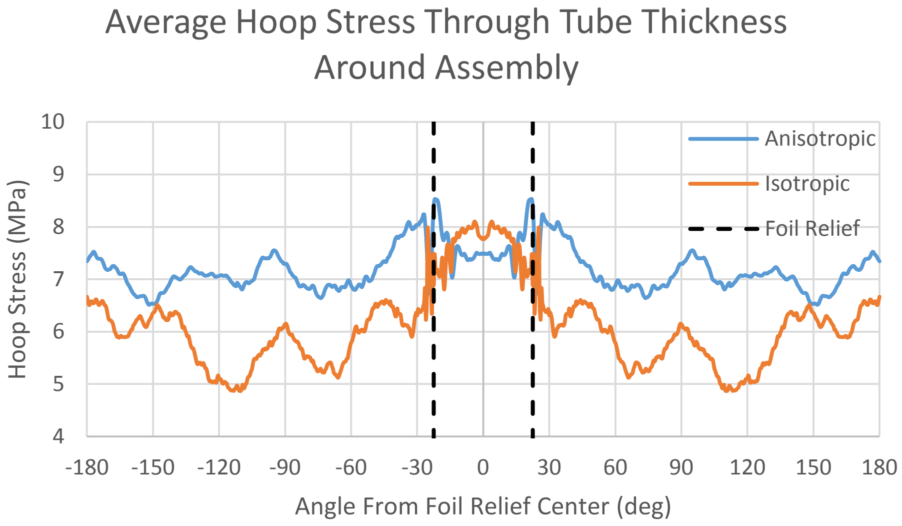

Figure 34. Residual hoop stresses around the outer tube

2.7 Conclusions

The CPB06 and hardening parameters were successfully fit to the predictions of the VPSC polycrystal plasticity model of a LEU straight-rolled foil. The employment of the CPB06 VUMAT with these material parameters showed that the material behaved as expected in finite element simulations of single elements under uniaxial loading and internal pressurization of thick-walled tubes. Although anisotropy can have a significant impact upon the stress state of such thick-walled tubes, when the foil-type anisotropy was used, the stress state was found to be similar to that of isotropic uranium. It appears the higher compressive strength along the ND (tube radial direction) and lower tensile strength along the TD (tube hoop direction) have counteracted one another in this application.

In agreement with this finding, the anisotropy did not have a significant effect on the results of the hydroforming and irradiation simulations for the Tc-99 target. The fact that the anisotropy effects are minimal for the internally-pressurized loading condition is likely due to the thin geometry of the uranium foil in comparison to the much thicker aluminum tubes which surround the foil. In parts of the assembly where the foil is present, the foil accounts for ~7% of the thickness of the total assembly. A greater increase in the strength of the foil would be required before significant differences in the performance of the irradiation target are observed.

Though the resistance of the foils to internal pressurization was ultimately considered to be similar, success in the finite element simulations was achieved in finding the pressure level required to create full contact between the tubes and foil after pressure is removed. The value of 41 MPa is higher than the 36.4 MPa previously explored [13]. This explanation for the distinct conclusion of the two studies is attributed to the removal of the contact condition requiring contact to be maintained between parts which have come into contact during the pressure and relaxation steps. This could be significant, since the design of the irradiation target may have to be reconsidered to handle higher pressures without rupturing the tubes during the assembly hydroforming step.

Some minor points of success are that at this pressure level, the tensile hoop stresses seen throughout the assembly are expected to aid in the retrieval of the fission products. Additionally, during the peak steady-state temperatures seen in irradiation, a gap did not form between any of the components due to thermal expansion. This shows that, at this pressure level, the current FEA model of the medical isotope target (which accounts for the expected plastic anisotropy of the foil) predicts that the hydroforming and irradiation of the LEU foil will be successful, assuming none of the aluminum tubes do fracture during target assembly. A strategy to mitigate the concern regarding tube rupture is outlined in the future work section.

3. Phase Transformations in U-10 wt% Mo with Ternary Additions of Cr, Ni, and Co

3.1 Introduction to Phase Transformations in U-Mo Alloys

The BCC γ-U phase is ideal for use as a nuclear fuel due to its favorable burnup characteristics when irradiated compared to the orthorhombic α-U phase [15]. Left unalloyed, the high-temperature BCC phase will return to α-U at temperatures below the eutectoid (560 ºC). The γ-U phase can be retained as a metastable phase at room temperature by the addition of an alloying element, which will slow the rate of the phase decomposition reaction. U-Mo alloys have been shown to have a good balance of high uranium density and γ-phase stability [16]. In addition, molybdenum has a relatively low neutron absorption cross-section compared to many other elements used as γ-stabilizers, which is preferable for maintaining fuel efficiency during irradiation. The choice of 10 wt% Mo is based on compromises between factors such as uranium density, phase stability, and other material properties. The ductility and fracture toughness of U-10Mo is better than U-12Mo [4], and it is less susceptible to stress-corrosion cracking than U-7Mo [30], making U-10Mo a good choice for a high-performance reactor fuel.

The phase diagram for U-Mo (Figure 35) shows that below ~560 ºC, the γ-U-Mo phase will transform to α-U and γ’ (U_2Mo). The yellow arrow indicates the location of the U-10 wt% Mo system, which is 21.6 at%.

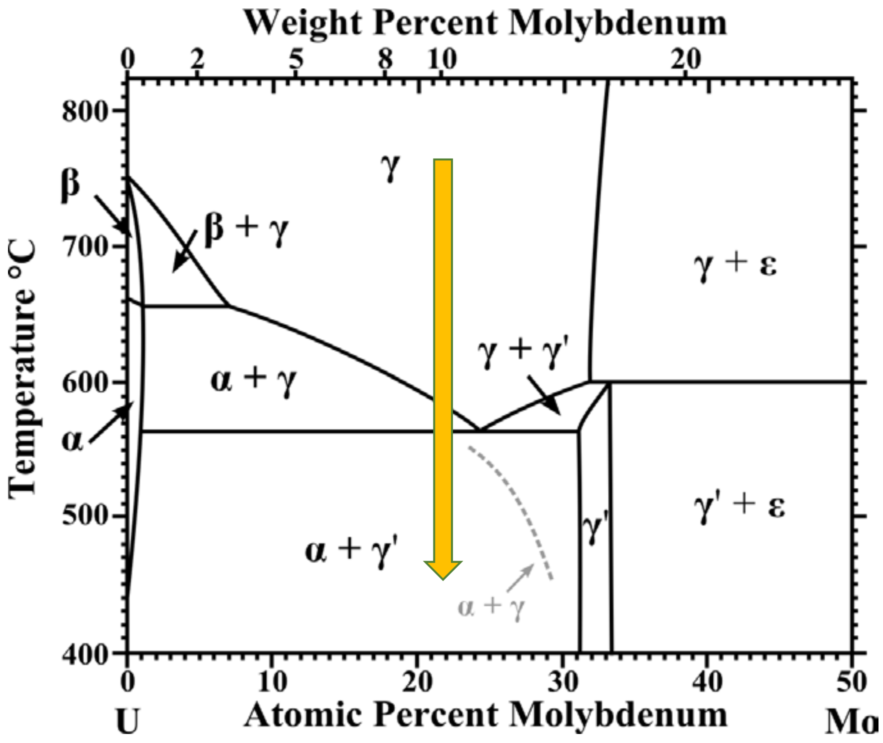

Figure 35. Phase diagram for U-Mo with 10 wt% Mo position highlighted [31]

The orthorhombic α-U phase and tetragonal γ’ phases are anisotropic, and display unfavorable burnup characteristics during irradiation, including cavitation swelling and thermal growth [15]. These phases are formed below the eutectoid temperature by a eutectoid transformation, which occurs by discontinuous precipitation [3]. Development of secondary phases in U-Mo begins with the precipitation of a lamellar microstructure consisting of α-U and Mo-rich γ-U-Mo which forms along the former γ-U-Mo grain boundaries [31, 32]. The timeline of the phase decomposition reaction can be visualized using a time-temperature-transformation (TTT) diagram (Figure 36).

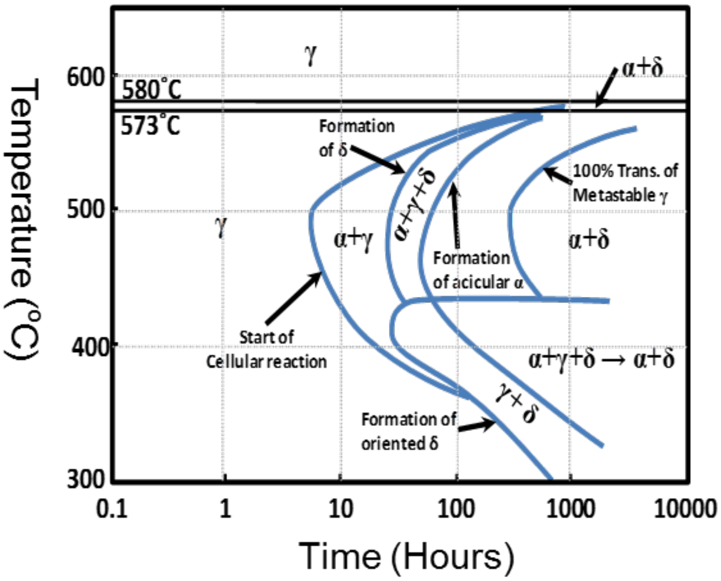

Figure 36. TTT diagram for U-10Mo [33]

The TTT diagram shows that the earliest onset of precipitation will occur close to 500 ºC, therefore this will be the target temperature for the experiments performed in this thesis. In these experiments, Cr, Ni, and Co will be added in small fractions (0.2 wt%) as ternary alloying elements to the U-Mo system while maintaining 10 wt% total alloying additions to the uranium. The addition of these elements may increase or decrease the time needed to start precipitating secondary phases, as well as the rate of growth, depending on how these elements interact with the primary matrix material.

These elements were chosen since they are common potential metal contaminants in U-Mo fuels. Since the contaminant level is theoretically low, this is why these alloys were added in small 0.2 wt% amounts. Cr (BCC), Ni (FCC), and Co (HCP), each having a different unit cell structure, may exhibit different levels of solubility in the BCC U-Mo matrix, yet another reason these elements were chosen.

3.2 Introduction to Neutron Diffraction and Rietveld Analysis

Neutron diffraction is an experimental technique which uses the elastic scattering of neutrons to determine the atomic structure of a material. This technique is similar to x-ray diffraction, but offers several unique advantages. Since neutrons interact with atomic nuclei, which are small in volume compared to the electron cloud, neutrons have a much higher penetration depth than x-rays. Due to this increased penetration depth, neutrons can be used to analyze bulk materials very effectively. Additionally, neutrons are more effective than x-rays in interacting with light atoms, which do not have large electron clouds, and are also useful in determining magnetic ordering [34].

Neutron scattering operates on the same basic principle as x-ray diffraction. As waves are scattered from lattice planes in a material, they interfere either constructively or destructively. The condition for constructive interference is outlined by Bragg's Law.

$$n\lambda = 2d \cdot sin\theta \qquad \text{(Eq. 29)}$$

In this equation, λ is the wavelength of the constructively interfering waves, d is the spacing between the planes, θ is the scattering angle, and n is an integer. This equation determines the total path difference, $(2d \cdot sin\theta)$, between two waves undergoing constructive interference. This path difference is demonstrated in Figure 37.

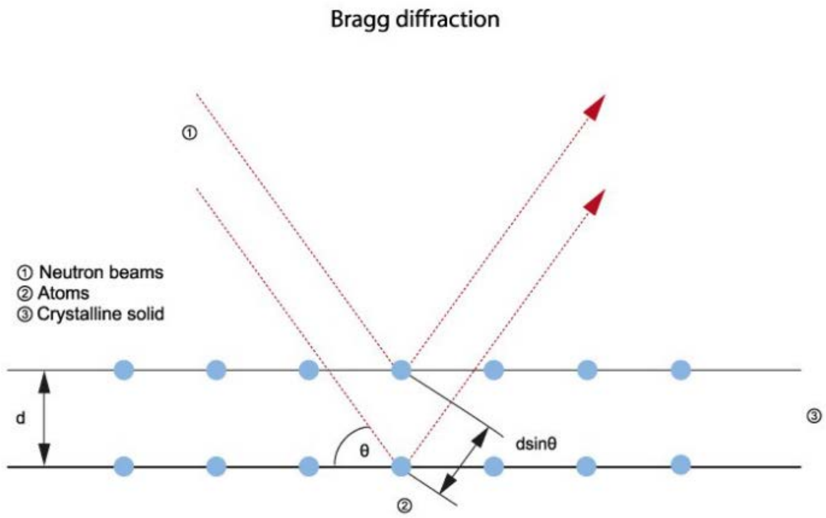

Figure 37. Constructive interference of neutrons [34]

Constructively interfering waves reach the detector at the end of the instrument, where the intensity of these waves is measured. The intensity is then plotted as a function of the scattering angle, d-spacing, or time-of-flight (TOF), resulting in a wave-interference pattern, commonly called a diffraction pattern. The experiments in this thesis were conducted on instruments using neutrons produced by a spallation neutron source, and thus use the TOF method, which is a method for measuring the d-spacing neutrons traveled through based on the time it takes for the neutron to travel from the chopper to the detector. The TOF concept will now be explained briefly.

The wavelength of a neutron can be related to its momentum by using the de Broglie equation (Eq. 30), where *h* is Planck's constant and *m* is the mass of a neutron. The wavelength of a neutron is therefore inversely related to its velocity.

$$\lambda = \frac{h}{mv} \qquad \text{(Eq. 30)}$$

Neutrons travel on the order of a few meters per millisecond, so their velocity can be easily measured using modern sensors [35]. The distance from the chopper to the detector, L, is known, and the velocity of a neutron can be expressed as $\frac{L}{t}$. Using this, the TOF equation can be constructed (Eq. 31). Again, this equation is useful for relating the wavelengths or velocities of neutrons to the d-spacings they traveled through.

$$\lambda = \frac{ht}{mL} = 2d \cdot sin\theta \qquad \text{(Eq. 31)}$$

Two neutron diffraction instruments were used in this study. The Spectrometer for Materials Research at Temperature and Stress (SMARTS) resides at the Lujan Center at Los Alamos National Laboratory, and is used for neutron diffraction with a focus on studying polycrystalline materials under stress, deformation, and temperature [36]. This instrument was chosen for its vacuum furnace capability, so the phase transformation kinetics of U-Mo samples could be monitored at temperature. Another Lujan Center instrument used was the High-Pressure-Preferred Orientation (HIPPO) instrument [37]. This powerful instrument specializes in studying texture by delivering high neutron count rates coupled with a large detector area. Data collected on this instrument was used to study the preferred orientation of phases in the cast U-10Mo samples.

Neutron diffraction patterns can reveal useful information about a material, but the information must be extracted from the diffraction data using a method known as Rietveld analysis. This type of analysis can be used to determine information about phases in the material such as weight fraction, lattice parameter, texture, microstrain, and more. A primary advantage of Rietveld analysis is that it works for diffraction patterns with overlapping peaks, such as material systems with multiple phases. Equation 32 - Equation 36, outlining the mathematics behind Rietveld refinement are from A. Garg [38].

The experimental intensity of peaks seen in diffraction patterns is given by Equation 32.

$$I_k = m_k L_k |F_k|^2 P_k A_k \qquad \text{(Eq. 32)}$$

In this equation, the intensity of the k^{th} reflection is determined by the multiplicity, m, Lorentz-polarization factor, L, structure factor, F_k , preferred orientation factor, P, and absorption factor, A. In Rietveld analysis, a software-generated diffraction pattern is calculated based on Equation 33.

$$I_i^{calc} = S_F \sum_{j=1}^{Nphases} \frac{f_j}{V_j^2} \sum_{k=1}^{Mpeaks} L_k \left|F_{k,j}\right|^2 S_j\left(2\theta_i - 2\theta_{k,j}\right) P_{k,j} A_j + bkg_i \qquad \text{(Eq. 33)}$$

This equation includes information about the beam intensity, S_F, phase volume fraction, f, cell volume, V, Lorentz-Polarization factor, L, structure factor, F, preferred orientation $P_{k,j}$, and volume absorption, A. A Rietveld analysis software will use an optimization routine to vary the values of select parameters which influence the calculated beam intensity until a good-fit between the experimental and calculated diffraction patterns is achieved. The amount of error between the experimental and calculated patterns, which the software seeks to minimize, is determined using Equation 34, where y_i is the observed or calculated intensity at a particular TOF or d-spacing.

$$Error = \sum_i \frac{(y_i^{obs} - y_i^{calc})^2}{y_i^{obs}} \qquad \text{(Eq. 34)}$$

Equation 35 demonstrates a standard measure of the goodness of fit, the "R" value of a weighted pattern, R_{wp}.

$$R_{wp} = \sqrt{\frac{\sum w_i (y_i^{obs} - y_i^{calc})^2}{\sum w_i (y_i^{obs})^2}} \qquad \text{(Eq. 35)}$$

where

$$w_i = \frac{1}{y_i^{obs}} \qquad \text{(Eq. 36)}$$

In the neutron diffraction experiments conducted on the U-10Mo system with ternary alloying elements, Rietveld analysis will be employed heavily for phase fraction analysis, lattice parameter determination, and texture analysis.

3.3 Experimental Methods

3.3.1 Materials

Materials for this experiment were manufactured at PNNL and transported to LANL for experimentation. 12 samples of 4 different compositions were used (3 samples per composition). The control group contained 3 samples with a composition by weight percent of U-10Mo. The other 3 groups contained 3 samples each of U-9.8Mo-0.2Cr, U-9.8Mo-0.2Ni, and U-9.8Mo-0.2Co. Each sample began as U-9.2Mo, and 0.6 wt% Mo and 0.2 wt% of a ternary alloy were added. First, they were melted and arc-cast in a water-cooled copper hearth under cover of argon gas to minimize oxidation. Each sample, containing the appropriate amount of each element by weight percent, was then heated to 900 ºC under argon gas to homogenize the material. This step is critical because it both increases the homogeneity of the alloy distribution in the material and also brings the material well into the γ-phase field of the phase diagram so that the material is fully converted to the BCC γ-phase in case any other phases had formed during casting. After this heating step, the material was cooled using furnace cooling at an average rate of ~2-3 degrees Celsius. Figure 38 shows the heating and cooling plan these samples experienced.

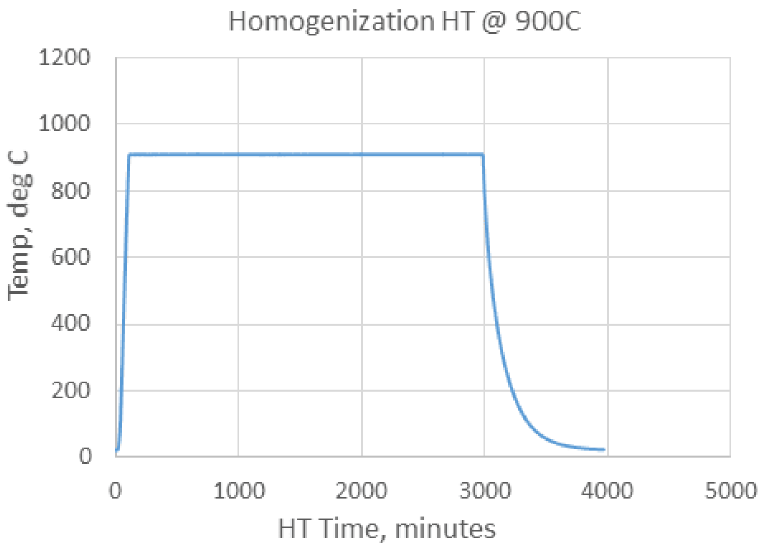

Figure 38. High-temperature homogenization and cooling [39]

The cool from 900 ºC was plotted over a TTT diagram of the U-10Mo system in Figure 39 to verify that no secondary phases were formed during the cooling step. If cooling is performed too slowly, secondary phases could develop, which defeats the purpose of attempting to preserve the high-temperature phase.

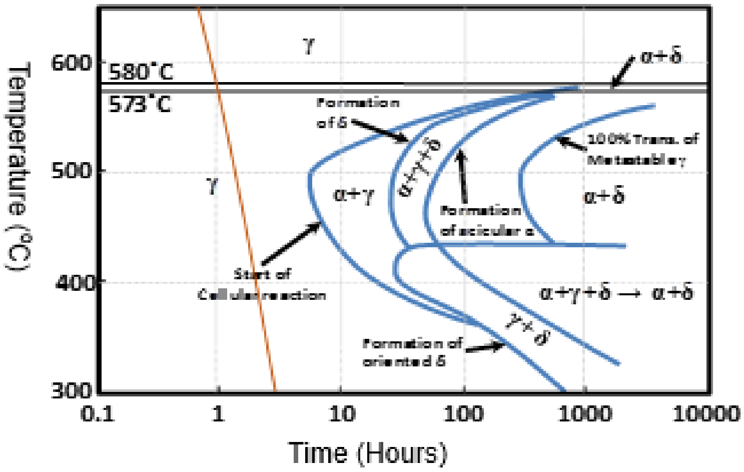

Figure 39. TTT diagram for U-10Mo

While ideally this would be plotted over a continuous cooling curve, a CCT diagram is not currently available for this material system. This TTT diagram can be used to approximate that no phases should have formed during the cooling step.

3.3.2 SMARTS Experiments

The 12 samples were sent to Los Alamos National Laboratory for experimentation on the SMARTS neutron diffraction instrument. The goal of these experiments was to collect *in situ* neutron diffraction data for the U-Mo samples held at temperature for 20 hours to track the phase kinetics. In order to make the most of allotted beam time on the instrument, two samples were placed in the furnace at a time, which was made possible by the use of a sample exchanger arm which moved back and forth to alternate which sample was in the beam path over the course of the experiment. The arrangement of the samples in the furnace is shown in Figure 40.

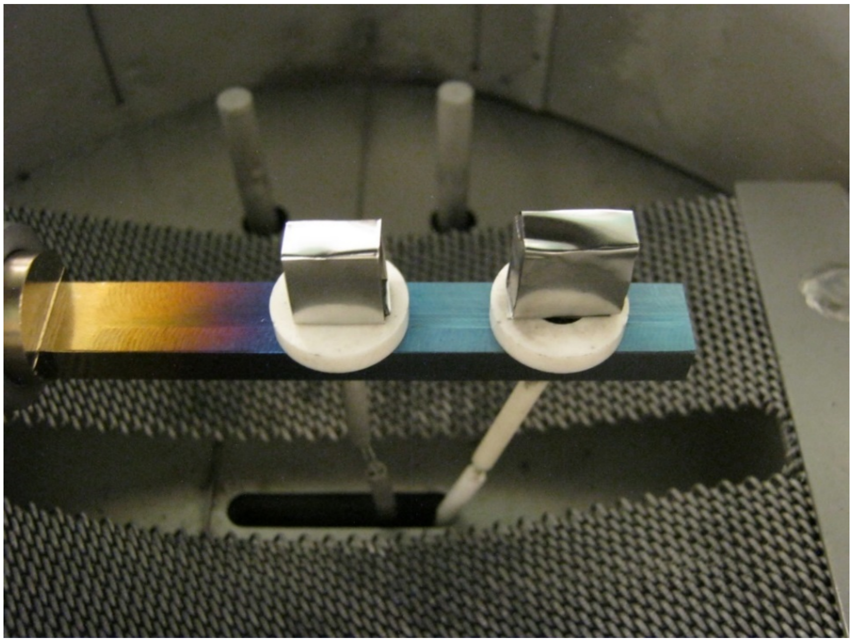

Figure 40. Arrangement of samples inside the SMARTS furnace

The two samples were placed on the steel sample holder with alumina washers separating the samples from the steel bar to minimize any cooling effects from contact with the steel. The steel sample exchanger is in contact externally with water coolant, so alumina washers were needed to make sure the influence of this coolant on the sample temperature was minimized. These samples were in direct contact with two thermocouples which came in direct contact with the samples through holes in the bottom of the sample holder bar. These samples were also wrapped in niobium foil which were used as another method to read the temperature by measuring the thermal expansion with neutron diffraction and comparing that to a known temperature-strain correspondence. Niobium was chosen because it has a known strain-temperature relationship and would not become significantly radioactive during the neutron experiment.

The position of each sample was calibrated so that no other materials, such as the alumina washers or equipment in the furnace, were visible in the neutron beam. Once positioned, the furnace was closed and a vacuum was created so that the U-Mo was not being heated in an oxidizing environment. Following vacuum pull, a neutron diffraction pattern was collected at room temperature so that an initial diffraction pattern could be collected from the samples before they underwent aging.

At this point, the temperature of the furnace was ramped to 650 ºC at the maximum heating rate of 50 degrees per minute. This temperature was chosen since it is high enough above the γ-solvus to transform any secondary phase particles back to the primary phase and homogenize any portions of the material which were not already homogenized. The samples remained at this temperature for 1 hour to solutionize the material once again, but also to calibrate the thermocouples for the successive drop to the determined temperature. The selected temperatures were 490 and 500 ºC, which are near the nose of the TTT diagram, where the earliest onset of phase decomposition occurs. These temperatures were chosen so that the maximum amount of phase transformation could be observed in the shortest amount of time due to limited time on the instrument, but also so that hopefully the precision of the position of the nose of the TTT diagram described in the collective scientific literature could be further established for U-10Mo.

After heating for one hour, the furnace was cooled at the maximum rate of 50 degrees per minute to either 490 or 500 ºC. While quenching to room temperature and then heating the sample would more accurately reproduce the conditions experienced by U-Mo fuel in service at a reactor, the quench rate would have a significant impact on the rate of phase transformation. Therefore, the samples were instead cooled immediately to the target temperature, eliminating the complexity of phase transformation kinetics due to a prior quench. The samples were held at the target temperature for a minimum time of 20 hours to collect neutron diffraction data which would later be analyzed using Rietveld analysis for phase transformation information. Figure 41 shows the temperature profile of the furnace and samples over the course of the first experiment. The temperature profile for the next two experiments was very similar.

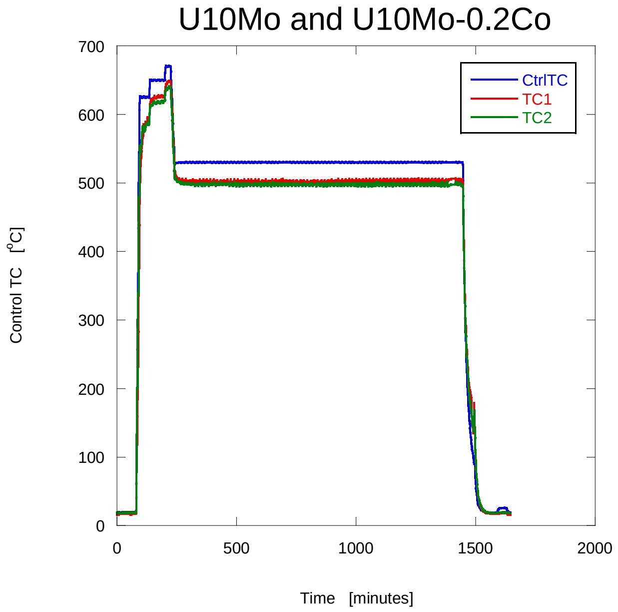

Figure 41. Sample heat profile for U-Mo diffraction experiment

The step increases in temperature seen near the beginning were due to attempts to establish the approximate difference in the temperature read between the control thermocouple, which measured the temperature of the furnace near the outer wall, the thermocouples placed directly under each of the samples, and the niobium foils. The calibration of this temperature difference was critical to be able to cool precisely to the target temperature without over or undershooting.

During the isothermal hold, each sample was held in the neutron beam for ~6 minutes at a time before the sample changer moved with a motor to place the other sample in the beam. It is important to note that each sample experienced ~1 degree change in temperature as the sample arm moved closer or further from the center of the furnace, likely due to the samples getting closer or further away from the water-coolant in contact with the outside of the sample changer. However, this is not expected to have a significant effect on the phase kinetics.

During this time, continuous TOF diffraction data was gathered and stored in files which were later be read by the GSAS Rietveld analysis software. After 20 hours, the samples were cooled at the maximum rate to room temperature and pulled from the furnace. Table 6 shows a summary of the experiments that were performed on the 6 samples which were able to undergo experimentation. The second experiment went over the required 20 hour time due to the experiment running overnight, allowing the experimentalists to sleep.

Table 6. Summary of SMARTS Experiments

Samples	Isothermal Hold Temperature	Isothermal Hold Time
U-10Mo U-9.8Mo-0.2Co	500 ºC	19.90 hrs
U-9.8Mo-0.2Cr U-9.8Mo-0.2Ni	500 ºC	30.43 hrs
U-9.8Mo-0.2Cr U-10Mo	490 ºC	19.75 hrs

Following the experiments performed at high temperature, an *ex situ* room temperature scan of each of the original 12 samples was done on the SMARTS instrument so that the final phase compositions of all of the samples could be determined for the planning of future experiments.

3.3.3 HIPPO Experiments

The HIPPO instrument was used to analyze phase content and texture in each of the 12 samples. Following the experiments on SMARTS, *ex situ* diffraction patterns were collected at room temperature with HIPPO at 0º, 67.5º, and 90º Ω-offsets. Data was collected in 5 banks at detector positions of 40º, 60º, 90º, 120º, and 150º. These Ω-offsets and collection angles are the standard for collecting texture data on the HIPPO instrument [40]. The large area of coverage allows for quality information about the texture to be revealed using the E-WIMV texture analysis function in the Materials Analysis Using Diffraction (MAUD) Rietveld analysis software, where the orientation distribution function (ODF) is refined during a texture analysis.

3.4 Results

3.4.1 Initial Observations

A section of the final diffraction patterns of the samples exposed to isothermal holds is shown in Figure 42-Figure 45. One of each sample type is shown because results for repeat sample types are very similar. For these images, a close-up of the highest d-spacing peak group is shown, since this group of peaks is the most intense and offers the clearest visual of the phases present.

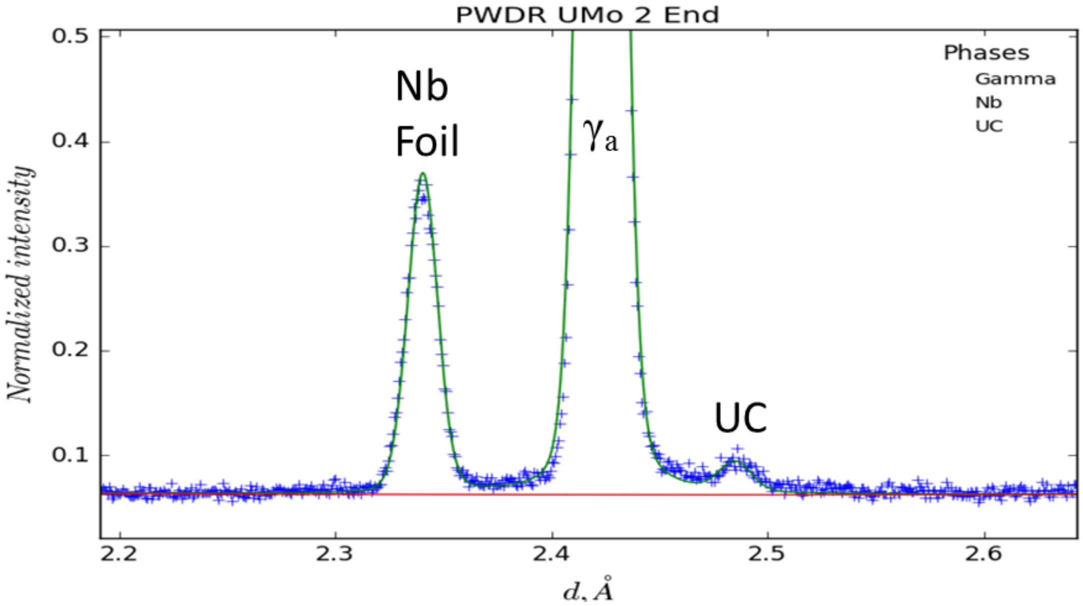

Figure 42. Diffraction pattern section for U-10Mo after aging

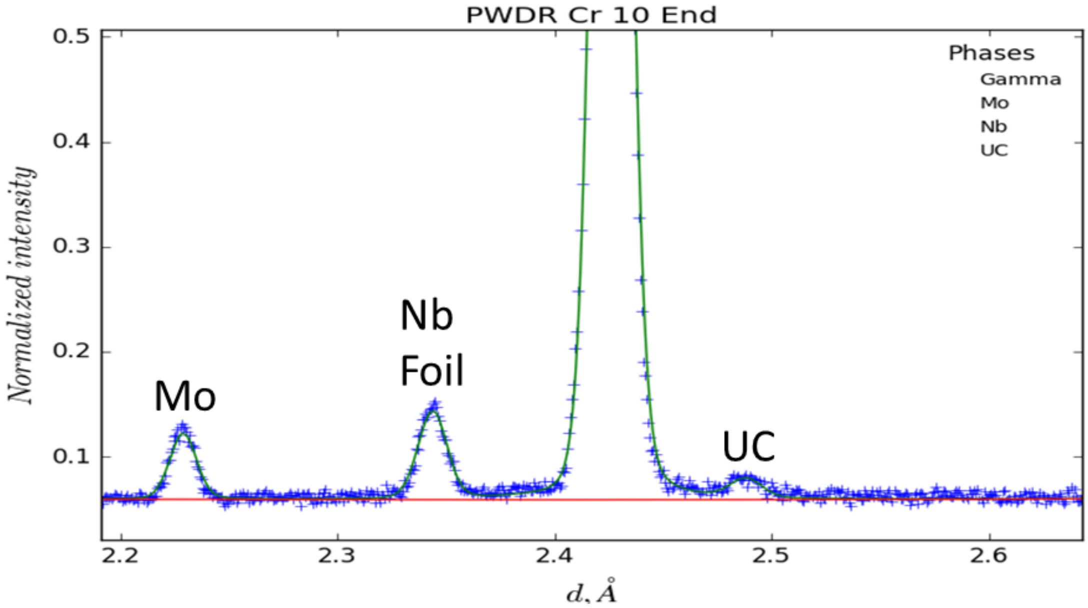

Figure 43. Diffraction pattern section for U-9.8Mo-0.2Cr after aging

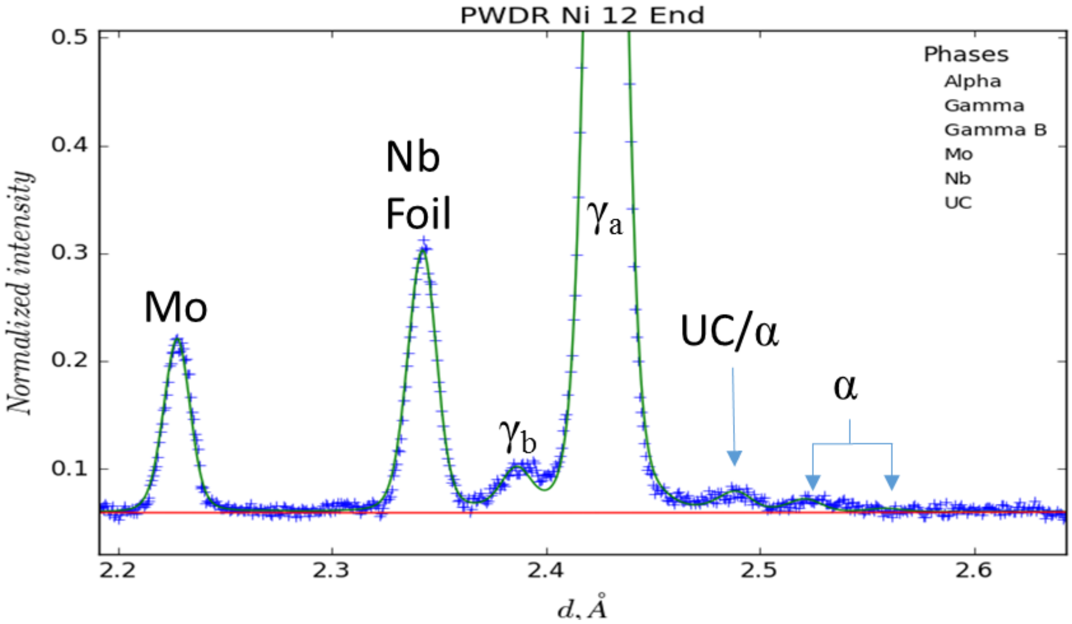

Figure 44. Diffraction pattern section for U-9.8Mo-0.2Ni after aging

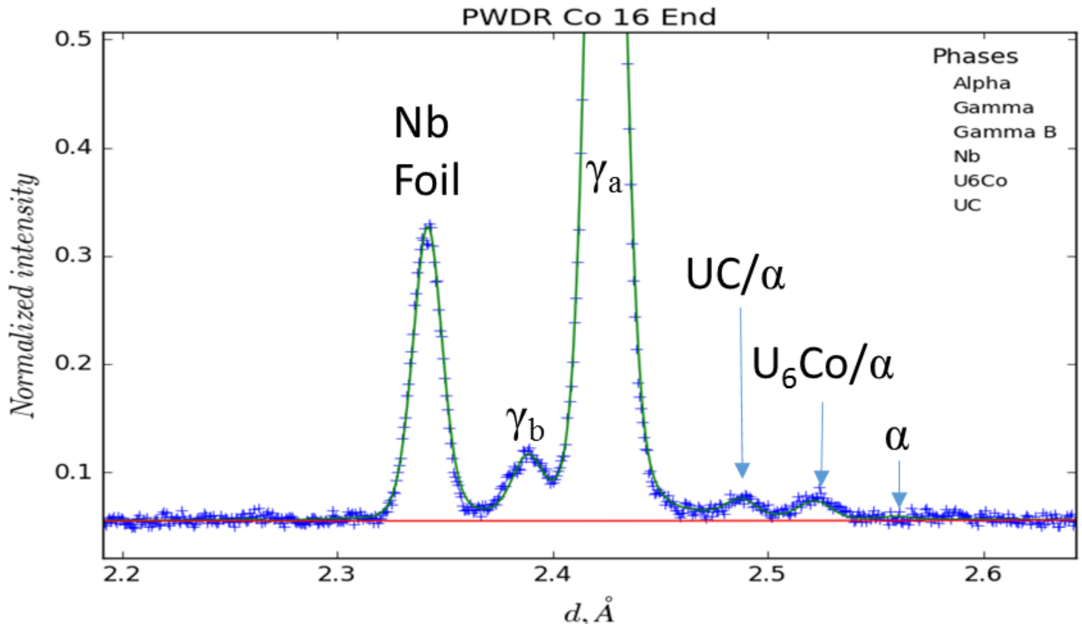

Figure 45. Diffraction pattern section for U-9.8Mo-0.2Co after aging

The phases which are common to all of the samples are the primary γ-U-Mo phase, γ_a, the carbide, UC, and the niobium foil. The small diffraction peak seen to the right of the primary γ-U-Mo peak was presumed to be uranium carbide, due to a number of matching peaks across the spectrum and since carbon is a common impurity in uranium which readily forms the carbide phase. The presence of uranium carbide was later confirmed using SEM and EDS [3]. In the samples containing chromium and nickel, pure molybdenum was found. Again, a number of peaks closely matched this phase, and it is logical that in a U-Mo alloy, some of the molybdenum may not have fully dissolved into the matrix. In the cobalt sample, an intermetallic U_6Co phase was found to match several peak locations. Most importantly, in the samples containing nickel and cobalt, phase decomposition has taken place, and α-U is visible. In addition to the α-phase, the peak corresponding to the Mo-rich metastable γ-phase, γ_b, is visible to the left of the main γ_a peak. The growth of this phase coincides with precipitation of the α-phase, which leaves molybdenum behind in the surrounding matrix. It is not as ordered as U_2Mo, but appears as a metastable phase, possibly with B2 ordering. The presence of all of these phases except for the molybdenum was later confirmed using SEM and EDS [3]. An explanation for why the molybdenum phase was not confirmed is that surface techniques were not capable of seeing it since it is inside the samples. This argument will be explained in depth later on. Visually, from the neutron diffraction patterns, it can be seen that U-10Mo and U-9.8Mo-0.2Cr samples did not undergo phase decomposition during the 20 hours at temperature, while the U-9.8Mo-0.2Ni and U-9.8Mo-0.2Co samples did. However, precipitation of the γ' (U_2Mo) phase which develops with slightly longer heating times, was not observed in the neutron diffraction patterns.

Since each of the samples was affected by carbon impurities which caused the formation of uranium carbide, it is important to understand how this phase could have affected the transformation kinetics of the uranium alloy. Carbon readily combines with uranium to form inclusions of UC in the uranium-molybdenum matrix, though this has little effect on the alloying behavior between uranium and molybdenum [41]. The preferential formation of the UC will pull uranium atoms from the U-Mo matrix, making the material slightly more Mo-rich than expected. From the phase diagram (Figure 46), carbon will not break from the bonds of the UC phase until the material is melted, so this phase is expected to remain through any of the heating steps performed following the initial melting and casting of the material.

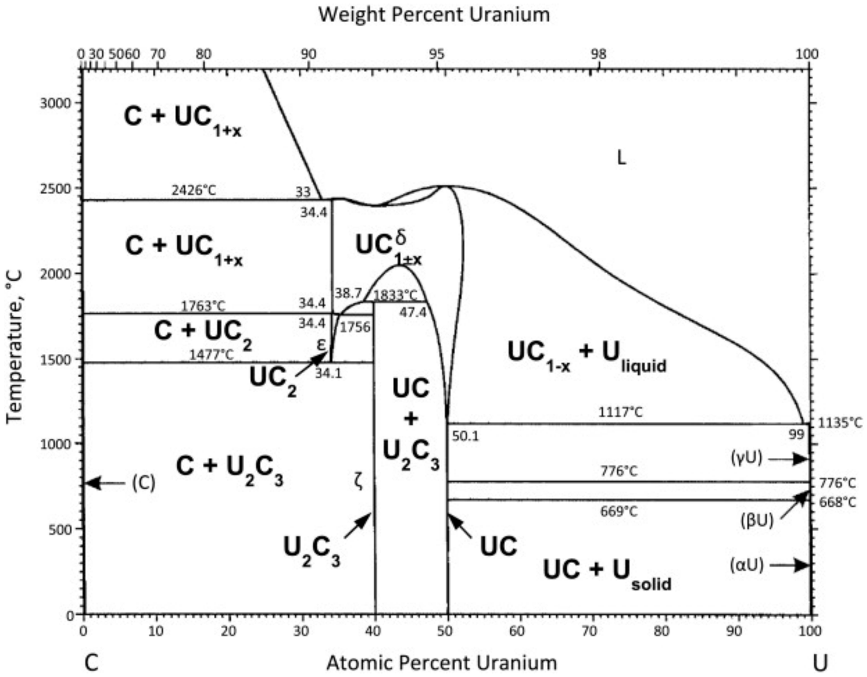

Figure 46. Phase diagram for uranium and carbon binary system [42]

The effect of carbon on the transformation kinetics of U-10Mo is not yet covered extensively in the literature. It has been postulated that uranium carbide precipitates could potentially serve as heterogeneous nucleation sites for phase decomposition [41], though there is little evidence for how this affects the rate of phase decomposition. The transformation to the equilibrium phases in U-Mo occurs by cellular transformation, which is aided by grain boundaries which act as high-diffusivity paths [3]. Since phase growth near the grain boundaries is highly preferred, it is predicted that the presence of carbide does not significantly affect the rate of phase decomposition.

3.4.2 Phase Content Determined by Rietveld Analysis

Rietveld analysis was performed using the Rietveld refinement software GSAS-II. To obtain an initial summary of the phase development during the SMARTS experiments, neutron diffraction data from the beginning and end of the isothermal holds was analyzed. The phase fractions determined from the analysis, reported in weight percent, are outlined in Table 7. Also shown is the estimated weight percent of impurity carbon that could have been in the material, under the assumption that all of the carbon formed UC.

Table 7. Weight percentages of phases at the beginning and end of the isothermal hold

Sample	γ_a	UC	γ_b	α	Mo	U_6Co	C (from UC)
U-Mo 500 C	99.1 → 99.1	0.9 → 0.9	-	-	-	-	0.043 → 0.043
U-Mo 490 C	99.0 → 99.0	1.0 → 1.0	-	-	-	-	0.048 → 0.048
Cr 500 C	96.4 → 96.3	1.1 → 1.0	-	-	2.5 → 2.6	-	0.053 → 0.048
Cr 490 C	96.9 → 97.6	1.1 → 0.6	-	-	2.0→ 1.8	-	0.053 → 0.029
Co 500 C	97.4 → 94.4	0.9 → 0.7	0 → 2.5	0 → 1.2	-	1.7 → 1.3	0.043 → 0.034
Ni 500 C	96.1 → 92.1	1.2 → 1.1	0 → 2.0	0 → 2.2	2.7 → 2.5	-	0.058 → 0.053

This data is consistent with the initial observations made by looking at the diffraction patterns. In the U-10Mo and U-9.8Mo-0.2Cr samples, the only phases present are the primary γ_a-phase and the UC, formed by carbon impurities. The weight percent of UC was found to lay between 0.5-1.9% with an average weight percent of 1.0% across the 12 samples. If it is assumed that all of the carbon in the sample is contained in uranium carbide, then the weight percent of carbon which is in the sample varies from 0.029 - 0.091 with an average weight percent of 0.048%. In these samples, the weight fractions of these phases stayed constant through the experiment (the Cr sample heated at 490 ºC shifted during the experiment, resulting in slightly different phase fractions). In the U-9.8Mo-0.2Co and U-9.8Mo-0.2Ni samples, phase decomposition is observed with the appearance of the α-U and Mo-rich γ_b phases by the end of the experiment. The U_6Co phase was present at the start of the isothermal hold, which means this phase must be stable at high and low temperatures. A Rietveld refinement was also performed on neutron diffraction data gathered *ex situ* on the samples which were not exposed to high temperature. This was done to check the phase content of the samples for comparison to the heated samples and also to be taken into consideration when planning future experiments. The results are reported in Table 8 in weight percent, where the sample number was only used to keep track of the samples.

Table 8. Weight percentages of unheated samples

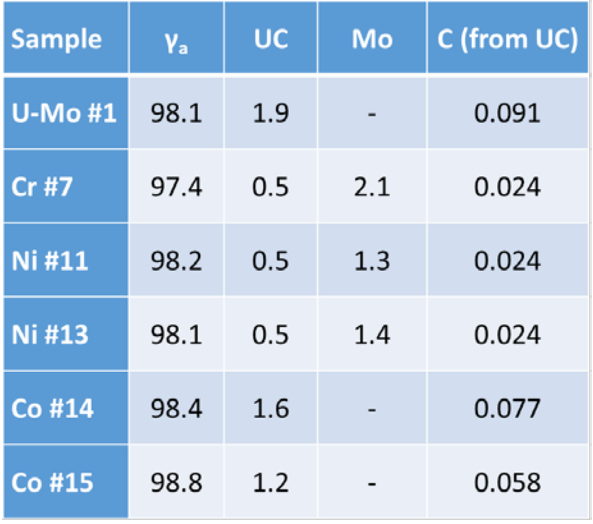

Sample	γ_a	UC	Mo	C (from UC)
U-Mo #1	98.1	1.9	-	0.091
Cr #7	97.4	0.5	2.1	0.024
Ni #11	98.2	0.5	1.3	0.024
Ni #13	98.1	0.5	1.4	0.024
Co #14	98.4	1.6	-	0.077
Co #15	98.8	1.2	-	0.058

These results are consistent with the *in situ* phase analysis results for the beginnings of the isothermal holds. UC is present in all samples in small amounts, and no secondary phases formed during cooling of the samples from the high-temperature homogenization. In addition, it is worth mentioning that all of the U-9.8Mo-0.2Cr and U-9.8Mo-0.2Ni samples contained pure molybdenum in the sample.

The phase content of all of the samples following the SMARTS experiments was also assessed using diffraction data gathered on HIPPO. For this analysis, the MAUD Rietveld refinement software was used for its built-in HIPPO analysis capability. The HIPPO analysis software is capable of efficiently performing Rietveld refinement while using the diffraction data gathered in the many data banks during a HIPPO experiment. The results are outlined in Table 9. Again, similar results are seen as far as the impurity content and the extent of decomposition that occurred in each of the samples. From the HIPPO results, the carbide content ranged from 1.6-2.5% (carbon content 0.077 -0.120%), resulting in an average carbide content of 2.0% (carbon content 0.096%).

Table 9. Weight percentages of all samples using HIPPO

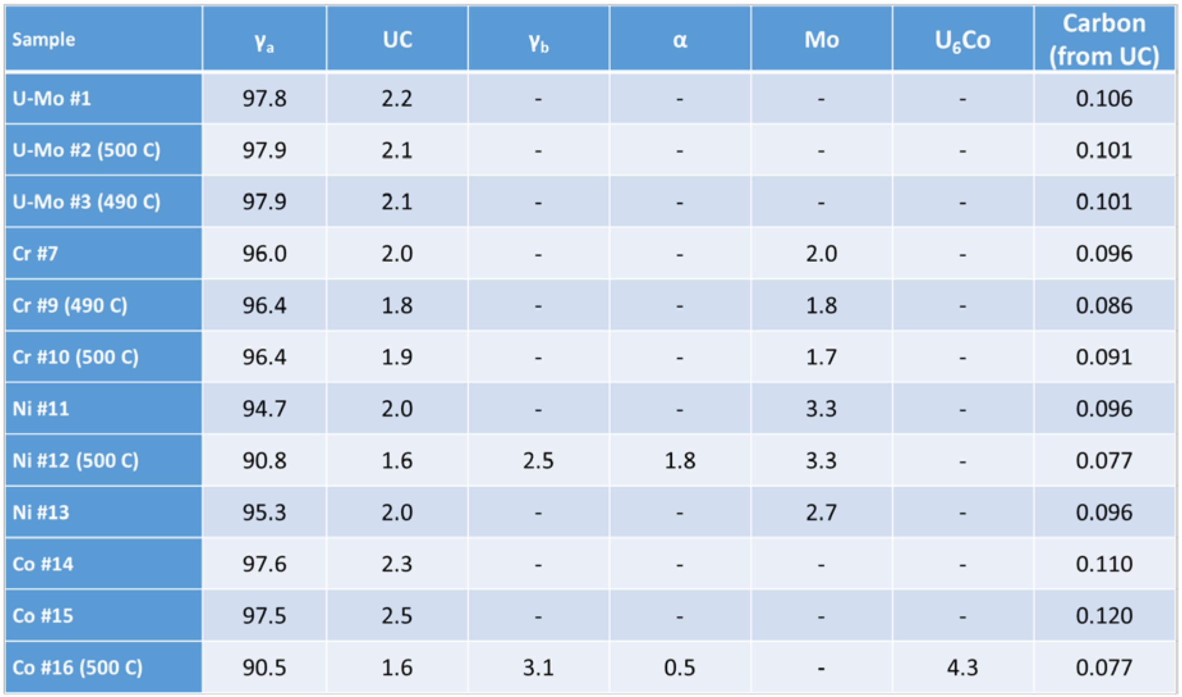

Sample	γ_a	UC	γ_b	α	Mo	U_6Co	Carbon (from UC)
U-Mo #1	97.8	2.2	-	-	-	-	0.106
U-Mo #2 (500 C)	97.9	2.1	-	-	-	-	0.101
U-Mo #3 (490 C)	97.9	2.1	-	-	-	-	0.101
Cr #7	96.0	2.0	-	-	2.0	-	0.096
Cr #9 (490 C)	96.4	1.8	-	-	1.8	-	0.086
Cr #10 (500 C)	96.4	1.9	-	-	1.7	-	0.091
Ni #11	94.7	2.0	-	-	3.3	-	0.096
Ni #12 (500 C)	90.8	1.6	2.5	1.8	3.3	-	0.077
Ni #13	95.3	2.0	-	-	2.7	-	0.096
Co #14	97.6	2.3	-	-	-	-	0.110
Co #15	97.5	2.5	-	-	-	-	0.120
Co #16 (500 C)	90.5	1.6	3.1	0.5	-	4.3	0.077

3.4.3 Phase Decomposition Kinetics in U-Mo-Ni and U-Mo-Co

The only samples which experienced phase evolution during the heating times were the Ni and Co samples. The evolution of the phase growth can be determined by using sequential Rietveld refinement in GSAS-II. In sequential Rietveld refinement, an initial analysis is performed on the first diffraction data set. The results from this refinement are then used as the initial values for the next refinement, and a refinement is done for a whole range of diffraction patterns. This is useful for an *in situ* experiment such as this, where weight fractions and lattice parameters of phases vary over the course of time and develop between diffraction patterns.

The evolution of the γ-U-Mo and α-U phases in the cobalt and nickel samples is shown in Figure 47 and Figure 48.

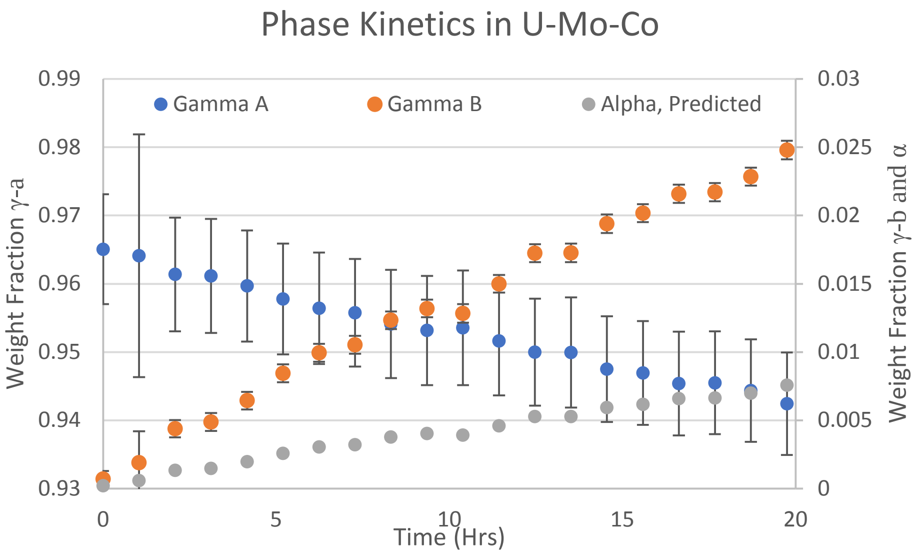

Figure 47. Phase evolution in U-Mo-Co

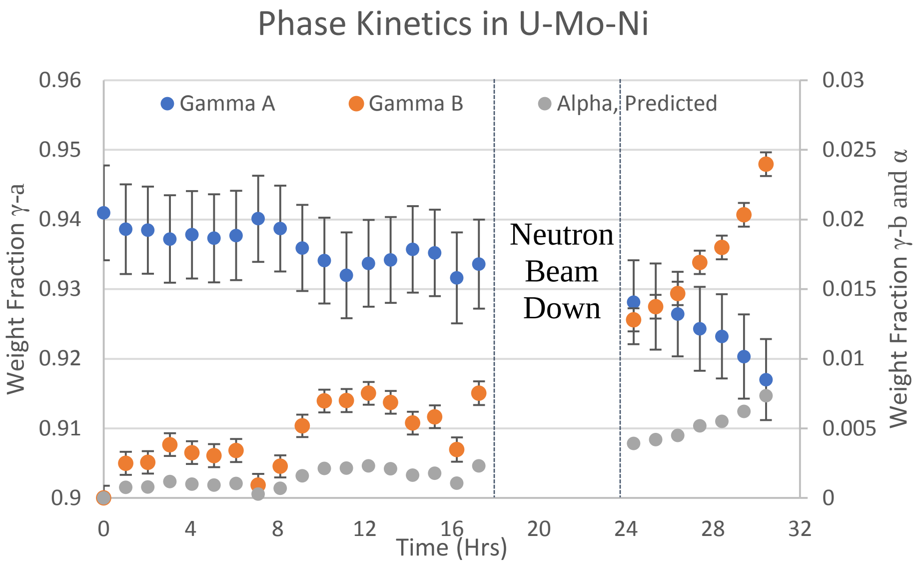

Figure 48. Phase evolution in U-Mo-Ni

The γ-U-Mo phase is shown to develop over the course of the experiment by transforming into two separate phases, γ_a and γ_b, with unique lattice parameters. The secondary phase, γ_b, is a metastable phase which forms along with the formation of α-U, and is molybdenum-rich. Since Rietveld refinement found that α-U was formed in very small weight fractions (< 1%), the kinetics of this phase transformation were difficult to capture using Rietveld refinement. It is therefore assumed that since γ_b and α-U are the only phases to form during this experiment, phase growth of α-U would occur in proportion to the development of γ_b. Thus the phase fractions of the α-U phase reported in the figures above are calculated from the metastable curve on the phase diagram (Figure 35) based on the amount of γ_b.

The phase growth in U-Mo-Co is shown to be linear over the course of the experiment. The phase growth in the U-Mo-Ni, however, begins to follow the expected shape of a JMAK curve, as seen by the increase in phase growth rate beginning around 24 hours. If the experiment were to continue longer, it is expected that the rate of phase growth would continue accelerating, level off, and then decelerate as the equilibrium amount of secondary phases is reached.

As phase decomposition occurs, the molybdenum concentration in the primary γ_a phase decreases, which in turn increases the lattice parameter. This change in lattice parameter can be plotted versus the weight fraction of the γ_a phase in the material. This relationship, seen in Figure 49, shows that as phase decomposition occurs, molybdenum-depletion of the γ-U-Mo phase corresponds directly to the amount of material transformed.

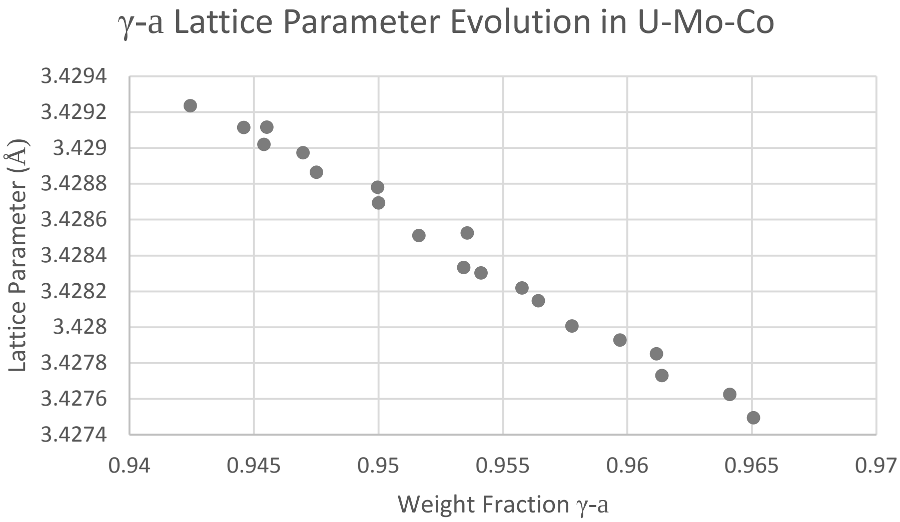

Figure 49. Evolution of γ-U-Mo lattice parameter during phase decomposition

3.4.4 Texture of Phases Measured with HIPPO

The texture of arc-cast samples is predicted to be relatively low, meaning that the material will have a mostly random grain distribution. The texture of each of the phases in the samples was analyzed using the E-WIMV feature in MAUD. E-WIMV is used to calculate the orientation distribution function (ODF) for each measured point to cover a pole figure. The ODF of each phase is refined during Rietveld refinement using the E-WIMV method. The textures of the γ-U-Mo phase for one sample which was only homogenized (unheated) and one sample which underwent an isothermal hold (heated), are shown in Figure 50. The carbide phase also displayed relatively low texture (Figure 51).

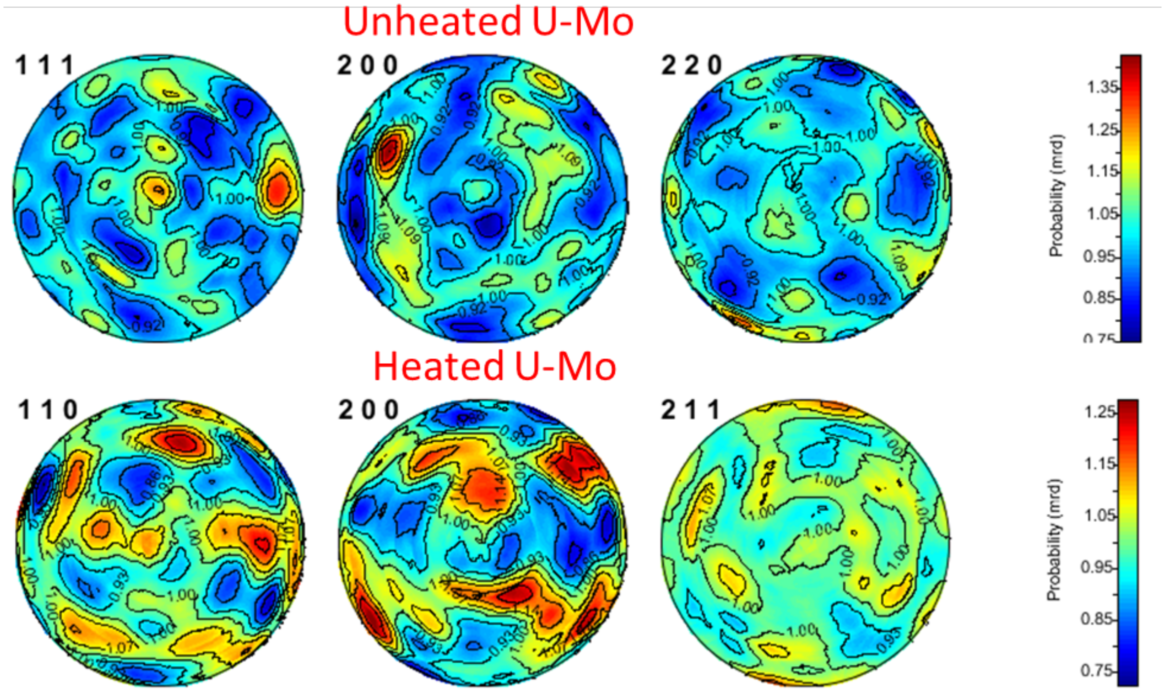

Figure 50. Texture of γ-U-Mo in two U-Mo samples

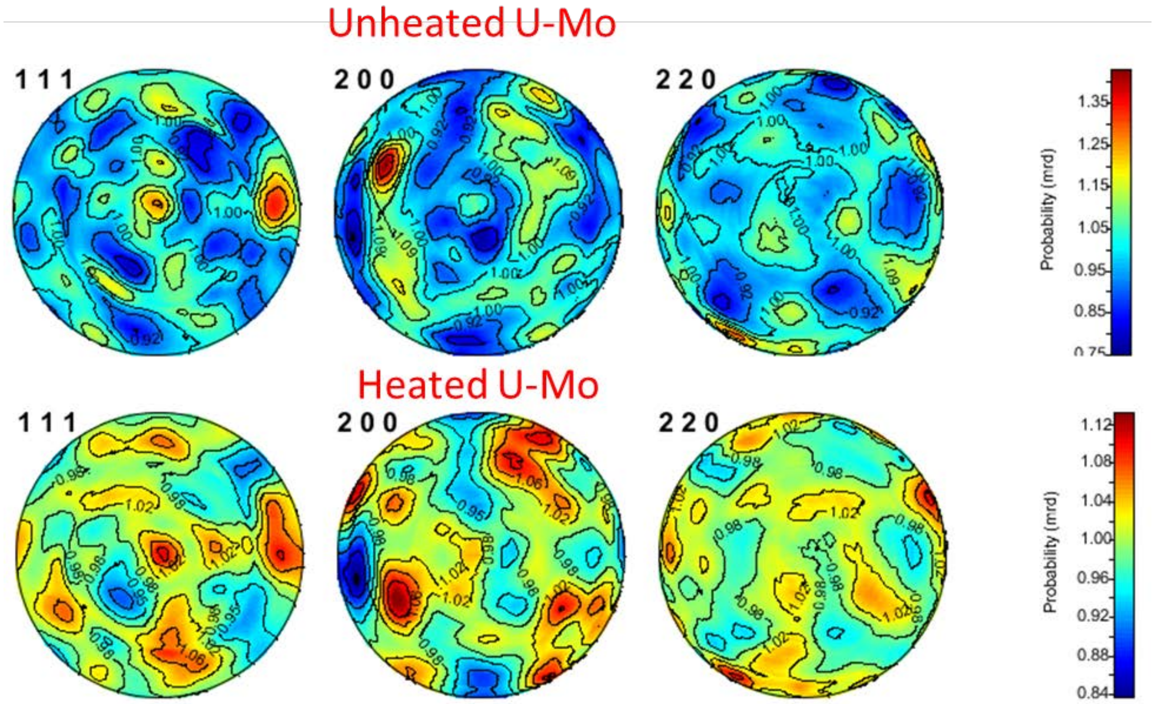

Figure 51. Texture of UC in two U-Mo samples

These pole figures confirm that the primary phases in the cast samples show a nearly random texture distribution, which is typical of cast samples. The molybdenum phase seen in the U-Mo-Cr and U-Mo-Ni samples, however, clearly displayed a <110> drawn fiber texture (Figure 52).

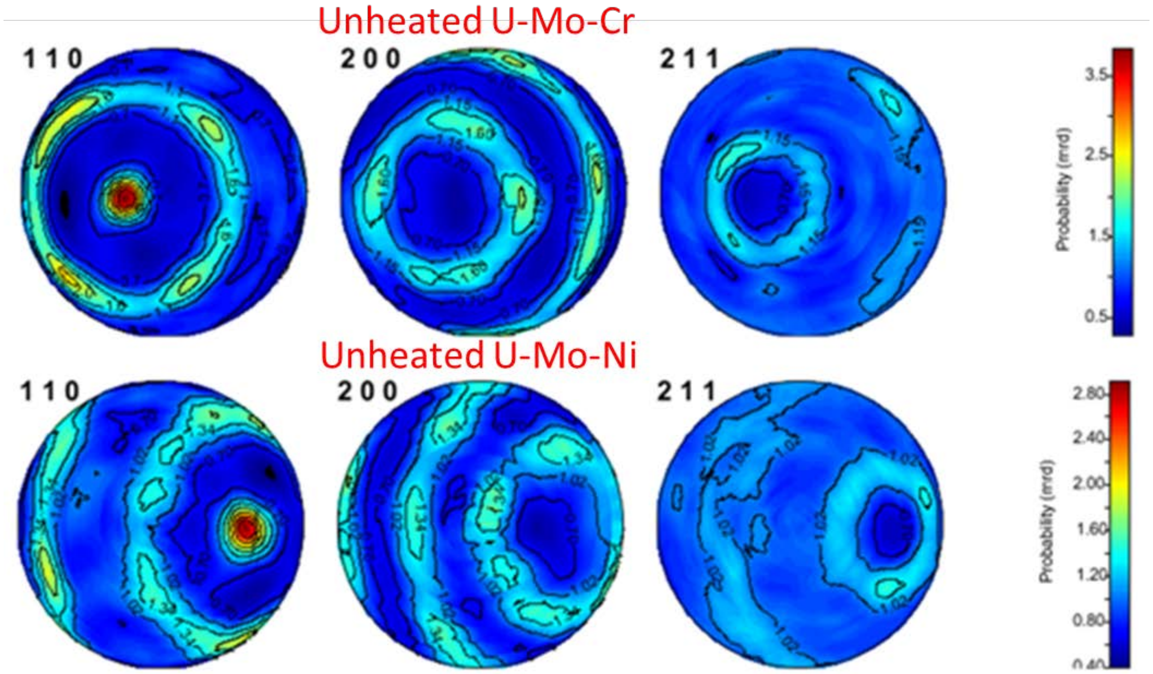

Figure 52. Texture of Mo in U-Mo-Cr and U-Mo-Ni samples

It was later confirmed in communication with PNNL that molybdenum was added to the samples by adding small wire pieces to the arc-melter. The presence of the molybdenum diffraction peaks and the clear texture discovered by E-WIMV suggest that the molybdenum fibers did not melt into the matrix.

3.4.5 Molybdenum in U-Mo-Cr and U-Mo-Ni

Molybdenum has a very high melting point, 2623 ºC, compared to the melting point of uranium which is 1132 ºC. The density of molybdenum is also low compared to uranium. Most likely, the molybdenum was not adequately melted in the material and rose to the top of the sample, forming a large cluster of unmelted molybdenum wires, which was picked up by both SMARTS and HIPPO. Rietveld analysis revealed that the weight percent of molybdenum in the Cr and Ni samples was in the approximate range of 2-3 wt%. This could be higher than in reality if the whole sample was not in the neutron beam, since the molybdenum cluster would account for a larger volume of the material.

If the molybdenum did not fully melt, the actual composition of the primary matrix in the Cr and Ni samples could very well be below 10 wt%. One indicator of how much molybdenum is in the material would be to check the lattice parameter of the primary γ-U-Mo phase, which will increase with lower molybdenum content and vice versa. If each sample is assumed to have 10 wt% molybdenum in total (from U-Mo and pure molybdenum), then the molybdenum content of the γ-U-Mo phase can be obtained by adding the molybdenum content of all of the other phases with weight fractions found by Rietveld analysis, and subtracting that weight fraction from 10%. This was plotted against the lattice parameter in Figure 53. The lattice parameters were found using Rietveld analysis.

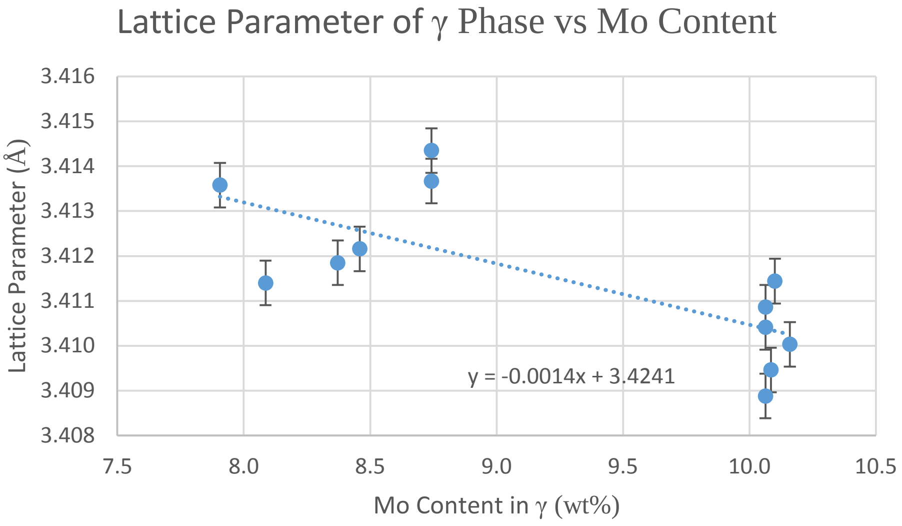

Figure 53. Lattice parameter vs matrix molybdenum content

The plot confirms that there is a relationship between the lattice parameter of the primary matrix phase and the predicted amount of molybdenum dissolved in the matrix using weight fractions gathered from Rietveld analysis. A lower molybdenum content in the primary phase can cause faster than expected phase decomposition in the material due to a lower alloying content in the matrix. Also, depending on how the molybdenum phase is dispersed, solid particles can serve as nucleation sites for phase decomposition. Another clues as to the nature of the molybdenum phase was discovered on SMARTS.

During the third experiment, the U-9.8Mo-0.2Cr sample shifted significantly due to the thermocouple pushing on the sample during movement of the sample stage. This shift occurred suddenly just before the 18 hour mark in the experiment. This shift is apparent in the neutron diffraction patterns because the Mo-peaks disappear from the diffraction pattern, meaning the molybdenum fell out of the beam path. These diffraction patterns (Figure 54, Figure 55) show that the peak seen at TOF ~29,000 completely disappears between the two frames.

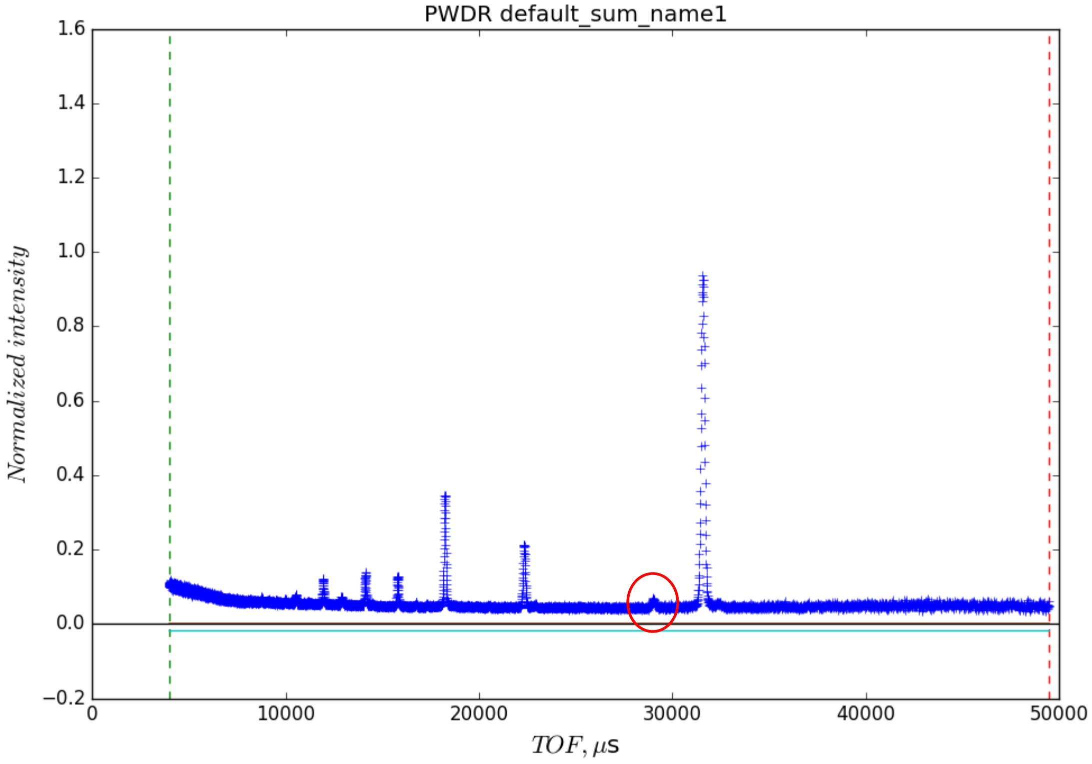

Figure 54. Molybdenum peak before sample shift

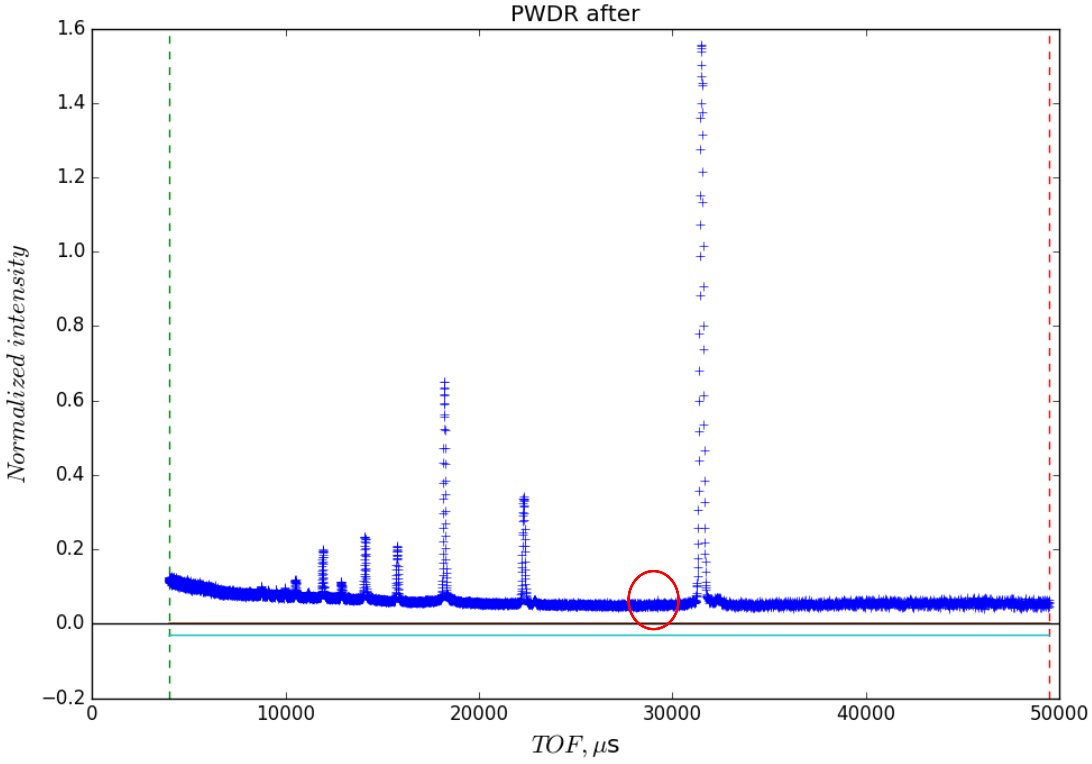

Figure 55. Molybdenum peak after sample shift

The intensity of this peak in comparison to the intensity of the largest γ_a peak was plotted over the approximate time range of the sample movement (Figure 56 and Figure 57) to observe the disappearance of this peak in proportion to how the overall intensity of the sample changed to determine if the disappearance of the phase was due to a sample shift or a reduction in incident intensity. During the time of the sample shift, the error associated with the peak intensity readings was 2-3% for the γ_a peak and just over 1% for the Mo peak.

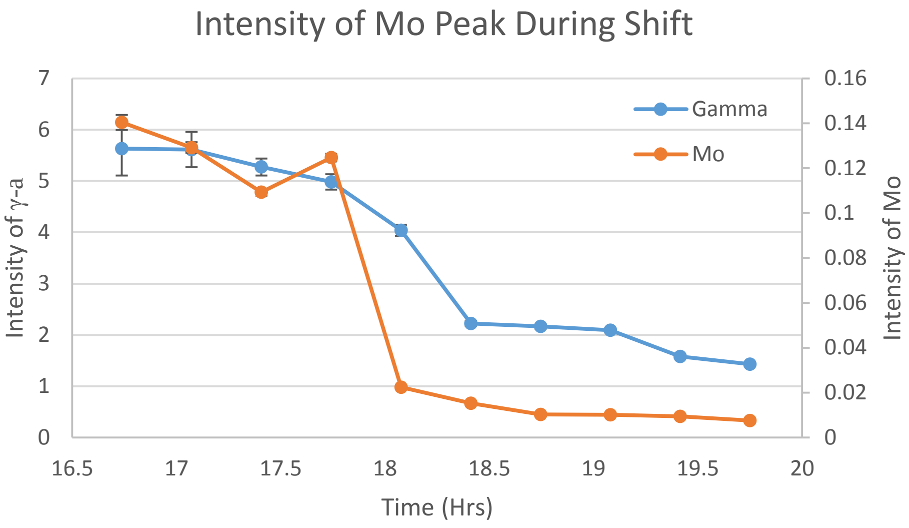

Figure 56. Intensity of γ-U-Mo peak and Mo peak during sample shift

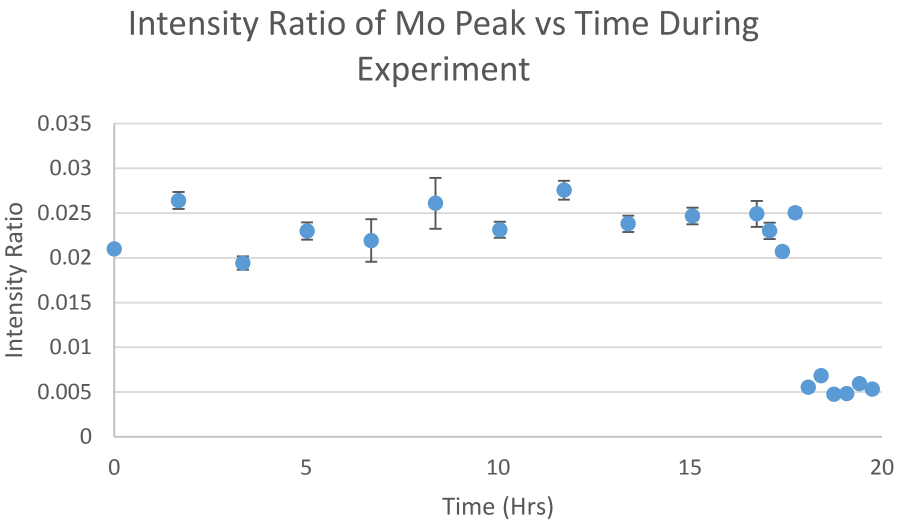

Figure 57. Intensity ratio of γ-U-Mo and Mo peak over the full experiment time

The intensity of the molybdenum peak falls within the noise of the background intensity, signifying that the phase was no longer observable by the beam. This likely means that this phase is a single, large chunk of material in a localized area of the sample.

3.5 Discussion

This neutron diffraction work was performed to complement work performed by Jana et al at Pacific Northwest National Laboratory [3]. The focus of that work was to study the microstructure of U-10Mo with 0.2 wt% additions of Cr, Ni, and Co using SEM, EDS, and x-ray diffraction in the as-cast condition, homogenized condition, and after 20 hours of aging at 500 ºC. Using these techniques allowed for a thorough analysis of the observable microstructure and phase content near the surface of the samples. Neutron diffraction, in particular used as an *in situ* technique, was useful for its ability to analyze phases seen through the bulk of the sample and track phase kinetics in real-time. In addition, it is a powerful tool for analyzing phase texture in the bulk of the material. The results of the neutron experiments will now be compared to the results from SEM to show how these techniques can be used to create a complete story of the phase information for a material system.

One of the major findings of the neutron diffraction study was that uranium carbide was present in small amounts in all of the samples. SEM and EDS work on the as-cast material confirmed this (Figure 58). Carbon impurities were determined to be present in the material at greater than 300 ppm [3]. Additionally, it was shown that the nickel and cobalt formed nickel- and cobalt-rich phases during this stage while the chromium dissolved into the matrix and did not form any observable phases.

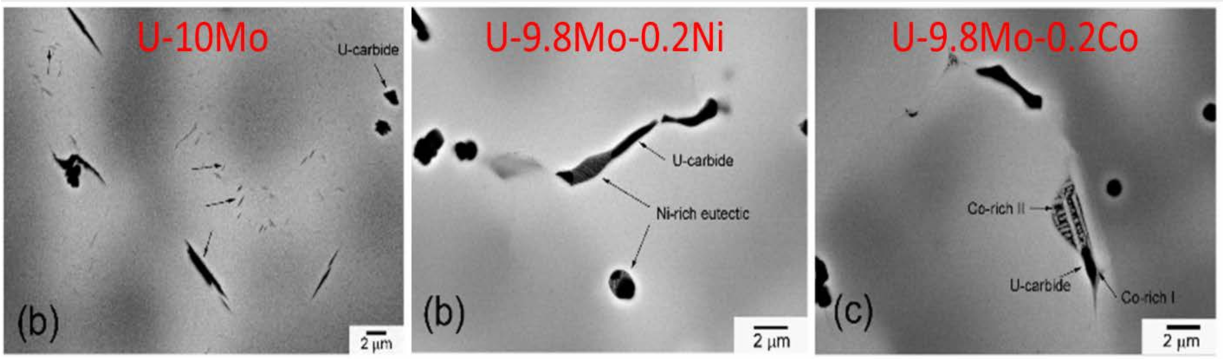

Figure 58. Comparison of as-cast microstructures of U-10Mo (left), U-9.8Mo-0.2Ni (center), and U-9.8Mo-0.2Co (right) [3]

Following homogenization, it was shown that the nickel-and cobalt-rich phases formed along the grain boundaries (Figure 59).The formation of these phases along the grain boundaries is expected to lower the energy for discontinuous precipitation to occur at these sites for phase decomposition of the U-10Mo. Additionally, it was discovered that in the case of U-9.8Mo-0.2Co, a fine lamellar structure was formed [3]. This lamellar structure consists of bright U_6Co lamella and a Mo-enriched inter-lamellar region. The molybdenum enrichment in the inter-lamellar region causes the area ahead of the lamellar structure to be low in molybdenum, which could possibly increase the rate of phase decomposition kinetics. A similar mechanism may be at play in the case of U-9.8Mo-0.2Ni, but this is still being confirmed.

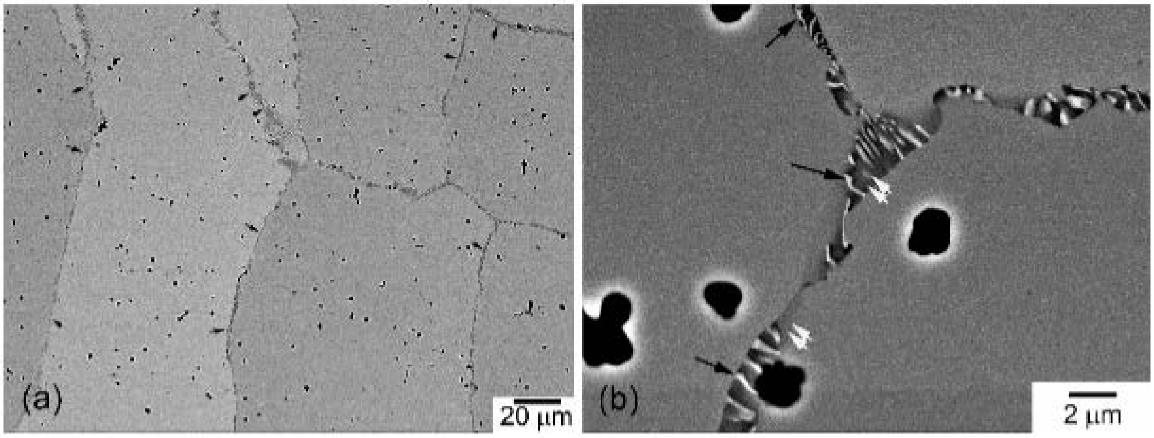

Figure 59. Homogenized microstructure of U-9.8Mo-0.2Co at two levels of magnification [3]

Ultimately, the neutron diffraction study clearly revealed that Ni and Co reduced the stability of the γ-phase in comparison to U-10Mo, while Cr did not have an observable effect on the stability. Indeed, these results were replicated at PNNL by aging one of each sample type at 500 ºC for 20 hours. In Figure 60, it can be seen that there is no major phase decomposition in the U-10Mo or U-9.8Mo-0.2Cr samples, while the U-9.8Mo-0.2Ni and U-9.8Mo-0.2Co samples did experience phase decomposition.

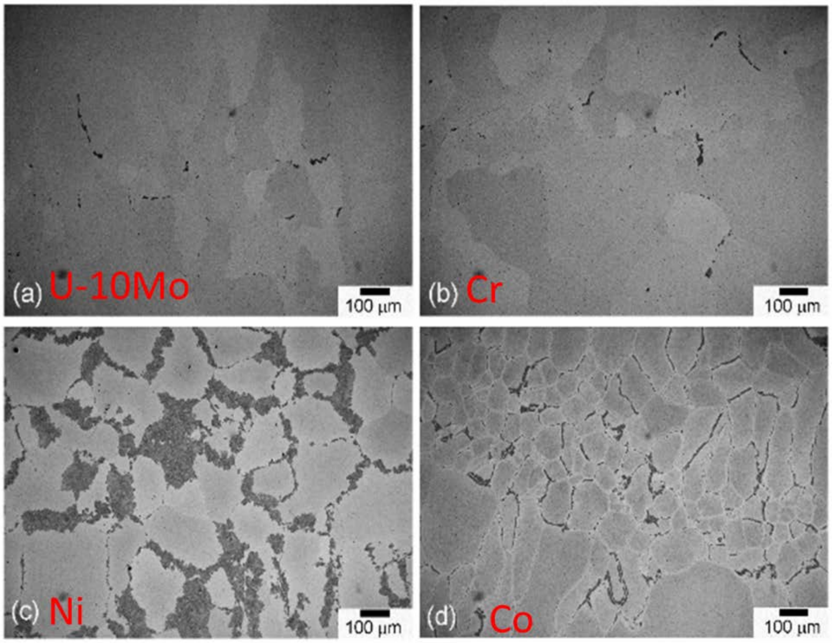

Figure 60. Microstructures of each sample type after 20 hours at 500 °C [3]

3.6 Conclusion

The neutron diffraction work on U-10Mo revealed that ternary additions of nickel and cobalt increased the rate of phase decomposition, while the addition of chromium did not significantly affect the rate of phase decomposition. The increased rate of phase decomposition is attributed to the development of nickel- and cobalt-rich phases which precipitated in the cast material and formed along the grain boundaries of the homogenized material. The discontinuous precipitation reaction then occurred at a faster rate in these materials, primarily along the grain boundaries of the former γ-U-Mo phase. In the nickel and cobalt samples, the formation of the α-U phase was accompanied by the formation of a Mo-rich γ-U-Mo phase, γ_b. The onset of the formation of γ’ (U_2Mo), was not witnessed during these experiments. Chromium dissolved into the matrix and did not form any phases which progressed the rate of the phase kinetics within the detection limits of the methods employed.

4. Overall Thesis Conclusions and Future Work

Each of the initial research goals was met by the execution of this work. The anisotropic yield strength behavior of rolled LEU foils was captured using the CPB06 model for plastic anisotropy and asymmetry. The parameters of this model were successfully fit using a MATLAB script with an optimization algorithm, and then implemented in a user subroutine for ABAQUS/Explicit. The user subroutine with the implemented anisotropy model allowed for a FEA study of internally-pressurized thick-walled tubes, to understand how plastic anisotropy affects internally pressurized materials with various anisotropy conditions. The user subroutine was then applied to FEA simulations of LEU foils as components of an irradiation target undergoing hydroforming and irradiation, to determine whether anisotropy of the LEU is a major factor in the manufacturing and use of these irradiation targets.

The results ultimately showed that for the current configuration, the anisotropy of the LEU foil is not a major factor in the resulting stress-state of the irradiation target. Due to the orientation of the foil with the annular target, the effects of anisotropy, which include higher compressive strength along the ND and lower tensile strength along the TD, essentially cancelled out. However, it is predicted that if the foil orientation were changed such that the RD wrapped around the θ-direction of the tube and the TD was aligned with the tube axis, the increase in compressive strength along the ND and increase in tensile strength along the RD would cause the foil to resist yielding under internal pressure to a greater degree.

For the hydroforming simulations, it was determined that a pressure of 41 MPa during hydroforming is required to maintain contact between each of the target components, which lasts through the irradiation step. Upon removal of this pressure, small tensile hoop stresses will remain in the outer tube, which are expected to aid in the retrieval of the irradiated foil. However, it is likely that the temperatures seen during irradiation will relax these residual stresses to a more neutral state.

The results here have serious implications. For example, the pressure required to hydroform the irradiation target may need to be increased to ensure full contact between the foil and tubes. Given that previous experiments on hydroforming of this type of structure revealed that only a maximum internal pressure of 36.4 MPa could be reached before failure of the assembly by rupture of the tubes along the foil relief section [13], the strength of the aluminum tubes would need to be decreased, allowing sufficient plastic strain at lower pressures to ensure intimate contact between the foil and surrounding Al tubes. One possibility is employing Al alloy 6061 in the softer and more ductile T4 (solution heat treated and quenched) temper, rather than the higher strength T6 (artificially aged to peak hardness) temper employed in this and prior studies.

Based on the advances made in this research, future work could be done in two areas. The first area of future work would be further research in the area of hydroforming and target assembly, considering the challenge identified above. During conversion from use of HEU to LEU, it is desirable to use similar target geometry as much as possible to simplify the process of conversion [43]. This limits the level to which the geometry of the target components can be altered. However, modeling could be employed to determine whether a softer tube material would permit use of lower pressures during assembly. Additionally, it is known that aluminum tubes can have considerable levels of plastic anisotropy, which much like the anisotropy in uranium foils, is due to the manufacturing processes which cause a large reduction in thickness of the material [44]. When the anisotropy is considered in FEA simulations of hydroforming of thin-walled tubes, this can change the results noticeably [45]. Though the focus of research for HEU to LEU conversion is understandably on the LEU material itself, since the aluminum tubes are such a large component of the irradiation target system, plastic anisotropy in the aluminum tubes ought to be accounted for as well, if the true stress-state of the system is to be successfully modeled. Additionally, research on how the orientation of the foil can affect the strength of the foil under internal pressure will be pursued. If the foil is rotated so that the TD is aligned with the tube axis, the anisotropy is predicted to make the foil stronger than the isotropic case, but whether this will affect the simulation results significantly is currently unknown.

The second area would be FEA-based research of other material systems with plastically anisotropic components, since a method for easily modeling the plastic anisotropy and employing this in finite element simulations was demonstrated and shown to be effective here. Many engineering problems assume that the material being used is isotropic, but this is often not the case with materials that undergo forming process, due to texture development. A simple method for incorporating plastic anisotropy in FEA would help modelers which are evaluating or designing parts made of anisotropic materials.

Neutron diffraction was used to study the phase transformation kinetics in U-10Mo and the effectiveness of three alloying elements as γ-U-Mo stabilizers. It was found the compared to U-10Mo and U-9.8Mo-0.2Cr did not undergo noticeable phase decomposition during the time-frame of the experiments, while U-9.8Mo-0.2Ni and U-9.8Mo-0.2Co did undergo discontinuous precipitation of the equilibrium phase, α-U, and a corresponding metastable Mo-rich γ-U-Mo phase.

There is still much more work that can be done in this area of research. First, these ternary U-Mo-X systems can be studied more extensively using the analysis techniques discussed in this thesis. One limiting factor to studying the phase kinetics of these materials was the limited time on the neutron beam. In order to do an *in situ* diffraction study, only about the first 20 hours of the phase transformation could be observed. This problem could be avoided by preparing more samples, aging them at the same temperature for a variety of different times, and then performing *ex situ* neutron diffraction on these aged samples, which would have a similar result as doing an *in situ* analysis, but enabling for much longer gaining times to be reached. The disadvantage to this is that the time between data points would increase, reducing the precision of phase growth curves. Additionally, different temperatures could be explored. In these experiments, 500 ºC was used since it is the temperature at which the fastest phase decomposition is expected to occur, but the reaction kinetics at surrounding temperatures need to be studied in order to help develop the TTT diagram for this class of material.

Another area of research which would be beneficial for the LEU fuel research community would be to research how carbon impurities affect the phase reaction kinetics. Carbon is a common impurity in U-Mo, but is generally present in low enough levels that the performance of the material is not seriously affected. However, it would be beneficial to know how these impurities affect the performance of the material with higher confidence than is currently available in literature. The 12 samples used for this thesis work will be rehomogenized and used for future experiments at different temperatures and times than used in these experiments.

Appendix: Finite Element Material Properties

Isotropic Uranium

Elastic and Thermal		
Property	Value	Units
Conductivity	27.5	$\frac{mW}{mm\cdot K}$
Mass Density	1.89E-08	$\frac{tonne}{mm^3}$
Young's Modulus	208,000	MPa
Poisson's Ratio	0.23	
Expansion Coefficient	1.39E-05	
Specific Heat	1.16E+08	$\frac{mJ}{tonne\cdot K}$
Plastic		
Plastic Strain	Yield Stress (MPa)	
0	110	
0.0001	132.2491	
0.00012	137.9127	
0.000144	143.8189	
0.000173	149.9781	
0.000207	156.401	
0.000249	163.0989	
0.000299	170.0837	
0.000358	177.3677	
0.00043	184.9636	
0.000516	192.8847	
0.000619	201.1451	
0.000743	209.7593	
0.000892	218.7424	
0.00107	228.1102	
0.001284	237.8791	
0.001541	248.0664	
0.001849	258.69	
0.002219	269.7686	
0.002662	281.3216	
0.003195	293.3693	
0.003834	305.9331	
0.004601	319.0348	
0.005521	332.6977	
0.006625	346.9457	
0.00795	361.8038	

0.00954	377.2983
0.011448	393.4563
0.013737	410.3063
0.016484	427.878
0.019781	446.2021
0.023738	465.311
0.028485	485.2382
0.034182	506.0188
0.041019	527.6894
0.049222	550.288
0.059067	573.8544
0.07088	598.4301
0.085056	624.0582
0.102067	650.7839
0.122481	678.6541
0.146977	707.7178
0.176373	738.0263
0.211647	769.6327
0.253977	802.5927
0.304772	836.9642
0.365726	872.8077
0.438871	910.1862
0.526646	949.1655
0.631975	989.8141
0.75837	1032.204
0.910044	1076.408
1.092053	1122.506

Anisotropic Uranium

Elastic and Thermal		
Property	**Value**	**Units**
Conductivity	27.5	$\frac{mW}{mm\cdot K}$
Mass Density	1.89E-08	$\frac{tonne}{mm^3}$
Expansion Coefficient	1.39E-05	
Specific Heat	1.16E+08	$\frac{mJ}{tonne\cdot K}$
CPB06		
Property	**Value**	**Units**
Young's Modulus	208,000	MPa
Poisson's Ratio	0.23	

Yield Strength (Along RD)	403	MPa
Strength Coefficient	155	MPa
Strain-Hardening Exponent	0.14	
Tolerance	0.001	
Iterations	50	
C11	1	
C12	2.6461	
C13	2.8173	
C22	2.8563	
C23	3.9708	
C33	2.6907	
C44	1	
C55	1	
C66	1	
Strength Differential	-0.22212	
Yield Function Exponent	2	

Aluminum 6061-T6

Elastic and Thermal		
Property	Value	Units
Conductivity	167	$\frac{mW}{mm \cdot K}$
Mass Density	2.70E-09	$\frac{tonne}{mm^3}$
Young's Modulus	68,900	Mpa
Poisson's Ratio	0.33	
Expansion Coefficient	2.34E-05	
Specific Heat	9.04E+08	$\frac{mJ}{tonne \cdot K}$

Plastic	
Yield Stress (Mpa)	Plastic Strain
297.853632	0
303.8175994	0.000103788
312.6359974	0.000203785
314.8285311	0.000303384
318.8274919	0.000466394
320.234023	0.000552785
321.7991335	0.000608999
322.5920309	0.000731266
323.1780855	0.000858794

323.6676134	0.000971875
324.081299	0.001085319
328.852473	0.002007559
329.7625813	0.003042606
330.5830577	0.004011623
331.5138503	0.005116114
332.2791687	0.006029545
333.0927504	0.007016436
333.9683849	0.008079003
334.8026508	0.009092942
335.6369168	0.010120768
336.4573932	0.011144042
337.1675535	0.01201472
338.0293985	0.013096637
338.8085064	0.014084403
339.5807195	0.015089081
340.3460379	0.016067536
341.1527248	0.017112634
341.8697798	0.018050733
342.641993	0.019095253
343.4211008	0.020124437
347.0615341	0.025094361
350.5295984	0.030056984
353.8528727	0.035046752
357.0658309	0.040131487
359.9961039	0.045028114
362.7815869	0.05001076
365.4153852	0.055052257
367.807867	0.060035567
370.048664	0.065101616
372.0343548	0.070091989
373.7994134	0.07504856
375.4058925	0.080053495
377.0330558	0.08533269
378.4257974	0.090070093
379.8047494	0.095017098
381.1423328	0.100062445
392.3670021	0.1570037
402.4264569	0.223143551
411.1069598	0.300104592
420.1115163	0.405465108

426.5443274	0.500775288
431.4947651	0.587786665
432.9081909	0.615185639
436.6451508	0.693147181
437.7483124	0.717839793
440.7130592	0.78845736
441.609378	0.810930216
444.7947571	0.896088025
445.5118122	0.916290732
448.6971913	1.011600912

Plastic behavior of isotropic uranium and aluminum gathered from Shrisharan et al. [13]

References

[1] M. A. Steiner, R. W. Klein, C. A. Calhoun, M. Knezevic, E. Garlea, S. R. Agnew, "Efficient rolling texture predictions and texture-sensitive thermomechanical properties of alpha-uranium foils," *Journal of Nuclear Materials,* vol. 495, pp. 234-243, November 2017.

[2] O. Cazacu, B. Plunkett, F. Barlat, "Orthotropic yield criterion for hexagonal closed packed metals," *International Journal of Plasticity,* vol. 22, pp. 1171-1194, 2006.

[3] S. Jana, L. Sweet, D. Neal, A. Schemer-Kohrn, S. R. Agnew, V. Joshi, C. Lavender, "The role of ternary alloying elements in eutectoid transformation of U10Mo alloy," 2018.

[4] D. E. Burkes, R. Prabhakarn, T. Hartmann, J. -F. Jue, F. J. Rice, "Properties of DU-10 wt% Mo alloys subjected to various post-rolling heat treatments," *Nuclear Engineering and Design*, vol. 240, pp. 1332-1339, 2010.

[5] "Civilian HEU Reduction and Elimination Resource Collection," Nuclear Threat Initiative. 2017.

[6] "U.S. Agencies Have Limited Ability to Account for, Monitor, and Evaluate the Security of U.S. Nuclear Material Overseas," September 2011.

[7] A. J. Kuperman, "Global HEU Phase-Out: Prospects and Challenges," in *Nuclear Terrorism and Global Security: The Challenge of Phasing Out Highly Enriched Uranium*, ed: Routledge, 2013, pp. 16-22.

[8] E. Bradley, "Non-HEU Production Technologies for Molybdenum-99 and Technetium-99m," 2013.

[9] National Research Council, *Medical Isotope Production without Highly Enriched Uranium*: The National Academies Press, 2009.

[10] P. Gould, "Medical isotope supplies dwindle," in *Nature International Weekly Journal of Science*, ed.

[11] J. Creasy, "Update on the Development and Manufacture of High Density LEU-Foil Targets for the Production of Mo-99," Y-12 National Secuirty Complex. June 2014.

[12] J. R. Lisboa, J. Marin, M. E. Barrera, G. Cifuentes, "Manufacturing of Annular Targets Made of LEU Foil Coated with Electrodeposited Nickel," *Procedia Materials Science,* vol. 8, pp. 343-441, 2015.

[13] S. G. Govindarajan, B. S. Graybill, P. F. Makarewicz, Z. Xie, G. L. Solbrekken, "Assembly and Irradiation Modeling of Residual Stresses in Low-Enriched Uranium Foil-Based Annular Targets for Molybdenum-99 Production," *Science and Technology of Nuclear Installations*, vol. 2013, 2013.

[14] Boybul, B. Briyatmoko, Sriyono, A. H. Gunawan, H. Lubis, A. Mutalib, Abidin, Hambali, "Experiences of HEU to LEU Mo-99 Production Conversion," Center for Nuclear Fuel Technology, Center for Radioisotope and Radiopharmaceutical. 2009.

[15] R. W. Cahn, P. Haasen, E. J. Kramer, "Nuclear Materials," in *Materials Science and Technology: A Comprehensive Treatment*. vol. 10A, ed, 1994.

[16] M. K. Meyer, J. Gan, J. F. Jue, D. D. Keiser, E. Perez, A. Robinson, D. M. Wachs, N. Woolstenhulme, G. L. Hofman, Y. S. Kim, "Irradiation Performance of U-Mo Monolithic Fuel," *Nuclear Engineering and Technology,* vol. 46, pp. 169-182, April 2014.

[17] M. K. Meyer, G. L. Hofman, S. L. Hayes, C. R. Clark, T. C. Wiencek, J. L. Snelgrove, R. V. Strain, K. -H Kim, "Low-temperature irradiation behavior of uranium-molybdenum alloy dispersion fuel," *Journal of Nuclear Materials,* vol. 304, pp. 221-236, August 2002.

[18] P.E. Repas, R. H. Goodenow, R. F. Hehemann, "An Investigation of Transformation Characteristics of Three Uranium Base Alloys," U.S. Army Materials Research Agency. 1963.

[19] V. W. Storhok, A. A. Bauer, R. F. Dickerson, "Survey of Ternary and Quarternary Metastable Gamma-Phase Uranium Alloys," Battelle Memorial Institue. 1958.

[20] G. L. Hofman, M. K. Meyer, A. E. Ray, "Design of High Density Gamma-Phase Uranium Alloys for LEU Dispersion Fuel Applications," presented at the The 1998 International Reduced Enrichment for Test Reactor Conference, Sao Paulo, Brazil, 1998.

[21] J. R. Einhorn, M. A. Steiner, S. C. Vogel, E. Garlea, S. R. Agnew, "Crystallographic texture of straight-rolled alpha-uranium foils via neutron and x-ray diffraction," *Journal of Applied Crystallography,* vol. 50, pp. 859-865.

[22] C. A. Calhoun, E. Garlea, R. P. Mulay, T. A. Sisneros, S. R. Agnew, "Investigation of the effect of thermal residual stresses on deformation of alpha-uranium through heutron diffraction measurements and crystal plasticity modeling," *Acta Materialia,* vol. 85, pp. 168-179, February 2015.

[23] C. A. Calhoun, J. A. Wollmershauser, D. W. Brown, R. P. Mulay, E. Garlea, S. R. Agnew, "Thermal residual strains in depleted alpha-U," *Scripta Materialia,* vol. 69, pp. 566-569, October, 2013.

[24] B. McGinty, "Von Mises Stress," Yield_Surfaces, Ed., ed. www.continummmechanics.org, 2012.

[25] D. G. Tari, M. J. Worswick, U. Ali, M. A. Gharghouri, "Mechanical response of AZ31B magnesium alloy: experimental characterization and material modeling considering proportional loading at room temperature," *International Journal of Plasticity,* vol. 55, pp. 247-267, 2014.

[26] B. Williams, H. Sinha, "Cazacu-Plunkett-Barlat 06 VUMAT for Abaqus Explicit," ed, 2016.

[27] R. W. Klein, "Measurement and Prediciton of Texture Evolution During Processing: Application to Rolled alpha-Uranium and Extruded Magnesium Alloys," Master of Science, Materials Science and Engineering, University of Virginia, 2016.

[28] J. Chakrabarty, *Theory of Plasticity,* 3 ed.: Elsevier Science & Technology, 2012.

[29] M. Kumamoto, "Thick Walled Tube," ed, 2017.

[30] J. E. Antill, K. A. Peakall, "Oxidation of uranium alloys in carbon dioxide and air," *Journal of the Less COmmon Metals,* vol. 3, pp. 239-246, June 1961.

[31] M. A. Steiner, C. A. Calhoun, R. W. Klein, K. An, E. Garlea, S. R. Agnew, "Alpha-Phase transformation kinetics of U-8 wt% Mo established by in situ neutron diffraction," *Journal of Nuclear Materials,* vol. 477, pp. 149-156, August 2016.

[32] S. Jana, A. Devaraj, L. Kovarik, B. Arey, L. Sweet, T. Varga, C. Lavender, V. Joshi, "Kinetics of cellular transformation and competing precipitation mechanisms during sub-eutectoid annealing of U10Mo alloys," *Journal of Alloys and Compounds,* vol. 723, pp. 757-771, June 2017.

[33] S. Vogel, M. Reiche, D. Brown, M. Okuniewski, "Characterization of nuclear fuels on HIPPO," Los Alamos National Laboratory.

[34] 2012. *Method to investigate structure: Diffraction.*

[35] J. K. Cockcroft. (2006). *Time-of-Flight Concepts*.

[36] (2017). *Spectrometer for Materials Research at Temperature and Stress, SMARTS*.

[37] (2017). *High-Pressure-Preferred Orientation*.

[38] A. Garg, "A Brief Introduction to Rietveld Analysis of XRD Patterns," ed: Materials Science & Engineering, IIT Kanpur.

[39] S. Jana, "UMo Furnace Cooling Profile," D. Malta, Ed., ed.

[40] H. R. Wenk, L. Lutterotti, S. C. Vogel, "Rietveld texture analysis from TOF neutron diffraction data," *Powder Diffraction,* vol. 25, pp. 283-296, September 2010.

[41] R. L. Craik, D. Birch, C. Fizzotti, F. Saraceno, "Phase equilibria in uranium-rich binary alloys containing molybdenum and zirconium and the effect of ternary additions of carbon," *Journal of Nuclear Materials,* vol. 6, pp. 13-25, June 1962.

[42] H. Okamoto, "C-U (carbon-uranium)," *Journal of Phase Equilibria and Diffusion,* vol. 26, pp. 642-642, Decemeber 2005.

[43] G. F. Vandegrift, C. Conner, G. L. Hofman, R. A. Leonard, A. Mutalib, J. Sedlet, D. E. Walker, T. C. Wieneck, J. L. Snelgrove, "Modification of Targets and Processes for Conversion of 99Mo Production from high- to Low-Enriched Uranium," Argonne National Laboratory.

[44] N. Tardiff, S. Kyriakides, "Determination of anisotropy and material hardening for aluminum sheet metal," *International Journal of Solids and Structures,* vol. 49, pp. 3496-3506, December 2012.

[45] Y.P. Korkolis, S. Kyriakides, "3-D and Anisotropic Effects on the Prediction of Burst in Aluminum Tube Hydroforming," in *10th International Conference on Numerical Methods in Industrial Forming Processes,* Pohang, South Korea, 2010, pp. 141-148.